Exploring solid supported membrane based electrophysiology as an alternative platform to probe activity of membrane transport proteins

Matthias Gantner

Submitted in accordance with the requirements for the degree of

Doctor of Philosophy

The University of Leeds

School of Biomedical Sciences

December 2017

The candidate confirms that the work submitted is his own and that appropriate credit has been given where reference has been made to the work of others.

Acknowledgements

I would like to thank my supervisors, Prof. Lars Jeuken and Prof. Asipu Sivaprasadarao for their advise and support during my PhD project. I would like thank soon-to-be Dr Theo Laftsoglou, Dr David Sharples, Honglin Rong and Kristofer Jones for helping me with protein expression and purification.

My special thanks goes to the many people from different research groups that gave me help and advise, including Dr Chi Trinh, Dr Vincent Postis, Dr Maren Thomsen, Dr Steven Harbourne, Dr Irshad Ahmad and Dr Vlad Vasilca. For their help with cell culture I would like to thank Riitta Partanen and Dr Nada Abuarab.

For their moral support I want to thank all the current members of the Jeuken research group, including Anna Stikane, Dr Hope Adamson, Joe Oram and Dr Ievgen Mazurenko, but also our new neighbours from the bioincubator.

Finally, I would like to thank my friends and family for their unconditional support.

Abstract

Membrane transport proteins take a pivotal role in all forms of life as they are responsible for organising traffic of ions and small molecules across the hydrophobic barrier of biological membranes. Mutations in membrane transporters can often lead to severe diseases and they often consitute drug targets. Hence, assaying function of membrane transporters is of great importance.

In this project the method used for this task was mainly a relatively uncommon technique called solid-supported membrane based electrophysiology. The goal was to test this technique on targets that are challenging to investigate by more conventional methods. A first target was the TRPM2 ion channel. TRP channels are difficult to investigate because they often show a very complex activation pattern. A second target was the bacterial transition metal transporter MntH2 from *Enterococcus faecalis*, belonging to the SLC11 family. Transition metal transporters are generally difficult to investigate, because of the nature of their substrates. Some transition metals are redox-active and in solution they act as complexing agents.

Application of solid supported membrane based electrophysiology was not successful for TRPM2, but the method was used to perform basic biophysi-

cal characterisation of MntH2. It was found that MntH2 transports a range of substrates including Mn^{2+}, Cd^{2+},Co^{2+} and Zn^{2+}. Ni^{2+} and Cu^{2+} were not transported and in fact inhibited manganese uptake. Interestingly, in the presence of the protonophore carbonyl cyanide m-chlorophenyl hydrazone (CCCP) electrophysiological currents were not affected. This, together with the observation from a complementary assay, that reconstituted MntH2 did not acidify the interior of vesicles loaded with pH-sensitive fluorescence probes, led to the hypothesis that MntH2, contrary to common belief, is not a H^+ symporter.

MntH2 was attempted to crystallise and in initial screens some conditions were identified which could be a basis for optimisation in future trials.

Contents

List of Figures

LIST OF FIGURES

List of Tables

List of Abbreviations

ADP . . . . . adenosine diphosphate

APS . . . . . ammonium persulfate

ATP . . . . . adenosine triphosphate

BCA . . . . . bicinchonic acid

BLM . . . . . black lipid membrane

BSA . . . . . bovine serum albumin

CD . . . . . circular dichroism

CHES . . . . . *N*-cyclohexyl-2-aminoethanesulfonic acid

CMC . . . . . critical micellar concentration

CNT . . . . . concentrative nucleoside transporter

CDF . . . . . cation diffusion facilitator

CPM . . . . . 7-diethylamino-3-(4'-maleimidylphenyl)-4-methylcoumarin

Cryo-EM . . . cryo-electron-microscopy

CV . . . . . columne volume

DDM . . . . . *n*-dodecyl-β-D-maltoside

DMNG . . . . decyl maltose neopentyl glycol

DPhPC 1,2-Diphytanoyl-*sn*-glycero-3-phosphocholine

DTT . . . . . dithiothreitol

E. coli . . . . . *Escherichia coli*

EC_{50} . . . . . half maximal effective concentration

EDTA . . . . . ethylenediaminetetraacetic acid

HEPES . . . . N-(2-Hydroxyethyl)piperazine-N'-(2-ethanesulfonic acid)

HRP . . . . . horseradish peroxidase

IM . . . . . (bacterial) inner membrane

IMAC . . . . . immobilised metal affinity chromatography

K_d . . . . . dissociation constant

K_M . . . . . Michaelis constant

LB . . . . . Luria broth (bacterial growth medium)

LCP . . . . . lipidic cubic phase

LS . . . . . light scattering

MBP . . . . . maltose binding protein

Me . . . . . metal (ion)

MES . . . . . 2-(*N*-morpholino)ethanesulfonic acid

MOPS . . . . . 3-(*N*-morpholino)propanesulfonic acid

Ni-NTA . . . . nickel-nitrilotriacetic acid

OGP . . . . . *N*-Octyl-β-D-glucoside

PBS . . . . . phosphate buffered saline

PEG . . . . . polyethylene glycol

POPC 1-Palmitoyl-2-oleoyl-sn-glycero-3-phosphocholine

PNS . . . . . post nuclear supernatant

SB . . . . . super broth (bacterial growth medium)

SDS . . . . . sodium dodecyl sulfate

SDS-PAGE . . SDS-polyacrylamide gel electrophoresis

SEM . . . . . standard error of mean

SEC . . . . . size exclusion chromatography

SEC-MALS . . SEC-multi angle light scattering

SSM . . . . . solid-supported membrane

SURFE^{2}R . . Surface electronic event reader

TBS . . . . . Tris-buffered saline

TBS-T . . . . . Tris-buffered saline with Tween® 20

TEMED . . . . N,N,N',N'-Tetramethylethylenediamine

TMB . . . . . 3,3',5,5'-Tetramethylbenzidine

Tris . . . . . tris(hydroxymethyl)aminomethane

UV . . . . . ultraviolet (radiation)

Chapter 1

Introduction

1.1 Introduction to membrane transport and related terminology

In biological organisms, phospholipid bilayer membranes separate cells from their environment and in eukaryotes they make the border between the interior of organelles and the surrounding cytoplasm [1]. The large hydrophobicity of these membranes provides an effective barrier for ions and polar molecules, which cannot diffuse from one side to the other due to the large energy "penalty" when passing the membranes hydrophobic core. The function of facilitating or promoting the traffic of ions and small compounds with low membrane permeability is taken by transmembrane transport proteins. The term "transmembrane transport" has been used to describe different processes. In this thesis the term "(trans)-membrane transport protein" in-

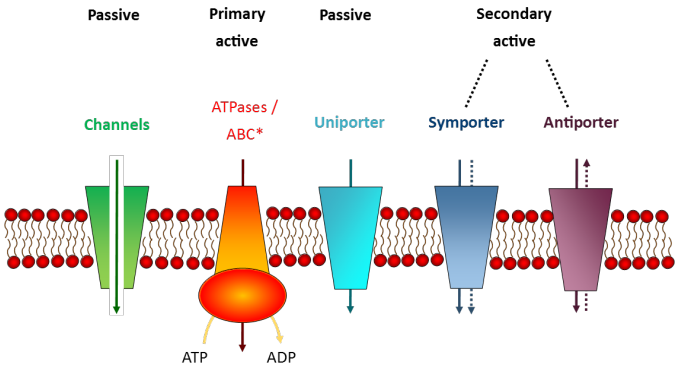

Figure 1.1: *Functional classification of membrane transport proteins. Transport directionality of substrates and cosubstrates are depicted by arrows, where dashed arrows are used to indicate cotransport. Channels and uniporters operate both in a passive mode, but there are other features to distinguish the two classes (see text). *ABC stands for ATP-binding cassette transporters which, as ATPases, use the energy from ATP hydrolosis to drive transport.*

cludes all classes of proteins involved in membrane traffic as shown in fig. 1.1. Fig. 1.1 indicates that there are three fundamentally different ways how transport of substrates is driven in these proteins. Ion channels and uniporters do not use any external energy source to drive transport. Hence, they equilibrate the concentration of their substrate on both sides of the membrane to a thermodynamic minimum. Substrate transport is said to be "passive" [2]. Other membrane transporters are powered by an external energy source and are able to transport their substrate against a concentration gradient. Some transporters use ATP, which is a primary energy source. Hence they are referred to as "primary active" transporters and include the family of the ATPases and the ABC-transporters. Finally, a large class of proteins couple the unfavourable process of substrate transport to a thermodynamically favourable transport of a co-substrate [3]. The

co-substrate is usually a small cation like H^+ or Na^+. These are secondary energy sources, because in order to maintain a gradient of the co-substrate, ATPases are needed, that use the primary energy source ATP. Transporters using a cosubstrate are therefore referred to as "secondary active" transporters. It should be mentioned that in some textbooks the uniporters are also referred to as secondary active transporters. This is inconsitent, however, because the term "active" suggests that substrate can be transported uphill, which is not the case for uniporters. From a thermodynamic view point, the uniporters are in fact much more similar to ion channels [2]. Still, it can be useful to have a general term for uni-, sym and antiporters, as these protein classes have several properties in common. A possible choice would be to use simply the term "transporter". The problem with this term is that it is not very well defined and depending on the context it may include primary-active transporters and even ion channels. To avoid ambiguities it would therefore be better to use a different term, but the problem is, that alternatives are lacking. The approach used in this thesis, is that, whenever possible, the term SoLute Carrier (family) transporters (SLC-transporters) is used. SLC-transporters form a large family of membrane transporters that has enlisted all human uni-, sym- and antiporters. They will be introduced in section 1.5.

Of the two proteins investigated in this thesis one (TRPM2) is an ion channel and the other one (MntH2) is an SLC-transporter homologue. TRPM2

will be introduced first, starting with a general introduction section about ion channels (1.2) followed by more specific sections about TRP-channels (1.3) and TRPM2 (1.3.2). The same structure will be applied to introduce MntH2, starting with a general section about transporters (1.4), then SLC-transporters (1.5), followed by sections introducing the SLC11 family (1.6) and bacterial SLC11 homologues to which MntH2 belongs (1.7).

1.2 Ion channels

1.2.1 Thermodynamics of ion transport

Before ion channels are discussed in detail some basic thermodynamics concepts will be introduced. Transport in ion channels is passive, meaning no external energy source is required to drive ions through the channel [1]. The channel provides a pore through which ions diffuse freely, but selectively. Diffusion of ions is directed by two factors. The first one is the concentration difference of an ionic species between the two sides of the membrane. Diffusion drives ion flow from higher to lower concentration until concentrations are equal on both sides. The free energy released in that process is described by eq. (1.1):

$$\Delta G = RTln\left(\frac{[A_{in}]}{[A_{out}]}\right) \tag{1.1}$$

In this equation, ΔG is the difference in Gibbs free energy, R is the universal gas constant, T the temperature and A_{in} and A_{out} are the concentrations of

the solute on the cytoplasmic and on the extracellular side of the membrane respectively. A look at the physiological ion concentrations in biological systems will show that ion distribution can be highly asymmetrical. In mammals, for instance, the concentrations of Na^+ and K^+ are highly imbalanced between in- and outside of cells. Concentrations are ca. 150 mM Na^+ and 4 mM K^+ in the extracellular fluid and ca. 140 mM K^+ and 12 mM Na^+ in the cytoplasm. Apart from the concentration gradient, the direction of ion flow is influenced by a second factor, which is the membrane potential. The membrane potential is a reflection of the difference in the sum of electrical charges between the two sides of the membrane. In case of the cell membrane, there is an excess of negative charges on the cytoplasmic side, whereas the extracellular side is positively charged. Ions are attracted to the side that has a total charge opposite their own charge. To account for the membrane potential the eq. 1.1 is modified by an additional term:

$$\Delta G = RTln\left(\frac{[A_{in}]}{[A_{out}]}\right) + zF\Delta\Psi \tag{1.2}$$

In eq. 1.2 F is the Faraday constant, z is the ionic charge of A and $\Delta\Psi$ is the membrane potential.

The membrane potential results from a combination of passive and active transport of certain ion species across biological membranes. In typical animal cells, for instance, the largest contribution to the membrane potential is

made by passive transport of permanently open potassium channels. These channels allow potassium ions, that have a high concentration in the cytoplasm to diffuse out. In doing so, the cytoplasmic side becomes negatively charged, which stops potassium concentrations from equilibrating. Sodium ions, that are present in excess on the extracellular side, are very much attracted to he cytoplasmic side, but they have a low membrane permeability. As a consequence the system cannot reach its thermodynamic minimum and a membrane potential is constantly maintained. The Na^+/K^+-ATPase assists this process by electrogenic transport of K^+ into- and Na^+ out of the cell. The magnitude of the membrane potential can be calculated by using the Goldman-Hodgin-Katz equation for monovalent ions (1.3). This equation takes into account the in- and outside concentrations of the three most abundant ions in biological systems (K^+, Na^+ and Cl^-) as well as the respective permeability of these ions.

$$\Delta\Psi = \frac{RT}{F} ln \left(\frac{\sum_i^n P_{M_i^+}[M_i^+]_{out} + \sum_j^m P_{A_i^-}[A_i^-]_{in}}{\sum_i^n P_{M_i^+}[M_i^+]_{in} + \sum_j^m P_{A_i^-}[A_i^-]_{out}} \right) \tag{1.3}$$

For obvious reasons anions and cation show opposite behaviour with respect to their position in the fraction and therefore a letter M is used for cationic species and A for anionic species. P is assigned for ion permeability coefficients. To calculate physiological membrane potentials, generally only Na^+, K^+ and Cl^- ions are considered. Evaluating equation 1.3 will typically re-

sult in values for membrane potentials between -40 and -80 mV, depending on cell types.

1.2.2 Structural architecture of ion channels

Ion channels are designed to enable a rapid passage of ions such as Na^+, K^+, Ca^{2+} and Cl^- across biological membranes. They form essentially a hydrophilic pore through which selected ions diffuse freely from one side to the other. Ion channels have in common two main features that are important for their function: A selectivity filter, that allows only certain species of ions to pass, and a gate, that can be opened and closed depending on external stimuli. The nature of the stimulus determines whether an ion channel is classified as a ligand-gated, signal-gated, voltage-gated or mechano-sensitive channels (fig. 1.2). Some channels, like for instance several members of the

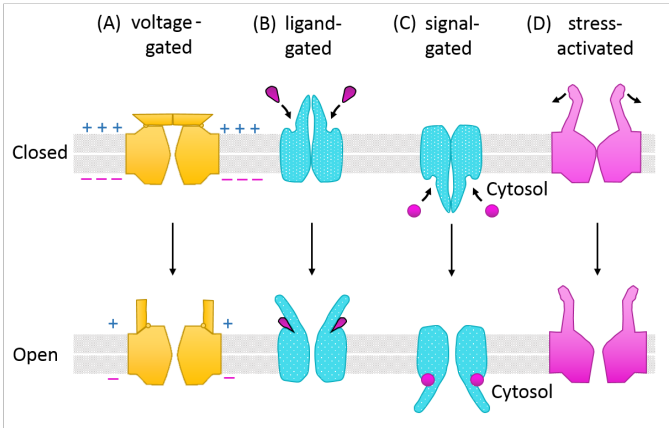

Figure 1.2: *Different classes of ion channels. (A): Voltage-gated channels respond to changes in membrane potential. (B) and (C): Ligand-gated and signal-gated channels respond to binding of a molecule to the extra-/intracellular side. Often these two classes are not distinguished and are both referred to as ligand-gated channels. (D): Stress-activated channels may be gated by different mechanisms. The depicted mechanism could occur in channels that are abundant in auditory hair cells in the ear basilar membrane. Figure adapted from [4].*

TRP family, show a more complex activation pattern and their state of transport depends on a combination of stimuli.

To give a general introduction on the molecular basis of ion channel pores, KcsA will be discussed as a model channel. KcsA is one of the best characterised and most intensively investigated channels. The structure of (truncated) KcsA was solved in 1998 by Doyle et al. [5]. KcsA is a bacterial

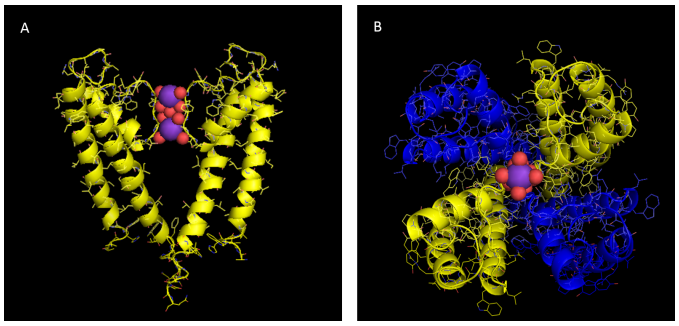

Figure 1.3: *Structural representation of the bacterial potassium ion channel KcsA. A: Pore with selectivity filter viewed from the membrane plane. From this perspective one can see the inverted tipee arrangement where the top of the tipee forms the gate at the intracellular side. The potassium ions in the selectivity filter (purple) and the coordinating oxygen ligands (red) are shown in a space filling representation. For better view the two subunits in the front and the back of the pore have been omitted. B: Top view from the extracellular side. This view shows the tetrameric architecture of the core that is found to be similar in most ion channels. One can also guess the 8-fold coordination of the hydration shell of the potassium ion in the selectivity filter. Figure made with PyMOL [6].*

potassium channel from *Streptomyces lividans* and it is activated at low pH [7]. There are several reasons why KcsA is such a good model system. First of all its structure is very simple: Like other potassium channels, it is tetrameric, but its monomer contains only two transmembrane helices. It is much more common for ion channels to have six transmembrane helices instead. Also KcsA's primary sequence is very homologous to the pore re-

gion of eukaryotic voltage-gated potassium channels. The structure of KcsA contributed to a large extent to solve one of the most puzzling questions at the time: It was hard to understand how ion channels could transport their substrate with such great speed, close to the diffusion limit, and at the same time provide such a high selectivity: KcsA has a greater than 10000-fold selectivity of potassium over sodium. The problem was that high substrate selectivity is usually associated with a high specificity of the binding site. High specificity, at the same time, implies a strong affinity for the substrate. But a strong affinity would slow down transport, because the rate of substrate release would become a limiting factor. The structure of KcsA answered this conundrum, in particular because the crystals included potassium ions in the selectivity filter (fig. 1.3)

As mentioned, KcsA is a tetramer, where each monomer contributes two transmembrane helices, named M1 and M2. The M2 segments form the pore in what has been called an "inverted teepee" arrangement, where the pinnacle of the teepee is on the cytoplasmic side and the base faces the extracellular side. This provides a large cavity within the membrane with a maximal diameter of ca. 10 Å, that enables K^+ ions to reside there in hydrated form (fig. 1.3). The selectivity filter, which lies adjacent to the cavity, is much narrower with a width of ca. 3 Å, that forces ions to strip off their hydration shell. This process requires energy, which slows down ion translocation. However, the filter is lined with oxygen-ligands from backbone

carbonyl-oxygens that arrange in a way that closely resembles the geometry of the water-oxygen atoms in the potassium hydration shell. This minimizes the energy required for dehydration and rehydration of K^+ ions and so they can pass through the filter still with a very high turnover. Na^+ ions, on the other hand, are too small to coordinate well with the backbone oxygens of the selectivity filter, which considerably hampers their passage. This explanation answers the question about high selectivity with simultaneous high speed K^+-conduction on a basic level. For the same reason this section will spare a detailed discourse about the gating mechanism. What has to be mentioned in this regard is that there is a conserved glycine residue in M2 that acts as a hinge between open and closed state. In related channels the hinge residue may also be a proline.

The last issue topic that will be illustrated by the example of KcsA is channel inactivation. So far it has been assumed that there are only two states that a channel can adopt: An open and a closed state. However, in some channels a third state can occur, which is the inactivated state. The inactivated state describes a configuration of the protein that is not ion-conducting, regardless of whether the gate is open or closed. In K^+ channels two types of inactivation can occur: N-type and C-type inactivation. N-type inactivation describes the autoinhibitory blocking of the pore by a ball-shaped domain located on the N-terminus. C-type inactivation is often a slow inhibitory process that deforms the cavity of the selectivity filter and thereby stops ion

translocation. Structural details of this process are known from a study on KcsA where several structures in transition to an inactivated state of this channel have been solved showing a stepwise deformation of the backbone of the selectivity filter [8]. This work will not be discussed in detail here, but it is worth noting that C-type inactivation has been reported to occur in the TRPM2 channel [9].

Structures from different types of potassium channels, including the voltage sensitive K^+-channels K_vAP [10] and K_v 1.2 [11], the bacterial inward rectifier K^+-channel KirBac 1.1 [12] and the calcium activated K^+-channel MthK [13] gave insights into voltage and ligand-gating mechanisms. These structures revealed that all the channels were tetrameric and that in general the architecture of the pore shows great similarity to KcsA. Most of these channels, with the exception of KirBac 1.1, differ from KcsA in that they have six TM helices instead of two. The transmembrane helices are generally labelled S1 to S6, where S5 and S6 are homologous to the M1 and M2 helices of KcsA. The first four helices may be involved in the gating mechanism, but the exact function may vary depending on the type of channel activation. In voltage sensitive channels, for instance, the S4 helix is rich in positively charged amino acids and thereby acts as a voltage sensor. Continuing with the example of voltage gated channels, the arrangement of the transmembrane part of the protein is very similar when comparing K^+ channels to channels conducting Na^+ or Ca^{2+} [14–16]. The main topological difference

of Na^+ and Ca^{2+} channels compared to K^+ channels is that rather than forming a tetramer, these channels consist of a single chain that adopts a pseudotetrameric fold [17]. Regarding the selectivity filter, it is noteworthy that it is wider for Na^+ and Ca^{2+} channels, which implies that these ions are transported at least partially hydrated, as their ionic radii are smaller compared to K^+ [14]. Another difference is that in the selectivity filter of Na^+ and Ca^{2+} channels the ion coordination sites are partly formed by amino acid side chains, whereas in K^+ channels K^+ is coordinated solely by backbone oxygens. By having side chains as part of the coordination sites, amino acid substitutions can modify the charge density inside the filter cavity, e. g. by varying the number of positively and negatively charged amino acids. As a consequence, a channel can be made more selective for either Na^+ or Ca^{2+} ions and studies have shown that by making appropriate mutations of amino acids in a conserved sequence, the selectivity of a Na^+ channel can be shifted towards Ca^{2+} selectivity [16].

Anion channels constitute a very intricate and interesting category of proteins. Some anion channels actually are classified as SLC26 transporters [18] and therefore are covered in section 1.5. Even the ClC channels, of which the structure of two bacterial homologues has been solved [19], have been found in many cases to be in fact Cl^-/H^+-exchangers [20]. For this reason, and the fact that anion channels have not been the subject of this thesis, they will not be further introduced here.

1.3 TRP channels

Transient receptor potential (TRP) channels form a large family of non-selective cation-channels [21–24]. The first TRP channel was discovered in *Drosophila melanogaster* where a spontaneous mutant led to an unusual response to steady light which appeared to be transient in contrast to the sustained response in wild-type flies [25] (Hence the name of these channels). Homologous channels found in eukaryotes have been classified into six subfamilies based on their protein sequence homology: TRPC (canonical) [26, 27], TRPV (vanilloid) [28], TRPA (ankyrin) [29], TRPP (polycystin) [30], TRPML (mucolipin) [31–33] and TRPM (melastatin) [34]. To a large extent TRP channels are involved in the molecular mechanisms of sensory perception in humans [23]. This includes touch, taste and smell, but also in hearing and vision TRP channels may play a crucial role. Because of their function as primary sensors, TRP channels naturally respond to a great variety of physical and chemical stimuli. A prototype TRP channel is TRPV1 that responds to a wide range of structurally unrelated vanilloid ligands [35, 36]. These include capsaicin (the pungent compound of hot peppers), resiniferatoxin (a chemical found in the cactus *Euphorbia resinifera*), piperine (the pungent extract of black pepper) and camphor (a strongly smelling compound extracted from *Cinnamomum camphora*, commonly known as the camphor tree). In addition, the channel is activated by some spider-toxins,

including the double-knot toxin DkTx, which is a short peptide of 75 amino acids [37]. Apart from ligand binding, TRP channel activity may depend on other factors including temperature [35, 38–44], membrane voltage [45–48], post-translational modifications such as phosphorylation [49] and ubiquitination [50], as well as the presence of certain membrane lipids, especially phophatidylinositol(4,5)biphosphate (PIP2) [51–53]. Because of the large variety of functions and activation mechanisms even among TRP subfamilies it is impossible to give a concise overview of this aspects of the family. Detailed lists of all human TRP channels together with their proposed activation mechanism and physiological functions have been published elsewhere [22].

Structural research on TRP channels has been challenging in the past, as it is for all eukaryotic membrane proteins. However, relatively recently, structures of several TRP channels have been published using cryo-EM, which gave some exciting new insights. The first published high-resolution structure appeared in 2013 and was of TRPV1 [54]. Subsequently, also high-resolution structures of TRPA1 [55], TRPV2 [56, 57] and TRPV6 [58] were published. From these structures it was found that the transmembrane core of TRP channels is structurally similar to voltage gated potassium (K_v) channels. Like K_v-channels, TRP channels are tetrameric and one monomer consists of six transmembrane helices, where S5 and S6 of each subunit form the pore. Helices S1-S4 are equivalent to the voltage sensing domain, even

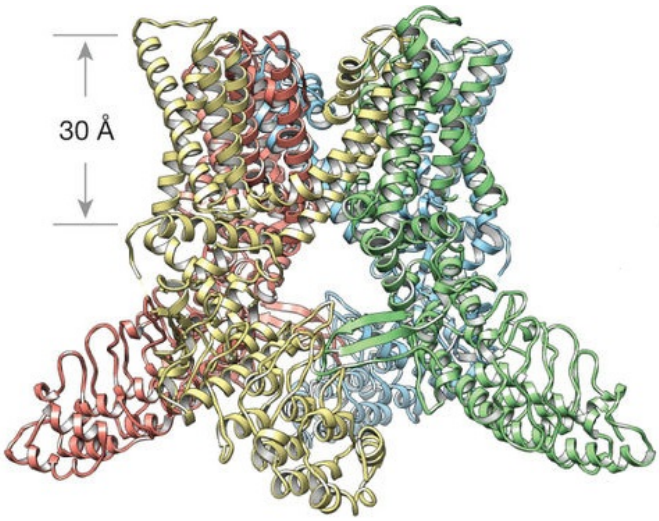

Figure 1.4: *Structural representation of the TRPV1 ion channel based on data from cryo-EM. The structure revealed a core architecture that is similar to the one of KcsA and other voltage gated ion channels (figure with permission from [54]).*

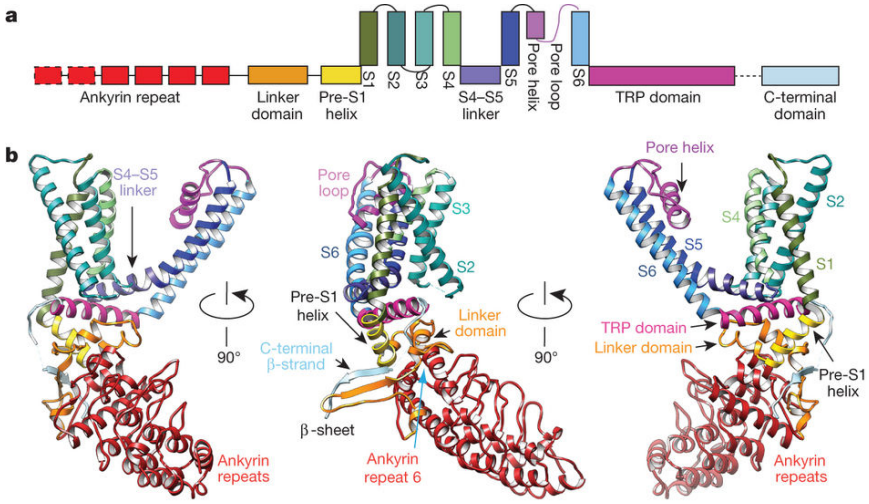

Figure 1.5: *a: Linear diagram of structural domains of TRPV1. Typical features for TRP channels are the ankyrin repeat and the TRP domain. Dashed lines indicate lack in electron density of that part b: Cartoon representation of TRPV1 monomer. The coloring matches with the diagram in a. From this view the positioning of the TRP domain can be identified which is parallel to the membrane plane close to the cytoplasmic side (figure with permission from [54]).*

though in voltage insensitive TRP channels, like TRPV1, helix S4 is not rich in charged residues. Of the published structures of TRP channels so

far, the one of TRPV1 is particularly insightful, because it has not been only solved in its apo-state (without ligand) but also with different ligands [59]. An interesting observation was that binding of activating vanilloid lig-

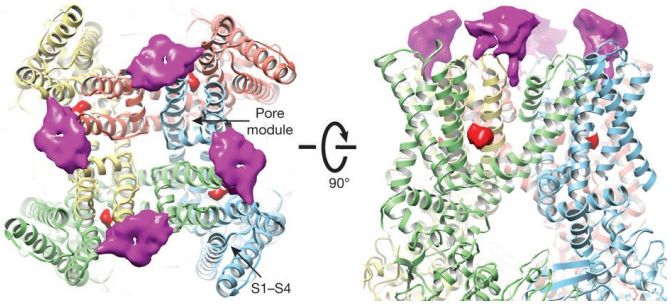

Figure 1.6: *Cryo-EM structure of TRPV1 core domain bound to two of its activators: capsaicin (red electron density) and Dktx (purple electron density). The structure reveals that these ligands bind to sides that are very far apart from each other. This illustrates the complexity of the activation mechanism in TRP channels (figure with permission from [59]).*

ands (capsaicin/resiniferatoxin) takes place in a very different location than binding of the spider toxin. Intriguingly, the channel appeared to be in a different state of activation depending on the nature of the ligand. Only the spider toxin, which binds to the outer pore region of TRPV1, causes the channel to adopt a fully open state. The vanilloid activators, which bind in a membrane buried region between the S4 and S5 helix, cause only a partial opening of the channel. This illustrates the complexity of TRP channel regulation and the challenges involved in getting a detailed understanding of the gating mechanisms.

1.3.1 The TRPM subfamily

The TRPM sub-family has been named after its first member, melastatin (TRPM1), which is predicted to be a tumour suppressor [34, 60]. So far eight members of this family have been described, for which a large variety of physiological functions have been proposed. Some of them (TRPM1, TRPM5, TRPM7 and TRPM8) appear to have a role in sensing, where the function of TRPM8 as a cold sensor is presumably the best established [43, 44, 61]. TRPM5 is expressed in taste bud cells and is supposed to be involved in the sensing of bitter, sweet and umami taste [62]. TRPM7 has been proposed as a shear stress sensor, but this hypothesis has not yet been proven [63, 64]. Finally, the tumor repressor TRPM1 also is involved in the light response in ON bipolar retinal ganglia cells [65]. For the majority of the TRPM channels, increasing evidence suggests that they are not involved in perception, but take on different functions, including contributing to maintaining homeostasis and organ function [66]. TRPM2, the channel under examination in this thesis, has been identified as a sensor for oxidative stress, which appears to be one of its key roles [67–71]. Potentially, TRPM4 and TRPM7 are also involved in oxidative stress sensing [72–79], but their contribution is less significant. The high diversity of functions among TRPM members is also reflected by the varying cation selectivity between the different channels. TRPM4 and TRPM5 are non permeable to Ca^{2+} [80], whereas the remaining members of the family show varying

selectivities between mono- and divalent cations. A peculiar feature of three TRPM family members (TRPM2, TRPM6 and TRPM7) is that their C-termini form a domain that carries out enzymatic activity. TRPM6 and TRPM7 exhibit α-kinase activity [81, 82] and TRPM2 catalyzes hydrolysation of ADP-ribose [83, 84]. A summary of TRPM family cation selectivity, physiological functions and cellular expression is given in table 1.1.

1.3.2 TRPM2

TRPM2 (formerly also called TRPC7 or LTRPC2) was the first target for biophysical characterisation in this thesis. Compared to other channels of the TRP family, it is fairly large with a monomer molecular weight of 173 kDa. It is expressed in a variety of tissues or cell types including the brain, bone marrow, neutrophils [85–87], lung, spleen, eye, heart and liver [84]. Whereas generally TRPM2 has been found located in the cell membrane, in pancreatic β-cells TRPM2 was found to be expressed as well in the lysosomes [88]. It is possible that TRPM2 is located elsewhere as well, because in a stable overexpressing HEK293 cell line, TRPM2 is also found in mitochondria [89]. TRPM2 is widely considered to be an oxidative stress sensor after it was found that Ca^{2+} influx via TRPM2 regulates H_2O_2-induced cell death [90, 91]. Additional functions have been proposed for TRPM2 involving maturation of dendritic cells and chemotaxis, as well as insulin secretion [66]. Furthermore, TRPM2 has been associated with a number of

Channel	Selectivity P_{Ca}/P_{Na}	Cellular expression	Physiological functions
TRPM1	ND	Skin melanocytes, retinal bipolar ganglia	Light response in ON bipolar retinal ganglia cells; tumor repressor in melanoma cells
TRPM2	0.5-1.6	Brain, bone marrow, peripheral blood cells (neutrophils), lung, spleen, eye, heart and liver	Oxidative and nitrosative stress response; activation of granulocytes; pancreas insulin release; critical in apoptosis
TRPM3	1.6-2.0	Primarily in kidney; lower in brain, sensory neurons, testis, ovary, pancreas and spinal cord	Steroid hormone (pregnanolon) sensor; possible regulator in endocrine pancreas,glia cells and cerebellar Purkinje cells
TRPM4	selective for monovalent cations	Heart, exo- and endocrine pancreas, mast cells, smooth muscle, macula densa, lung and placenta	Mast cell degranulation (histamine release) and migration as a critical Ca^{2+}-impermeable cation channel regulating Ca^{2+} entry; catecholamine release from chromaffin cells; vasopressin release from paraventricular and supraoptic hypothalamic nuclei
TRPM5	selective for monovalent cations	Tongue (taste bud cells), lungs, testis, digestive system, brain, endocrine pancreas	Taste(sweet, bitter, umami); positive regulator of glucose-induced insulin release; trigeminal nasal chemoreception
TRPM6	$P_{Mg}/P_{Na} \sim 6$	Kidney, colon and intestine	Mg^{2+} homeostasis and reabsorption in kidney and intestine
TRPM7	3	Ubiquitous	Mg^{2+} homeostasis and reabsorption in kidney and intestine; cell cycle control; gastrulation; development of thymocytes (thymopoiesis); cell migration; shear stress sensor?; skeletogenesis?
TRPM8	1-3	Sensory dorsal root and trigeminal ganglia neurons, nodose ganglion cells innervating the upper gut, vascular smooth muscle cells, liver, gastric fundus, bladder (urothelium) and different tissues of the male genital tract; high in tumors from prostate, breast, colon, lung and skin	Thermo-sensation (cold); sperm motility, acrosome reaction

Table 1.1: *Expression, selectivity and function of human and mouse TRPM channels. ND: not determined. (table adapted from [22, 24])*

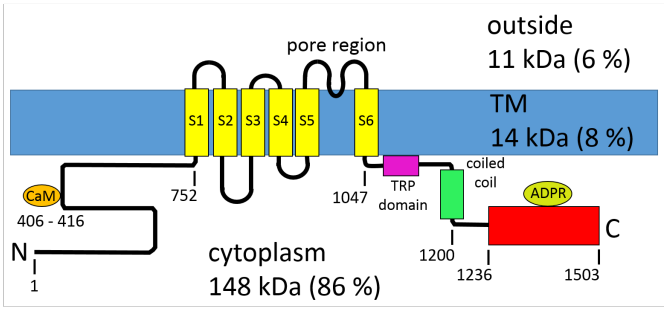

Figure 1.7: *Schematic representation of TRPM2 sequence. The protein consists of three main domains: A large N-terminal which includes a calmodulin binding site, a transmembrane domain, presumably strongly resembling that of K_v-channels, and a C-terminal domain that includes the TRP domain, a coiled coil domain and an ADPR-hydrolosis (NUDT9-H) domain. Figure adapted from [92].*

serious diseases. Its activation by H_2O_2 *in vivo* suggests a role in pathogenic processes which are characterised by an increased oxidative environment, including carcinogenesis, inflammation, neurodegenerative disorders, diabetes and others [90].

The modulatory mechanisms of TRPM2, like of most TRP channels, are very complex as has been shown in previous studies. The primary gating molecule is adenosine-diphosphate-ribose (ADPR; [90]), which binds with high specificity to the TRPM2 specific Nudix-like domain at the C-terminus (fig. 1.7). Considerable amount of work has been done to characterise TRPM2 in numerous patch clamping studies of different cell types [93–98]. Despite this large body of work there are still some issues that have not yet been fully resolved. For instance, the role of Ca^{2+} in gating is still not fully understood. Although it is widely agreed that in addition to ADPR, intracellular calcium ions ($[Ca^{2+}]_i$) are needed as co-activators to open the

channel [66], it is not quite clear whether Ca^{2+} ions bind independently or whether they mediate channel opening via calmodulin. Tong *et al.* claim evidence that activation occurs via calmodulin binding [99]. The authors used a calmodulin mutant that was made insensitive to Ca^{2+}. When TRPM2 was coexpressed with the calmodulin mutant, Ca^{2+} influx was suppressed which led to the conclusion that the mutant competes with the endogeneous calmodulin and stops it from activating TRPM2. In a further experiment it was shown with immunoblotting that calmodulin associates with TRPM2 in a region at the N-terminus (fig. 1.7). Later, Csanády *et al.* postulated that in addition to calmodulin binding, the channels has four Ca^{2+} binding sites that regulate channel opening [100]. Although it seems likely that bound and unbound Ca^{2+} affect the channel, results from biophysical studies could give a definitive answer to that question. Apart from ADPR and Ca^{2+}, a large number of other compounds also appear to have regulatory effects on TRPM2. These include ADPR related compounds such as cyclic ADPR (cADPR) [101, 102], nicotinamide adenine dinucleotide (NAD^+) [68, 84] and nicotinic acid adenine dinucleotide phosphate (NAADP) [102, 103], but also unrelated compounds such as reactive oxygen species (ROS), most notably H_2O_2 [68, 101]. The activation mechanism of these compounds, especially of H_2O_2, has been highly controversial in the past, as the debate has been on whether they are direct or indirect activators of TRPM2. From experiments, taking advantage of the inside-out patch-clamp technique, Toth *et*

al. claim that most of the compounds are indirect modulators [104], but it would be worth confirming this with a different technique.

Most studies on TRPM2 have focussed on the channel in the plasma membrane. Little work has been done yet on the characterisation of the lysosomal channel. The sensitivity of the channel towards changes in intra- and extracellular pH has been investigated by Starkus et al. [105] and they found a decrease in activity at lower pH. It remained unclear, whether the channel is able to conduct protons or not, or whether cotransport of protons with cations takes place. At least of equal importance is the question whether the channel is permeable to other cations such as Zn^{2+}. This is of significance in the context of the channel's potential role in cell death of pankreatic β-cells. It has been shown that activity of the lysosomal TRPM2 channel alone can lead to oxidative-stress induced cell death in mouse β-cells, but the pathway of apoptosis remains unknown. There is evidence that TRPM2 releases Zn^{2+} from the lysosomes, which would explain the occurence of cell death, as free Zn^{2+} is toxic [106]. But cell death is not the only process in which TRPM2 has potentially a detrimental role. Experimental evidence suggests that TRPM2 is directly linked to type II diabetes. A study using TRPM2 KO mice showed that mice not expressing the channel were protected from diet-induced obesity and insulin resistance [107]. Inhibiting TRPM2 therefore should help to prevent type II diabetes. Besides biophysical characterisation of TRPM2, a declared goal of this project was to establish a stable

assay for screening compounds inhibiting TRPM2. A chemical library for this purpose has been designed in preceeding work. Here it was attempted to screen this library to identify the direct inhibitors to be used for iterative screening.

1.4 Transporters

For reasons outlined in section 1.1 the term "transporter" used as a title of this section refers to secondary active- and passive transporters only. Secondary active transporters include a co-substrate, like Na^+ or H^+, in the transport mechanism, that moves down its electrochemical potential gradient. The free energy of this downhill movement is then coupled to uphill transport of the substrate. Depending on the directionality of co-transport, the transporter is referred to as a sym- or antiporter (fig. 1.1). Uniporters do not use a cosubstrate and are initiated only by a transmembrane gradient of their own substrate. What all transporters have in common, and distinguishes them from ion channels, is that they operate in an "alternative access" mechanism. This means that the protein alternates between two conformations: An outward facing conformation, that allows access of substrate only from the extracellular side and an inward facing conformation that can only take up substrate from the cytoplasmic side. It is nowadays assumed in general that some occluded states are involved in the transport cycle as well, where the substrate is shielded completely from either bulk solution ([109], fig.1.8). Membrane transport following this mechanism can

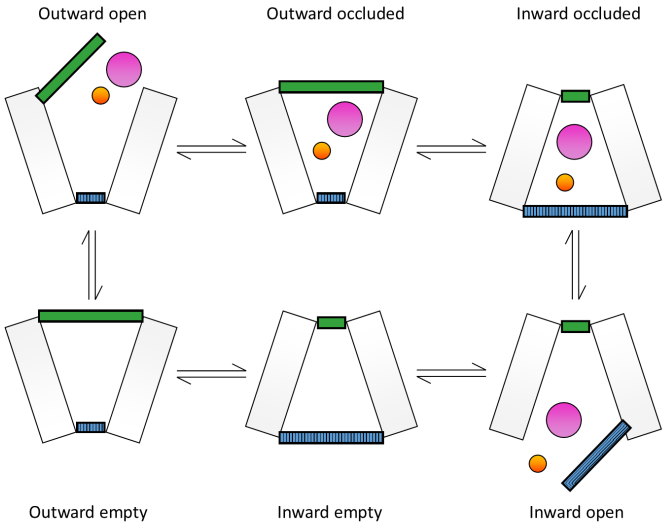

Figure 1.8: *Illustration of a transport cycle following an alternating access mechanism. A symporter mechanism is shown for this example. Apart from outward open and inward open states the cycle contains as many as four occluded states (figure adapted from [108]).*

be written as a chemical equation. For a transporter molecule P exporting a substrate S out of the cell this would look as follows:

$$\mathrm{S_{in}} + \mathrm{P} \rightleftharpoons \mathrm{PS} \xrightarrow{k_{transport}} \mathrm{P} + \mathrm{S_{out}} \tag{1.4}$$

Thereby PS represents the substrate bound transporter, $k_transport$ is the rate constant of substrate transport and S_{in} and S_{out} is the substrate in- and outside of the cell respectively. It turns out that this equation is equivalent to an enzyme catalysed reaction where Michaelis Menten kinetics applies. Therefore, a Michaelis constant can be defined analogously:

$$v_0 = k_{transport}[PS] = \frac{v_{max}[S]}{K_M + [S]} \tag{1.5}$$

Where K_M is the Michaelis constant and v_0 is the initial velocity of transport. This implies that at high substrate concentrations, transport velocity is limited by the number of proteins available. Based on kinetic data it is therefore possible to distinguish whether a protein has an alternating access transport mechanism or whether it behaves like an ion channel.

1.5 The solute carrier family

The solute carrier (SLC) nomenclature system has been introduced only in the 1990s. Essentially, the idea of that system was to assign all human genes of membrane transporters, that do not belong to any of the remaining classes (ion channels, aquaporins and primary active transporters) to a large superfamily [110]. Consequently, the SLC family is very diverse and its members are responsible for transport of a large variety of substrates. Most of these are small organic molecules such as amino acids, sugars or neurotransmitters, but some also transport ions or larger molecules, including oligopeptides. Up to date there have been 52 subfamilies identified which account for more than 400 human genes [110].

Structural information about SLC-transporters is available mostly from crystal structures of bacterial homologues. Up to 2017 only three human SLC structures have been published [111–113]. From a structural point of view, SLC-transporters are very different from the classical ion channels, that have been introduced in the previous sections. Perhaps surprisingly, despite having highly diverse function and substrates, there have only been identified

a few different folds of SLC transporters that are shared among the many different members of the SLC family. One of the most predominantly occurring folds is the LeuT-fold, named after the protein where this fold has been first discovered [114]. Another common fold is the major facilitator superfamily fold (MFS-fold). This fold is named after the protein family for which the structures of two members were released in 2003 (the glycerol-3-phosphate/phosphate antiporter GlpT and the proton-coupled lactose symporter LacY) [115, 116]. Finally, a group of transporters shows distinct folds that are not widely shared among other members. Examples include the glutamate transporter GltPh [117], the Na^+/H^+-antiporter NhaA [118] and the concentrative nucleoside transporter VcCNT [119]. For a complete list see ref. [2]. Progress has also been made in elucidating the transport mechanism of these proteins. As expected, they all display an alternative access mechanism, but the way it is implemented varies between proteins of different folds. Although not conclusive, it is thought that all proteins adopting a similar fold share the same principal mechanism. Two of these mechanisms, the so called rocker-switch and the rocking-bundle mechanism, are conceptually related and are based on the principle of a moving-barrier. What this means is illustrated in fig. 1.9. The barrier is formed at the interface of two domains that interact in close proximity. This interaction is formed close to one of the membrane surfaces so that from that side the barrier completely blocks access to the substrate binding pocket, which is

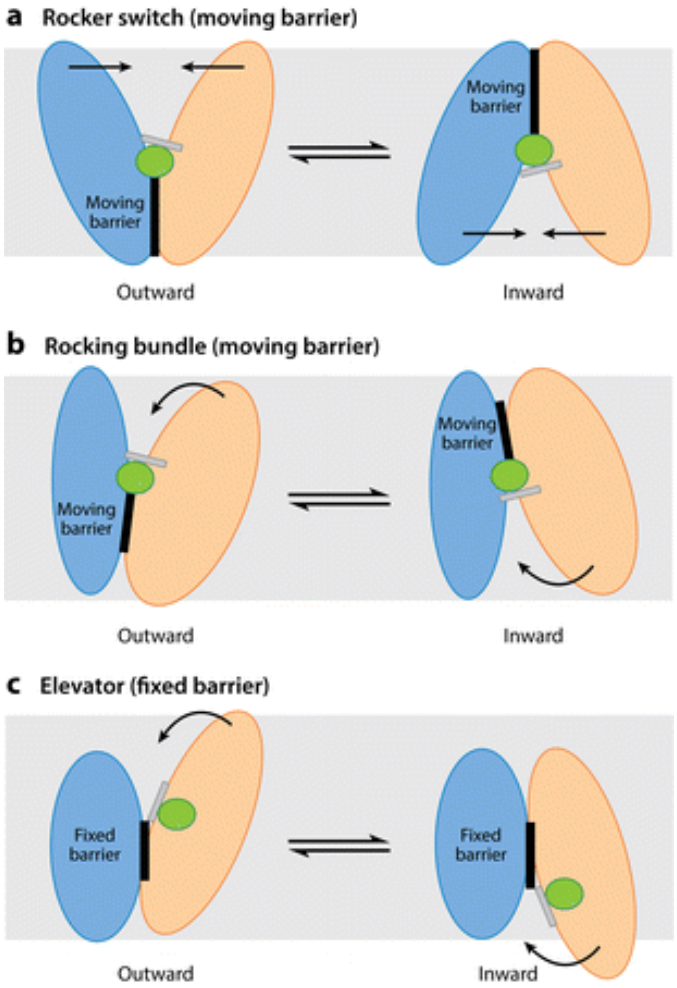

Figure 1.9: *The three general transport mechanisms in SLC transporters. a: The Rocker switch mechanism is found in MFS-folded transporters and features two domains which at their interface form a barrier which keeps the substrate from passing. During the transport cycle the two domains move around the substrate binding pocket. Thereby the barrier is being taken apart but if will reform at the side which previously was accessible to the substrate.From the principle this mechanism works very much like a water lock, where of the two doors, only one is open at a time b: The Rocking bundle mechanism is very similar to the Rocker switch mechanism and also follows the concept of the water lock ("moving barrier"). c: The elevator mechanism is different from the other two, because it has a fixed barrier (figure from [2]).*

located about in the middle of the membrane. Towards the other end, the binding pocket is shielded only by a thin gate. During substrate translocation the domains move apart and the barrier is broken. At the same time the domains approach each other on the other side of the membrane and eventually they will close up to reform the barrier. The barrier has now moved so that the accessibility of the substrate binding pocket has changed sides.

Mechanisms involving a moving barrier are the ones that have been most commonly found in transport proteins. Crystal structures so far showed that proteins adopting the LeuT-fold are displaying the rocking-bundle mechanism and MFS-fold proteins are operating on the basis of a rocker-switch mechanism. The difference between the two mechanisms, as based on fig. 1.9, may appear rather subtle. Indeed, the main distinction is that in a rocker-switch mechanism the barrier is formed by two structurally similar domains, which both undergo movement during substrate transport, whereas in the rocking-bundle mechanism the two domains share no analogy and only one domain is moving.

In contrast to the above, the third mechanism shown in fig. 1.9 is very different from the first two in that there is a fixed barrier between two domains. One of these domains is a moving domain that binds to the substrate on one side and then translocates it all the way to the other side before releasing it again. Remarkably, it has been found that this elevator type mechanism

is shared by proteins which do not have a common fold. Among these are GltPh [120], NhaA [121] and VcCNT [119] and there are more proteins displaying a rare or unique fold predicted to work according to an elevator-type mechanism [2].

1.5.1 The LeuT fold and mechanism

To examine substrate transport more closely, one of the mechanisms will be explained in more detail by taking aid of a model protein for which in-depth research on that matter has been done. Several model proteins could be considered for this introduction, but LeuT seems to be the most obvious choice. This is not only because the LeuT fold and its corresponding rocking bundle mechanism are very common and well studied. Even more important is the fact that homologues of the SLC11 family, the same family to which belongs MntH2, have been crystallised in this fold [122, 123]. The first LeuT structure was solved from the bacterium *Aquifex aeolicus* and appeared in 2005 [114]. It reveiled a fold that was unique at that time and therefore it was named after this protein. To understand what defines the LeuT-fold, it is best to have a look at its membrane topology (fig. 1.10). There are two main characteristics of the LeuT fold. The first is a two-fold pseudosymmetry axis in the plane of the membrane that relates five transmembrane helices to the consecutive five. In LeuT these are TM1-TM5 that are symmetric to TM6-TM10, but in other LeuT fold transporters these numbers may be different. This feature may be called a '5+5' inverted structural

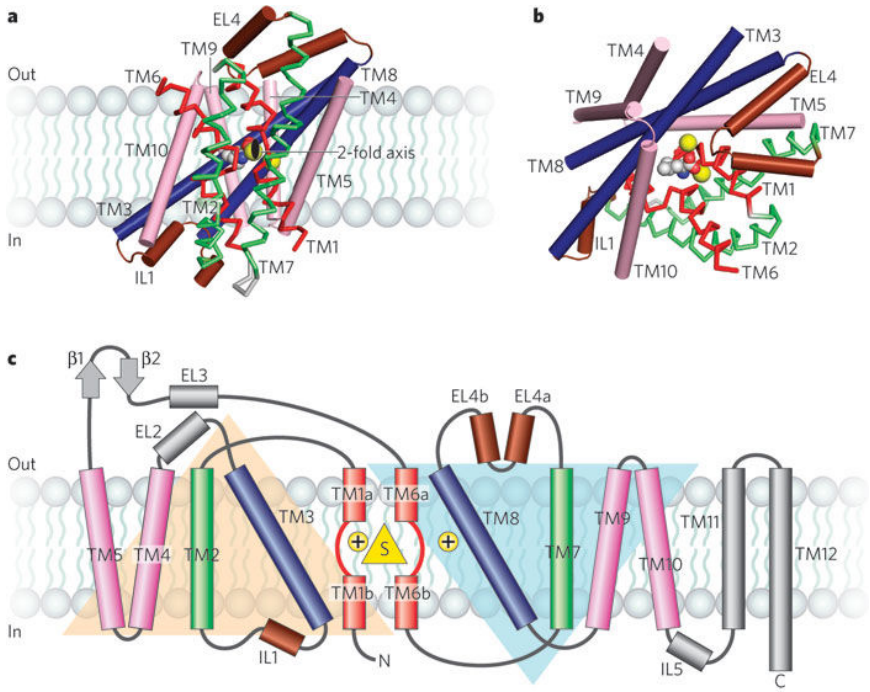

Figure 1.10: *Illustration of the LeuT fold. a: Representation of the LeuT structural arrangement in the membrane. Helices that are part of the scaffold domain (TM3-TM5,TM8-TM10) are depicted as rods and helices belonging to the core domain (TM1,TM2,TM6,TM7) are shown in a stick representation. Not shown are TM11 and TM12 that don't contribute to the signature LeuT fold. The two-fold axis parallel to the membrane plane is indicated and coincides with the substrate binding pocket. b: Same as a but with view from top of the membrane. The bound substrate (carbon, grey; oxygen, red; nitrogen,blue) and sodium ions (yellow) are shown. c: Topology diagram of LeuT. The helices are represented in the same color as in a. The diagram reveals the architecture with the substrate (depicted as a yellow triangle) bound in the center. The pseudosymmetric fold of the 5+5 helices around the substrate is emphasized by the two orange and blue colored triangles [124].*

symmetry motif. The second common signature is that the first two helices of the inverted repeat (TM1 and TM6 in LeuT) are not continuous, but are interrupted in the middle by a few residues (including e.g. a proline and glycine), which do not adopt an α-helical fold. These non-helical parts of TM1 and TM6 together form the substrate binding site, which is in the center of the membrane and coincides with the symmetry axis. It is worth

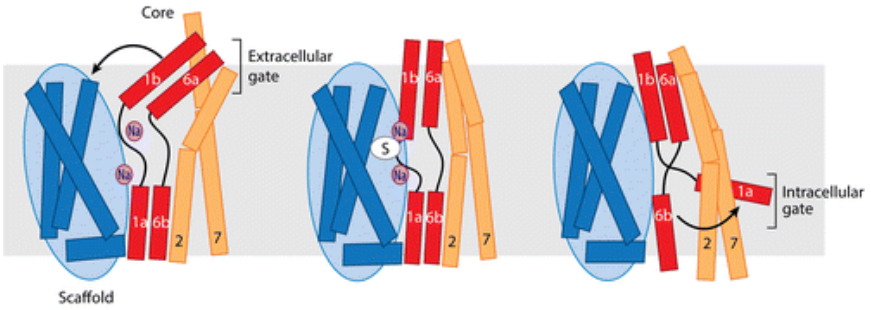

Figure 1.11: *The implementation of the "rocking bundle" mechanism in LeuT as a cartoon representation. The figure illustrates the movement of the core domain helices in a transport cycle [2, 133].*

noting that the themes of a two-fold symmetry axis and partially unwound helices is also found in transporters of different folds; It is the specific arrangement of these motifs that defines the LeuT fold. The 2005 structure of LeuT captured the transporter in an occluded state, which alone is not sufficient to define a mechanism for substrate transport. Before the structure of LeuT was solved in different conformations, a number of related protein structures appeared that showed transporters adopting the LeuT fold in different conformational states [125–131]. All these structures helped to shape the understanding of substrate translocation. Still, it was crucial that for LeuT a new set of structures was published in 2012 that contained the important inward and outward facing states, required to get a complete transport cycle [132]. Fig. 1.11 shows the three states in the LeuT rocking-bundle transport cycle in a cartoon representation. Of the two structurally distinct domains that are found in proteins with the rocking-bundle mechanism, the fix domain, which is called the scaffold-domain is depicted as a

single entity. The helices of the flexible domain, which is called the core domain, are represented as tubes. Of course, this cartoon depicts only a very schematic representation of the mechanism, but it illustrates the common underlying principle of transport following the rocking bundle mechanism. It should be noted that, even though LeuT fold transporters share similarities in their overall mechanism, there is considerable variation in how they work in detail. This is not surprising considering the high variability of substrates (and also co-substrates) that is found among proteins sharing the LeuT fold.

1.6 The SLC11 family of proton coupled metal ion transporters

1.6.1 The human transporters SLC11A1 and SLC11A2

The SLC11 family has two human representatives: SLC11A1 and SLC11A2. Before the SLC nomenclature took over, SLC11 was better known as the Natural Resistance Associated Macrophage Protein (NRAMP) family, because its original member (NRAMP1/SLC11A1) is expressed in macrophages and has an important role in defending against microbial invasions. The second member (NRAMP2/SLC11A2) is expressed in the duodenum and is responsible for the uptake of Fe^{2+} and other divalent metal ions. Hence this protein is often referred to as DMT1 or DCT1, which is short for Divalent Metal/Cation Transporter 1. Both proteins are recognised to be pro-

ton coupled transporters but whereas it is undisputed that SLC11A2 is a proton/Me^{2+}-symporter it is still not fully clear whether SLC11A1 is a symor antiporter [134]. Determining the directionality of the proton flow is important to answer the question about the strategy involved to kill bacteria. In macrophages SLC11A1 is expressed in the phagosomal membranes, that

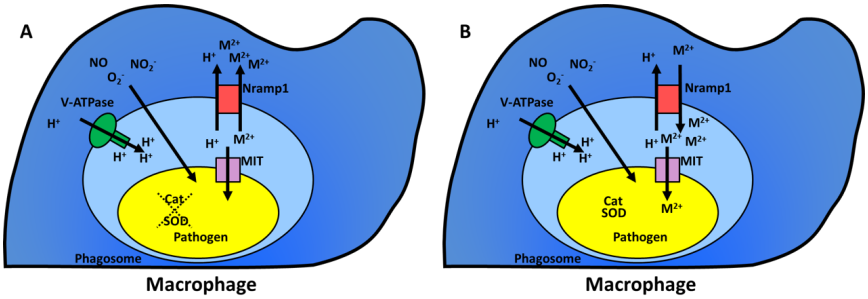

Figure 1.12: *Illustration of the two hypothesises concerning the working mechanism of NRAMP1. A: NRAMP1 acts as a symporter. Metal ions are transported out of the phagosome to prohibit pathogens to use them in their defense system (SOD) against ROS. B: NRAMP1 acts as an antiporter. Metals are transported into the phagosome where they catalyse the generation of ROS by Fenton-like chemistry (figure adapted from [135]).*

have an acidic lumen inside. Researchers in favour for SLC11A1 as a symporter argue that the function of the transporter is to transport metal ions out of the phagosome to starve bacteria from essential transition metal ions [136–138]. In particular this would make the bacteria susceptible to reactive oxygen species (ROS) because enzymes like superoxide dismutase (SOD) that protect the bacteria against ROS, use transition metal ions in their active centre. Some scientists, however, would argue that SLC11A1 is an antiporter, transporting transition metal ions into the phagosome [139, 140]. In that case the metal ions could catalyse reactions of Fenton-like chemistry

(eq. 1.6) that yields the particularly reactive and damaging hydroxyl radical.

$$Fe^{2+} + H_2O_2 \longrightarrow Fe^{3+} + OH^{\cdot} + OH^{-} \tag{1.6}$$

Compared to SLC11A1, characterisation is further advanced for the duodenal transporter SLC11A2. It has been identified that Fe^{2+} is the preferred physiological substrate, although selectivity has been ranked even higher for the toxic Cd^{2+} ions [141]. Co^{2+} and Mn^{2+} compete with Fe^{2+} uptake and are reasonably good substrates whereas Zn^{2+}, Ni^{2+} and VO^{2+} are considered to be weak substrates. No transport activity has been shown for earth alkali metal- or other ions including Cr^{2+}, Cr^{3+}, Cu^{+}, Cu^{2+}, Fe^{3+}, Ga^{3+}, Hg^{2+} and VO^{+} [141].

The situation gets more complicated when it comes to co-transport in SLC11A2. The unusual part of symport in the duodenal transporter is that the ratio of metal ion to proton transported is not fix, but varies depending on external conditions. This was already established in the first publication on SLC11A2, where it was found that at low pH a higher number of protons per turnover was transported than at high pH [142]. In a later publication [143] the findings of the first paper was confirmed and the authors proposed a model according to which SLC11A2 can adopt at least eight different states and although it acts primarily as a H^{+}/Me^{2+} symporter, under certain conditions it will operate as a H^{+}- or Me^{2+} uniporter

(fig. 1.13). Proton co-transport will be discussed in chapter 6.

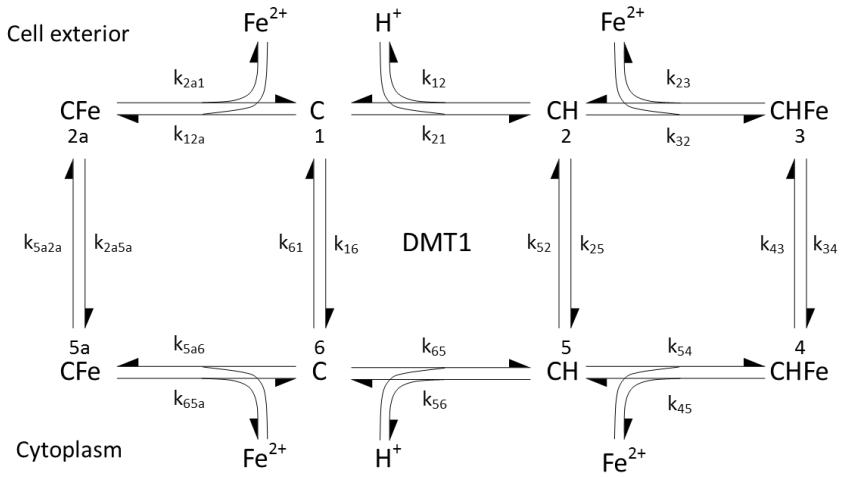

Figure 1.13: *Proposed states of DMT1 related to substrate transport. Each reaction step x →y is described by its rate constant k_{xy}. According to this DMT1 acts mainly as a H^+ coupled Fe^{2+} transporter (step 3 → 4), but under some conditions may work as well as a H^+ leak (step 2 → 5) or Fe^{2+} uniporter (step 2a → 5a) [143].*

1.6.2 Structural aspects of SLC11 transporters

This paragraph will focus on the two structures of bacterial SLC11 homologues that have been solved recently by X-ray crystallography. The first structure was of *Staphylococcus capitis* DMT (ScaDMT) [122]. The structure revealed a LeuT fold which is likely to be shared among SLC11 family members (fig. 1.14A). Of particular interest are the residues of the binding pocket which were identified to be an alanine (backbone oxygen), an asparagine, an aspartate and a methionine (fig.1.14B). As expected for the LeuT fold, these residues are located in the unwound part of TM1 and TM6 and are highly conserved among the family. Maybe the most unusual contribution comes from the methionine that coordinates the metal via its sulfur

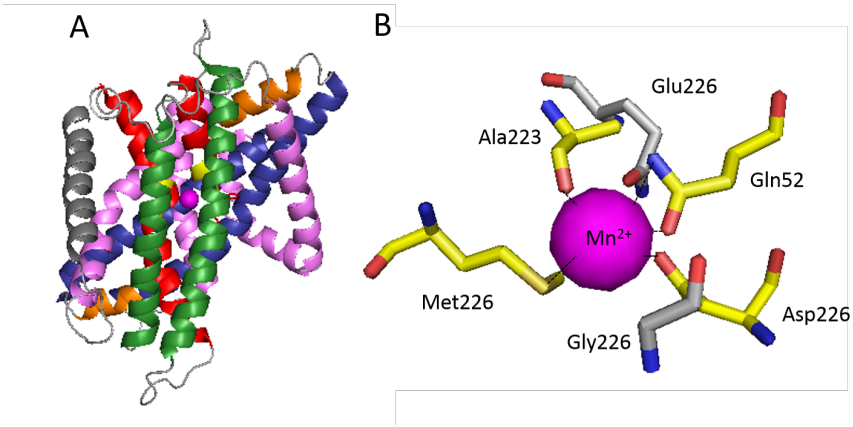

Figure 1.14: *A: Structure of ScaDMT in a cartoon representation. The colours of the helices are equivalent to fig. 1.10. The bound Mn^{2+} is represented as a sphere (mangenta). B: Residues involved in the substrate binding pocket of ScaDMT. The four residues identified in the crystal structure are shown in yellow. Grey residues have been suggested to contribute as well to substrate binding in computer simulation. Atoms of oxygen (red), nitrogen (blue) and sulfur (dark-yellow) have their separate colour. Figure made with PyMOL [6]*

atom. It was later demonstrated that the methionine plays a key role for the protein to distinguish between transition metal and earth alkali metal ions [144]. The thiol-ligand is not a good binding partner for the hard earth alkali metal ions. In MntH from *Deinococcus radiodurans* substituting methionine by an alanine led to a mutant which remained fully functional, but in addition to transition metals, the mutant would transport calcium and magnesium ions.

Crystals of ScaDMT have been obtained in the apo-form as well as bound to a series of different transition metal ions. These structures showed that Mn^{2+}, Fe^{2+}, Co^{2+}, Ni^{2+}, Cd^{2+} and Pb^{2+} occupy the same binding site. Cu^{2+} does so too but in a slightly shifted position. Of the transition metal ions, only Zn^{2+} prefers to occupy a different location, coordinating to a con-

served histidine that may have a role in proton cotransport [123, 143, 145]. Some earth-alkali metals did bind to the protein as well, but in different locations and with low affinity. Binding of these ions did not interfere with protein activity. In terms of activity, substrate transport in ScaDMT could be confirmed for Mn^{2+}, Cd^{2+}, Co^{2+} and Ni^{2+} in transport assays using the metal sensitive dye calcein. With this assay it could not be unambiguously determined whether Zn^{2+}, which does not occupy the main binding pocket, is a substrate or an inhibitor of the transporter. The assay was also incompatible for the ions Fe^{2+} and Cu^{2+}.

The second structure of a SLC11 transporter homologue, was from the *Eremococcus coleocola* protein EcoDMT and appeared very recently in 2017 [123]. Whereas ScaDMT was crystallised in an inward-facing conformation, EcoDMT showed an outward facing conformation. This second publication contained considerable work on functional studies showing proton cotransport. This will be discussed more closely when compared to functional data from MntH2 obtained in this thesis. The authors also tried to establish a transport mechanism based on their two structures and using analogies with LeuT. Nevertheless many details remain obscure. As the authors admit, for instance, it is unclear, if the mechanism is proton coupled, how proton binding to the outward open state would help substrate binding or *vice versa*.

1.7 The MntH-family and *Enterococcus faecalis* MntH2

Bacterial homologues of the SLC11 family are generally named MntH which is to suggest that these proteins are $\mathbf{H}^+$-coupled **m**a**n**ganese **t**ransporters [146]. Evidently, the nomenclature is not fully consistent, which is why the SLC11 homologues of which the structure has been solved, are named differently. MntH proteins form one of the two major protein families responsible for Mn^{2+} uptake in bacteria. The other one consists of the Mn^{2+} specific ABC-transporters named MntABC(D) [147, 148]. Manganese is an essential transition metal and required for a number of important enzymes. These include most famously superoxide dismutase (SOD), but there are many more processes where Mn^{2+} plays a key role, including glycolysis [149]. Therefore, bacteria have to rely a great deal on their Mn^{2+} import machinery. This is especially the case when bacteria are invading host tissue, because Mn^{2+} concentrations are very low in this environment due to the cellular defense of the host, that includes scavenging of Mn^{2+} and other ions by a histidine rich protein called calprotectin [150]. To be able to compete with calprotectin, bacterial uptake proteins have to be very efficient and operate with a K_M in the order between 100 nM and a few μM [149]. A single strain of bacteria may express more than one SLC11 homologue. In *Enterococcus faecalis* there are three SLC11 homologues expressed, which after an elabo-

rate nomenclature are labelled EfcmCβ, EfaCβ1 and EfaCβ2 [151]. EfaCβ1 is the protein investigated in this thesis, but instead it will be referred to as MntH2, following the nomenclature of a different publication [152]. The mentioned publications on MntH2 included some *in vivo* characterisation of the protein: Richer et al. [151], in an assay measuring metal-induced growth inhibition, found that MntH2 overexpression in *E. coli* leads to enhanced sensitivity towards Cd^{2+}, Co^{2+} and Fe^{2+}. No change in the growth was found when the bacteria were subjected to excess Mn^{2+}. A number of studies have performed expression analyses in response to metal replete or deplete conditions. From this work it is known that MntH2 expression in *Enterococcus faecalis* is downregulated in the presence of Mn^{2+} and Cu^{2+} and upregulated by excess Zn^{2+} or Fe^{2+} [152]. A further study reported downregulation in the presence of Fe^{3+} [153].

An overexpressing construct of MntH2, as well as a purification protocol has been established in a thesis precedent to this one [108] and been subject to a publication [154]. The construct is shown in fig. 1.15 as a topology diagram. It includes the full length protein bearing a His_8-tag at the C-terminus that is precluded by a HRV cleavage side. To predict the topology of the residues, the crystal structure of ScaDMT has been used as a template. Besides an overexpressing construct, the aforementioned publication included as well some functional data from *in vitro* experiments using the stopped flow fluorescence technique, which show Zn^{2+} transport in MntH2.

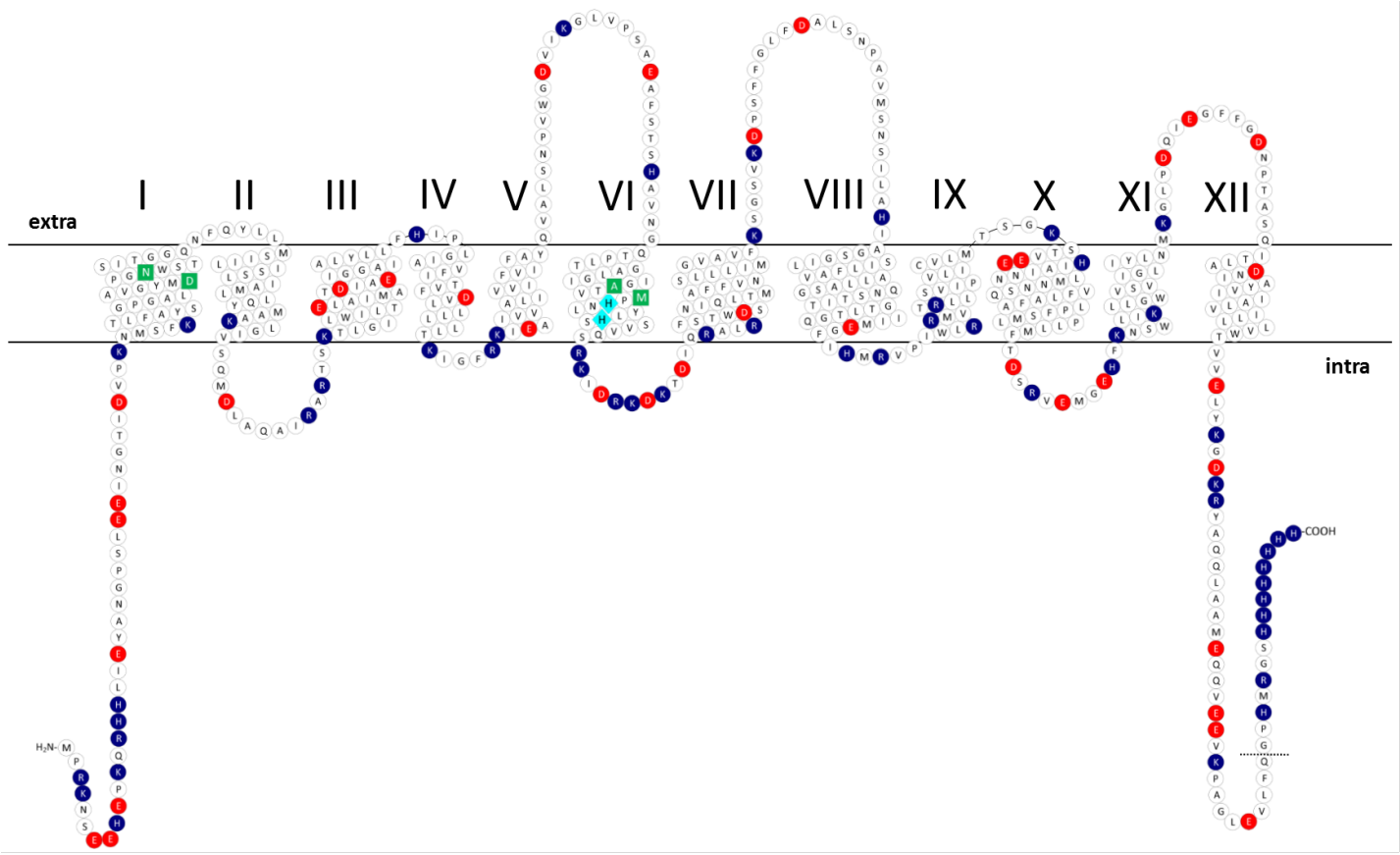

Figure 1.15: *Topology diagram of MntH2. The model is based on the crystal structure of ScaDMT, and secondary structure elements were assigned accordingly. Red/blue: negatively/positively charged residues, green: residues involved in substrate binding, cyan: residues potentially involved in proton coupling. The dotted line indicates the HRV-3C cleavage site.*

However, Mn^{2+} transport was failed to be detected in similar experiments [108]. In this project MntH2 served as a model protein to test the applicability of solid supported membrane based electrophysiology towards transition metal transport. Details about why this technique was chosen and its advantages over fluorescence based and other membrane transport measuring techniques are discussed in the following chapter.

In summary this project consisted of two parts, for which the main research question was addressed with solid supported membrane based electrophysiology. In case of TRPM2 a major goal was to provide direct evidence that TRPM2 is able to conduct Zn^{2+} to confirm its proposed role in apoptosis [106]. Another goal was to identify direct and indirect activators among natural and synthetic ligands.

The main question connected to MntH2, initially was to confirm that the protein is a Mn^{2+} transporter. Later it was attempted to obtain a complete biophysical characterisation of MntH2. This included determining all substrates/inhibitors and co-substrates.

Chapter 2

Methods for measuring membrane transport

This chapter will introduce the most important techniques to assay membrane transport. The largest part of this chapter will be dedicated to solid supported membrane based electrophysiology, which is the technique that has been predominantly used in this thesis. For comparison, an introduction of the patch-clamp method is given, even though this technique has not been applied in this thesis. At the end of this chapter some non-electrophysiological methods to measure substrate uptake of membrane transporters are briefly discussed as well.

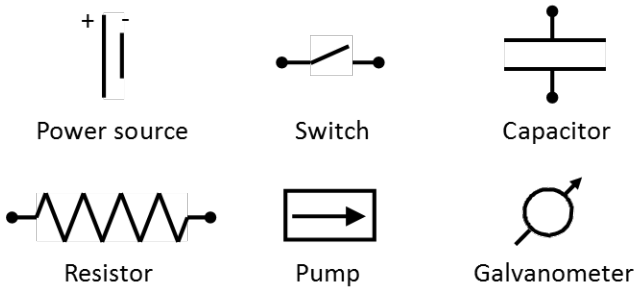

Figure 2.1: *Schematic representations of selected circuit elements and components.*

2.1 Electrical circuits

An electrical circuit is a closed loop of a conducting element which allows current to circulate when driven by a power source [155]. A very simple electrical circuit consists only of a voltage source and a resistor in a circular connection. Electrical circuits are an abstract way to describe the flow of currents in a real system. They are built by a combination of basic circuit elements with well defined electrophysical properties. Three basic circuit elements are, for instance, resistor, capacitor and inductor, whereby only the first two of these elements will be introduced here. Fig.2.1 gives an overview of all the circuit elements and other circuit components that occur in this thesis. The simplest circuit element is the resistor. Its characteristics are described by eq. 2.1.

$$U = R * I \tag{2.1}$$

Equation 2.1 is called Ohm's law. Ohm's law states that the current, I, passing a resistor is proportional to the applied voltage, U. The proportionality

constant R is called the resistance and has the unit ohm (Ω). It is defined by a resistor's ability to oppose a current to pass through it. The resistance depends on the material the resistor is made of and on its geometrical properties (eq. 2.2).

$$R = \rho \frac{l}{A} \tag{2.2}$$

In eq. 2.2 ρ is the electrical resistivity that is a material specific constant. The variables l and A stand for the length and the area respectively. The inverse of the resistance 1/R is called the conductance. It is usually assigned with the symbol "G" and it is measured in siemens (S).

Another important circuit building block is the capacitor. It consists of two conducting surfaces in close proximity, separated by a non-conducting medium. Its most common form is the plate capacitor where two parallel plates of a conductor enclose a non-conducting medium. Other geometrical forms of capacitors exist as well but will not be discussed here. When a voltage is applied to a capacitor charges of opposite sign are built up on the capacitors surfaces. The amount of charge in the capacitor is linearly related to the applied voltage:

$$Q = C * V \tag{2.3}$$

The constant C is called the capacitance. It has the unit Farad (F) where one Farad is equal to one coulomb per volt. A capacitor's capacitance is

dependent on the material/substance and the thickness of the medium layer in between the two conductors. It is given by the following equation

$$C = \frac{\epsilon_0 \epsilon_r A}{d} \tag{2.4}$$

where A is the area of the capacitor, d is the distance in between, ϵ_0 is the permittivity of free space and ϵ_r is the relative permittivity of the medium. ϵ_r is also named dielectricity constant. This constant describes the mediums ability to polarize in response to an electric field. Molecules with a permanent dipole, like water, are highly polarisable because the dipoles will align with an applied electric field, in antiparallel fashion, such that the electric field of the dipole points into the opposite direction of the original field. This means that in a capacitor with a polarisable medium the influence of the charges from one plate to the other is diminished which allows the capacitor to accumulate more charge. Consequently, if the medium is apolar less charge will be built up.

The remaining circuit elements depicted in fig. 2.1 shall be explained briefly. A power source is an element that provides either a voltage or a current to energize the circuit. A typical would be a battery, for instance.

A pump is in principal similar to a power source. The difference is that the power source has a constant output that is not affected by the circuit, whereas the performance of the pump is dependent on the electrical pro-

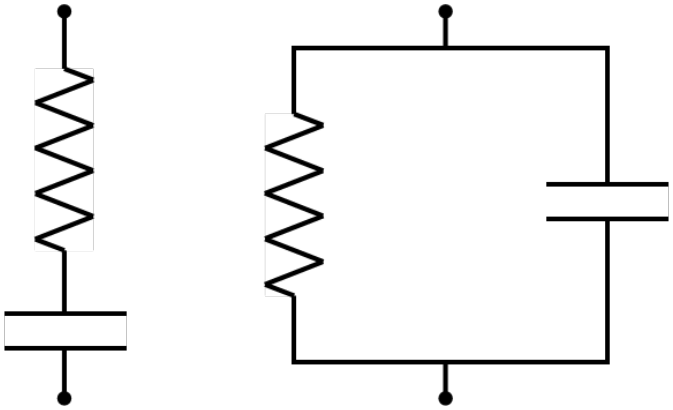

Figure 2.2: *A capacitor and resistor connected in series (left) and in parallel (right).*

cesses that happen in the circuit. In this thesis, the pump will be used to represent a membrane protein.

The switch provides control over the electrical energy flow of the circuit. A closed switch allows the energy flow to continue and an open switch breaks it. Finally, the galvanometer is a device to measure current.

2.1.1 Series and parallel circuits

In an electrical circuit, elements can be either connected to each other in series or in parallel (fig. 2.2). The following relations can easily be derived when considering that a given circuit element can be conceptually split up into two halves. Depending on how the element is split, the two halves can then be recombined in parallel or in series to yield back the original element. For instance, splitting a resistor perpendicular to its axis will yield two elements that in series must have the same resistance as the original element according to eq. 2.2. Likewise, when the same resistor is cut along its axis, the resulting elements in parallel are equivalent to the resistor as a

whole. Analogous considerations can be made for capacitors.

It will be found that for resistors in series the following relation holds:

$$R_{tot} = R_1 + R_2 + ... \tag{2.5}$$

and in parallel:

$$\frac{1}{R_{tot}} = \frac{1}{R_1} + \frac{1}{R_2} + ... \tag{2.6}$$

For capacitors the relationships are analogous but are switched around for in series and parallel circuits. The total capacitance of multiple capacitors in parallel is the sum of the individual capacitances:

$$C_{tot} = C_1 + C_2 + ... \tag{2.7}$$

and the relationship for capacitors in series is reciprocal:

$$\frac{1}{C_{tot}} = \frac{1}{C_1} + \frac{1}{C_2} + ... \tag{2.8}$$

2.1.2 Equivalent circuits

In practice the relations from section 2.1.1 can be used to simplify electrical circuits representing a complex system. This includes essentially any system in the real world that is not made entirely of electrical components. As an example could serve for instance a cell membrane. The electrical properties of a cell membrane are generally represented by a capacitor and a resistor

in parallel. An exact representation would be much more complex: The capacitance of the membrane will vary slightly with the exact spot on the cell surface due to inhomogeneities in lipid composition and the presence of membrane proteins. In a completely accurate description this would be accounted for by a huge number of capacitors and resistors in parallel. Such a representation would obviously be very impractical and therefore a simplified circuit is used that reflects the systems properties sufficiently accurate. Such circuit is then referred to as an equivalent circuit.

2.1.3 Kirchhoff's circuit laws

When dealing with electrical circuits it is very useful to know two basic laws that are valid in any given circuit. They are called Kirchhoff's laws after the German physicist Gustav Kirchhoff who described them first in 1845. Kirchhoff's first law is also called Kirchhoff's current law (KCL). It states that at any node or junction in an electrical circuit the sum of currents flowing in and out of that node is zero (eq. 2.9).

$$\sum_{k=1}^{n} I_k = 0 \tag{2.9}$$

In eq. 2.9, n is the total number of branches with currents flowing in or out of a node and currents flowing out are signed negatively. This law intuitively makes sense because the sum of currents flowing into the node has to be the same as the sum of currents flowing out.

Kirchhoff's second law is referred to as Kirchhoff's voltage law (KVL). It states that the (directed) sum of any electrical potential differences around any closed loop is zero (eq. 2.10).

$$\sum_{k=1}^{n} V_k = 0 \tag{2.10}$$

In this case n is the number of circuit elements in the loop across which a potential difference is measured. This rule also is very intuitive. When making a full turn around a loop one has to arrive at the same potential as one has started with. Otherwise it would violate the law of energy conservation.

2.1.4 Capacitive coupling

Capacitive coupling is a term that will be of importance when discussing the SURFE^{2}R technique and is introduced here, because it is a phenomenon that can be easily explained by using the basic electrophysics from previous sections. First, it has to be clarified, that the term "capacitive coupling", when used in a different context from this thesis, can have a slightly different meaning. More commonly, capacitive coupling describes the interaction between two electrical circuits, mediated by a capacitor. This is often unwanted as it can be a source of noise. For instance when two conducting wires come close to each other, they form a capacitor, which can then lead to communication between the wires, distracting their signals.

Here, "capacitive coupling" is used to describe the behaviour of an electrical

circuit with two capacitors in series. It merely states that in such a circuit, if the first capacitor experiences a change in voltage, the voltage across the second capacitor has to alter simultaneously, for the circuit to obey the KVL. An illustration of this is given in fig. 2.3 , which shows the process in four panels (A-D). For ideal capacitive coupling the circuit consists of basically two capacitors in series (fig. 2.3A). The first capacitor has a pump in parallel, that can transport charges against a potential gradient, when it is switched on. For simplicity it is assumed that both capacitors have the same capacitance (C1=C2). In the initial state, the pump is switched off, no charges are moving and there is no potential difference across the capacitors (V1=V2=0). At some point the pump will be switched on for a short time, Δt, during which it will transport the charge ΔQ (fig. 2.3B). This creates a charge imbalance on the first capacitor. It can be noted that fig. 2.3B represents a physically impossible state as Kirchhoff's voltage law is violated. In reality, when the first capacitor is charged, the second capacitor will charge in an immediate response so that V1 is equal to -V2 at all times. This is illustrated in fig. 2.3C: Half of the charge transported by the pump (ΔQ/2) is passed on to the second capacitor which equivalently passes ΔQ/2 through the external circuit. In this way both capacitors will end up carrying the same charge (fig. 2.3D). Note that this is only true because in this example the capacitances are equal. The distribution of the charges depends on how the capacitances of the two capacitors relate to each other.

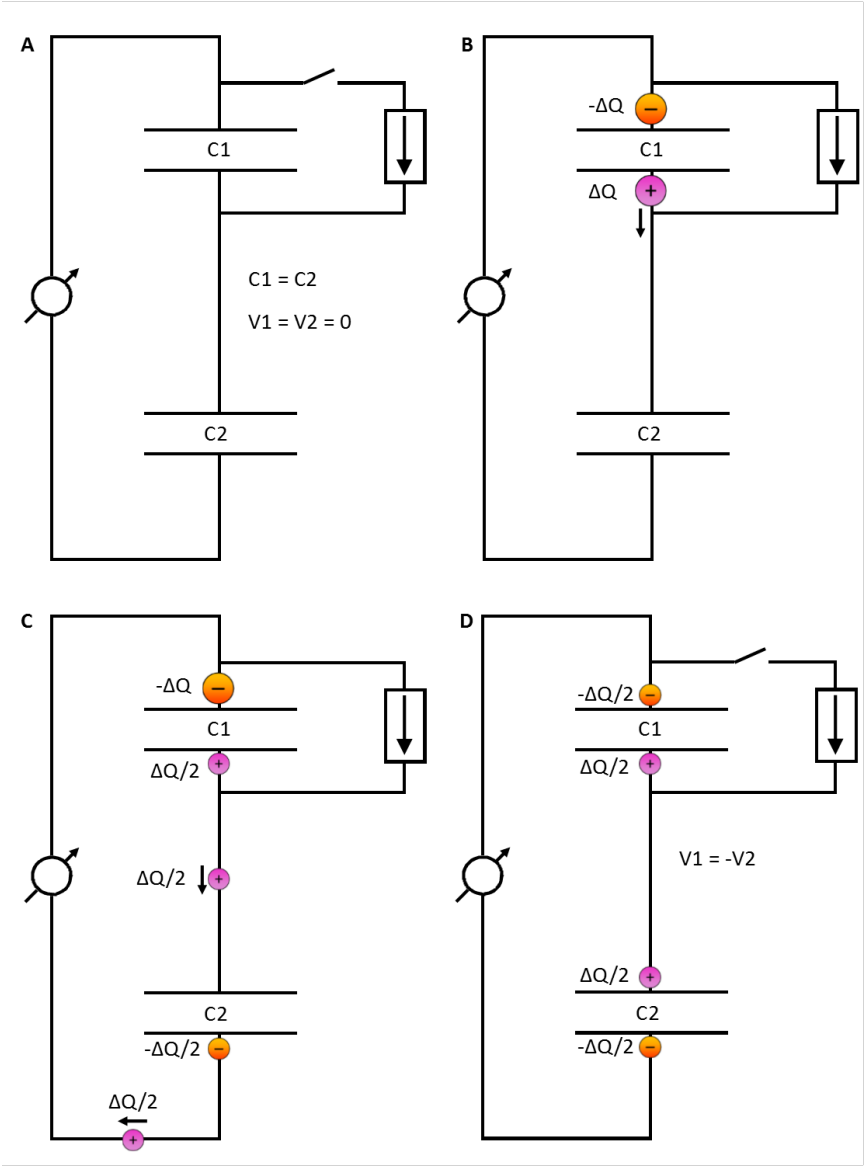

Figure 2.3: *Schematic illustration of charge movements in the event of ideal capacitive coupling. A: A requirement for ideal capacitive coupling is a circuit with two ideal capacitors in series. One of the capacitors can be charged by a pump that is connected in parallel to the capacitor. B: When the pump is switched on for a time Δt it will transport a charge ΔQ which leads to charging of the first capacitor. C: This will lead to an immediate response in the second capacitor because according to Kirchhoff's voltage law both capacitors must experience the same potential difference at all times. For this reason, given that in this example C1 = C2, a total charge $\Delta Q/2$ is passed through the external circuit, that will recombine with the negative charge on the first capacitor. The resulting current is registered by the galvanometer. C: The pump has switched off and both capacitors end up carrying the same charge.*

A mathematical expression for this is given in eq. 2.15 (section 2.4) where the signal detection with the SURFE^{2}R technique will be discussed.

2.2 Electrophysiology

Electrophysiology is a field in biology that studies the processes in living systems that in some way cause a charge imbalance in the system and therefore can be recorded as a current. The field dates back to as early as the late 18^{th} century when Luigi Aloisio Galvani observed that frog muscles contract when he applied an electric shock to one of its nerves [156]. From this discovery researchers began to understand that nerve signals are of electrical nature. One and a half centuries later, during which techniques and experiments have steadily developed, the American biophysicists Cole and Curtis could already measure a complete action potential of a giant squid [157]. But although this was a milestone, to understand signal transmission on a molecular level further technological advance had to be made: At this time there was no technique available that was sensitive enough to measure the currents of single ion channels that promote the progression of the action potential and hence at this point there was no evidence even that these ion channels even existed. The breakthrough was made in the late 1970's with the development of the "patch clamp" technique by Erwin Neher and Bert Sakman that enabled the recording of single ion channel currents [158]. For their achievement Neher and Sakman got awarded the Nobel Prize in 1991. After it was understood how electrical signals are transmitted in neurons,

the field of electrophysiology advanced to investigate function and mechanism of electrophysiologically active ion channels and transporters in detail. "Patch clamp" is by far the most common technique to address these questions and the basics of the technique will be introduced in the following paragraph. The technique applied in this project, solid-supported membrane based electrophysiology, is less commonly used but it is very useful for certain purpose. A thorough introduction of this technique will be given in section 2.4 that, along with explaining the working principle of this technique, will discuss some aspects of its development and highlight the key aspects where it performs better than "patch clamp".

2.3 Patch clamp technique

In the patch clamp technique a micropipette is pressed against a single cell and by applying suction a very tight junction is formed between cell membrane and pipette that has a gigaohm resistance (fig. 2.4). In patch clamp terminology this is called a gigaseal. The high resistivity of the gigaseal allows for the detection of single ion channel currents across the membrane patch spanning the pipette. The measured current is the sum of two components: The ions flowing through the ion channels and the capacitive current. The capacitive current results from ions of one kind adsorbing to one side of the membrane, attracting ions of the opposite charge to the other side of

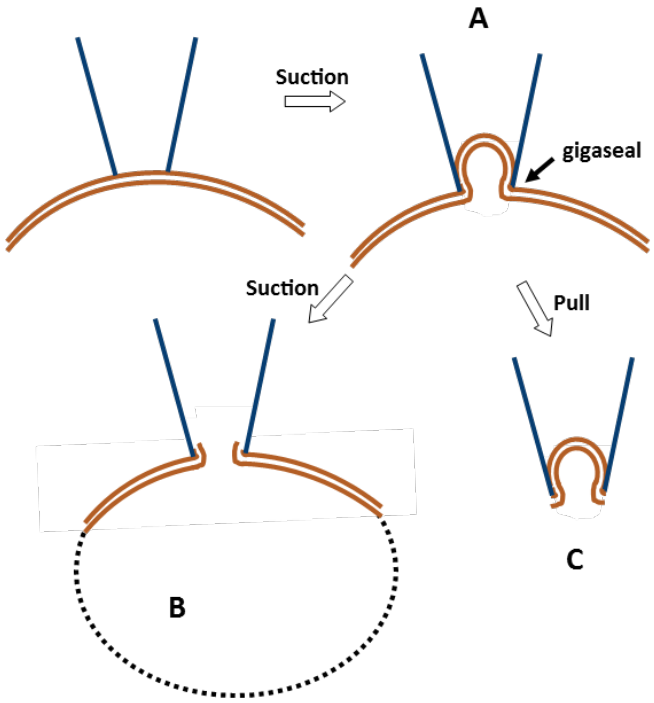

Figure 2.4: *Illustration of the patch-clamp technique. In a first step suction is applied with a micropipette to the membrane of a single cell to yield the initial configuration (A). In this step the gigaseal is formed. From the initial configuration different configurations can be reached including (B): Whole-cell configuration and (C): Inside-out configuration.*

the membrane. This can be summed up in the following equation [159]:

$$I_m = I_{ionic} + C_m dV/dt \tag{2.11}$$

I_m is assigned for the total current, I_{ionic} for the current gated through the ion channel and C_m is the membrane capacitance. To diminish the contribution of the second term of equation 2.11, voltage clamp experiments are usually performed where the membrane voltage is fixed [159]. In voltage clamp experiments the current is then recorded as a function of the mem-

brane potential. Other experimental parameters that need to be varied in patch clamp experiments include the concentration of extra- and intracellular ion concentrations. However, in the conformation described above, this is not possible because the solutions on neither side of the patch (cytoplasm and pipette solution) can be easily exchanged. Therefore the initial conformation is of limited practical use in terms of conducting experiments. There are several ways to adapt the experiment to enable exchange of extra- and intracellular solutions. Two conformations will be described here: The "whole cell" and the "inside-out" conformation. Details about other patch clamp conformations have been excellently reviewed elsewhere [159, 160].

Whole cell configuration

The whole cell configuration is the most common set up for patch clamp experiments. It can be achieved from the initial configuration by briefly applying a higher suction that will remove the membrane patch at the end of the pipette so that the interior of pipette and cell are connected (fig. 2.4). In this configuration transport from all ion channels in the cell membrane is observed and the extracellular buffer can be altered by exchanging the bath solution. An advantage of the whole-cell configuration is that cytosolic components are retained, which can be essential for activation of the channel. At the same time the presence of cytosolic components can be a drawback when the experimental goal is to determine direct activators of the channel.

Compounds that are added to the extracellular buffer might start a signal cascade that can set free effectors of the target protein contained within the cell. In this way a molecule might be identified as a modulator of a protein even though it affects its state of transport only indirectly. This can make an accurate biophysical characterisation very challenging and this is especially a problem for drug discovery. Another drawback of the whole cell configuration is that modulators that bind intracellularly will not be identified in experiments if they are not membrane permeable. A different patch-clamp configuration, that is applied to avoid these downsides, is the inside-out configuration. It will be introduced here shortly because it has been applied in relevant research studies on the TRPM2 channel [100, 104].

Inside-out configuration

The inside-out configuration can be reached from the initial configuration by abruptly pulling the pipette away from the cell to which the pipette is attached (fig. 2.4). As a result the membrane patch will rupture from the cell and the cytoplasmic side of the patch will face the bath solution. In this configuration, the cytosolic components are removed from the system so they do not contribute to the experiment. The disadvantage of this configuration is that it is further away from a native like environment than the whole cell configuration as intracellular components might be required to assist modulation of the protein.

To conclude the introduction of the patch clamp technique some practical aspects should be discussed: The patch clamp technique is very challenging to perform and it requires a researcher several months of training to learn. To achieve the formation of a gigaseal, exact protocols for the preparation of the cells and the pipettes have to be followed. For this reason traditional patch clamp is a very low throughput technique. A lot of research effort has been undertaken to increase the throughput of the patch clamp technique. Nowadays there are different systems of patch clamp robots available that can automate some of the tasks. But even though these systems are very useful for drug screens, automated patch clamp is still less flexible compared to manual patch clamp in terms of experimental design, quality of data and types of cells investigated [161]. A detailed discussion of the possibilities and limitations of automatic patch clamp would go beyond the scope of this section. However, with respect of the work performed in this thesis, it is noteworthy that among other families, TRP channels turned out to be challenging to investigate by automated patch clamp [161, 162].

2.4 Solid supported membrane based electrophysiology

2.4.1 Introduction

Solid supported membrane based electrophysiology is a technique that has been developed in the 1990's by Fendler and co-workers [163, 164]. It has been commercialised and is currently marketed by NaNion technologies as an instrument called SURFE^{2}R (SURFace Electrogenic Event Reader). It was designed with the main purpose to study membrane transport proteins and measure their activity with a high time resolution ($\geqslant$5 ms). A high time resolution is needed to measure pre-steady state currents of transporters, that contain information about different steps in their reaction cycle [163]. Fig. 2.5 shows a schematic representation of the chip's surface that forms the basic of the technique: Preparations are adsorbed onto a modified gold surface in a sensor chip. These preparations can either be proteoliposomes or membrane extracts from overexpressing cells/bacteria. The modification on the gold surface consists of a layer of 1-octadecantethiol (1-ODT) completed with a layer of a specific lipid (DPhPC) to form a so called "hybrid bilayer". This hybrid bilayer provides a surface with a very low capacitance, which is a requirement to keep noise levels low during experiments. The sensor is mounted in a fluidic system that allows for a rapid exchange of the external buffer. At the beginning of the experiment this buffer will be

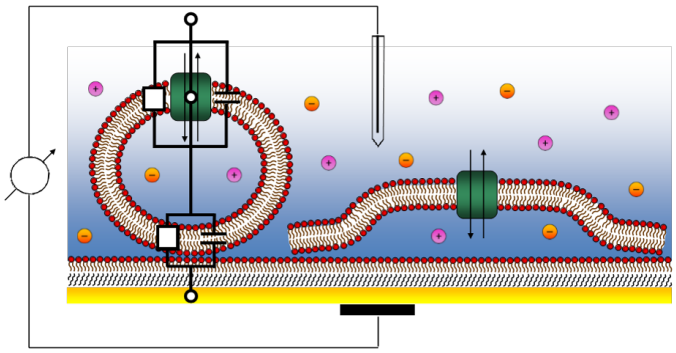

Figure 2.5: *Experimental setup of the SURFE^{2}R technique. Protein is added in membrane fragments (proteoliposomes, membrane extracts), which are adsorbed to a chemically modified gold sensor. The sensor is mounted in a fluidic system and when substrate is added by exchanging the external buffer, the protein is activated. Currents resulting from protein activity will be registered in the external circuit by capacitive coupling. In the left part of the figure the equivalent circuit of the system is illustrated.*

neutral towards the target protein (typically a transporter; see next paragraph in case the protein is an ion channel) and is called "non-activating buffer". This means that the protein will be inactive. When the external buffer is exchanged by a buffer containing a substrate ("activating buffer"), the protein will be activated because the substrate gradient between the internal and the external buffer will drive uptake of the substrate. In case transport is electrogenic this will lead to a response in the external circuit due to the effect of capacitive coupling as described in section 2.1.4. It is worth noting that not only transport of a charged substrate, but any process that is electrogenic, will be recorded. This includes binding of a substrate to its binding pocket [165] or a conformational change in the protein that leads to rearrangement of some charged domains [166].

The protocol described above includes only one solution exchange and works

only if the target protein is a transporter. SSM-based electrophysiology works also for (ligand/signal gated) ion channels [167] but the workflow has to be adjusted. Instead of one solution exchange, the protocol for ion channel includes two solution exchanges and a third buffer, which is called the "resting buffer". In the first solution exchange an ion gradient is established by exchanging the "resting-buffer" with "non-activating" buffer, which has a different ion composition. This ion gradient is needed to drive ion flow through an open channel. The channel is then activated by exchanging "non-activating buffer" with "activating buffer" as described for transporters above.

2.4.2 Development and theory of SSM-based electrophysiology

To get a better understanding of SSM based electrophysiology and its benefits, an outline of the context in which the technique was developed will be given.

Before solid supported membrane based electrophysiology was developed, studies were performed with free standing bilayers called black lipid membranes (BLMs). A BLM is a lipid bilayer membrane is "painted" over a small aperture (< 200 μm diameter) in a teflon membrane that separates two aqueous chambers (fig. 2.6). In each of the chambers an electrode is placed so that by linking the electrodes over an external circuit, potential changes and charge flow between the two chambers can be detected. The

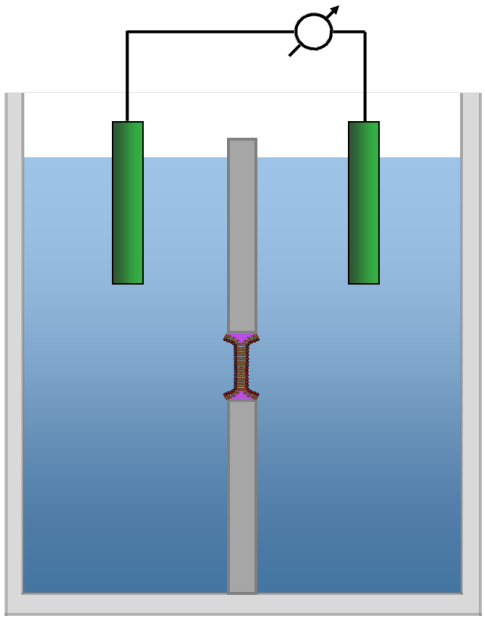

Figure 2.6: *Setup for a BLM experiment. The BLM separates two aqueous chambers that are connected by an external circuit. For investigation of transport proteins, membrane fragments containing the target protein are added on either side of the membrane. It has to be noted that in the BLM technique ion channels are incorporated directly into the BLM. Only when transporters are investigated on a BLM the sample is adsorbed in membrane fragments as in SSM-based electrophysiology [164].*

protocol for Membrane fragments containing the target protein are added on either side of the membrane (if the target protein is a transporter, see legend to fig. 2.6). Conceptually, transport studies on BLMs are similar as on a SSM with the only differences being of practical nature. The most definite advantage of using a SSM as opposed to a BLM is that SSMs have a much higher mechanical stability compared to BLMs which enables one to rapidly exchange the solution in the aqueous chamber by applying a rapid flow. This is of great importance in order to measure currents under the limits of ideal capacitive coupling, as will be discussed later.

The first study on transport proteins on a BLM setup was performed in 1974 by Drachev *et al.* [168]. Notably, this was before Neher and Sakmann recorded single ion channel currents for the first time in 1976 by the patch-clamp technique [169]. Drachev *et al.* intended to observe activity of the bacterial membrane transporters bacteriorhodopsin, H^+-ATPase and cytochrome oxidase by incorporating them into the BLM and then detect ion flux between the two chambers. This approach, however, failed but the authors realised that they could see currents when membrane sheets containing the protein of interest were adsorbed to one side of the BLM. Based on this observation the authors assumed that the observed currents are not due to ions crossing the BLM but that capacitively coupled currents from ion pumping into vesicles adsorbed to the BLM are detected.

At this point it is important to note that getting direct evidence of the adsorption geometry of vesicles or membrane sheets on a planar BLM membrane is challenging. Up to the present date, no images recorded from AFM or SEM have been published. Knowing the adsorption geometry is important for modeling an equivalent circuit to the system, which is required to accurately interpret the measured currents. An key paper for establishing a model circuit was published in 1979 by Bamberg *et al.* [170], who adsorbed purple membranes containing bacteriorhodopsin and activated the bacteriorhodopsin by illuminating with light. The authors observed that when the BLM was non-permeable they obtained a light-induced transient

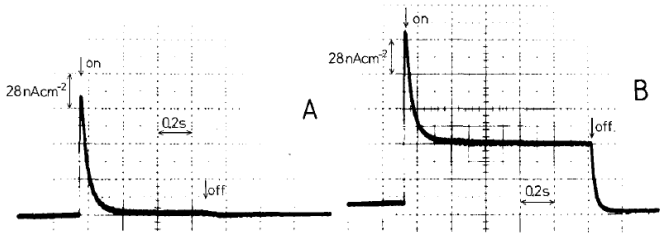

Figure 2.7: *BLM experiment with purple membranes. A: Activation by light induces a short transient current that declines when the membranes are fully charged. B: The BLM is made proton-permeable by the protonophore CCCP. In this case a continuous steady-state current is observed as the protein continues to pump protons. Together this data is evidence for an adsorbed geometry ob the purple membranes [170].*

current that rapidly declines and after ca. 250 ms returned to baseline (fig. 2.7A). When the BLM was made permeable to protons, a large stationary current remained after the initial transient current and, under constant illumination, the stationary current was stable for at least 20 min (fig. 2.7B). The interpretation of this data is that in the first case protons are transported into a compartment that builds up a positive potential inside and, as a result, transport is stopped and the current declines. When the BLM is made permeable to protons, protons can be constantly removed from the compartment to the other side of the BLM. Therefore transport is maintained and a steady current is observed. These results were strong evidence for the "adsorbed configuration" and the authors described the system by an equivalent circuit introduced by Herrmann and Rayfield in a precedent study (fig. 2.8) [171]. In this circuit the parallel elements C_m and G_m represent the capacitance and conductance of the BLM. Because of the very high resistance of a BLM G_m can assumed to be zero. Similarly C_p and G_p

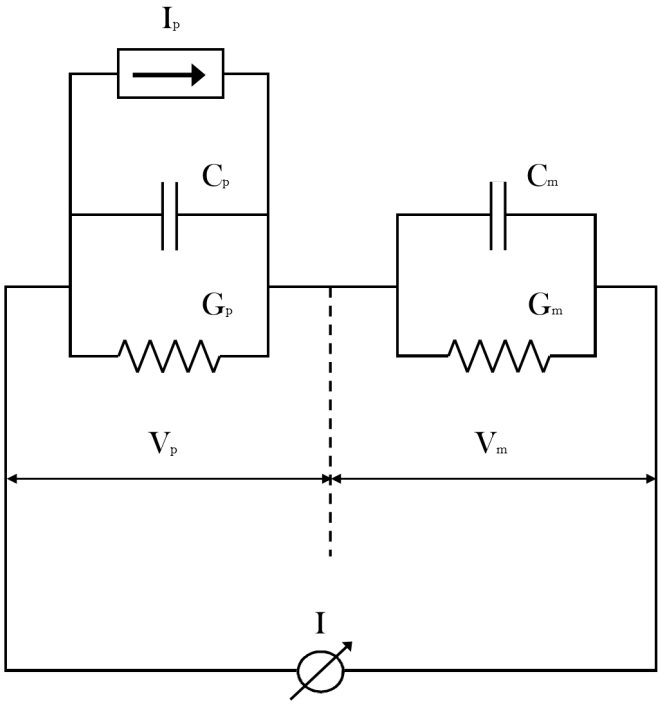

Figure 2.8: *Equivalent circuit for BLM experiments that can be used analogously for the SURFE^{2}R technique. The protein preparations are described by three elements in parallel: A capacitance C_p, a conductance G_p and a pump. The BLM is represented by a capacitance (C_m) and a conductance (G_m) in parallel, where G_m is usually approximated to be equal to zero. Short circuit conditions are assumed, which implies that V_p is equal to -V_m.*

are assigned to the capacitance and conductance of the purple membrane sheets and I_p models the current due to light induced proton pumping of bacteriorhodopsin. Note that G_m does not only represent the conductance of the purple membrane bilayer but also accounts for possible leakage at the edge of the membrane sheets that contact the BLM [170]. As mentioned, having an equivalent circuit is important for the analysis of signals. From the model circuit in fig. 2.8 it is possible to predict the signal $I_{(t)}$ that is obtained from a given pump current I_p. This will help to understand the information that is contained in the observed current. An expression for

$I_{(t)}$ can be obtained by circuit analysis, which means solving a differential equation describing the behaviour of the circuit. Such equation can be obtained for instance by using Kirchoff's first law (2.9) and summing up all the currents through the node between the membrane sheets and the BLM to zero (eq. 2.12).

$$I_p + G_p V_p + C_p \frac{dV_p}{dt} - C_m \frac{dV_m}{dt} = 0 \tag{2.12}$$

Solving this equation yields a complex expression, which has been derived in more detail elsewhere ([172]).

$$I(t) = \frac{C_m}{C_m + C_p}[I_p(t) - exp(-t/\tau_I)\frac{1}{\tau_I}\int_0^t I_p(t')exp(t'/\tau_I)dt'] \tag{2.13}$$

τ_I represents the so called "system time constant" and is given by:

$$\tau_I = \frac{C_m + C_p}{G_p} \tag{2.14}$$

Because the solution is complex, it is worth considering a hypothetical scenario in the limit $G_p \rightarrow 0$. In this scenario the circuit would reduce to the one in section 2.1.4 and hence under these conditions ideal capacitive coupling would occur. In this case the solution simplifies to:

$$I(t) = \frac{C_m}{C_m + C_p} I_p(t) \tag{2.15}$$

As would be expected under ideal capacitive coupling conditions the measured current is related to the pump current by a simple proportionality constant that is dependent only on the capacitances of the BLM and the adsorbed membranes. The complexity of the real solution is due to the fact that the adsorbed membranes do not behave as an ideal capacitor and ions will leak out through the resistance G_p during the measurement. An important point is that at short times ($t \rightarrow 0$) the leak current through G_p will not be significant because leakage is dependent on the voltage across the resistance according to ohm's law. At the start of the experiment, the pump has not had time to establish a membrane potential and therefore leakage will be negligible. This can be verified mathematically by inserting $t = 0$ into eq. 2.13. This will again yield eq. 2.15 and therefore this shows that the conditions of ideal capacitive coupling are always fulfilled at short times [172].

This is of great importance experimentally, because it means that the amplitude of the peak current is directly proportional to the pump current and therefore can be used to quantify activity of the pump. With this information, it is thus possible to characterise a transport protein, e.g. identifying its substrate and determine the K_M by plotting the amplitudes of the peak current against the substrate concentration. It shows as well the necessity of a rapid solution exchange when adding substrate, as otherwise the peak current would shift out of the range where ideal capacitive coupling applies.

Technically, planar membrane based electrophysiology can be used not only to determine the substrates of transport proteins and their corresponding K_M values, but also transport associated rate constants. The latter information is contained in the pre-steady state currents that are obtained in a concentration jump experiment: At the start of the experiment, when turnover starts, no substrate is bound to the enzyme. The enzyme will then bind the substrate and after a short equilibration period the concentration of the enzyme-substrate complex remains constant. This is when the steady-state is reached. The time it takes to reach the steady state depends on the rate constants of processes preceding the rate limiting step, which is substrate translocation. Extensive analysis of pre-steady state currents have been performed for instance on bacteriorhodopsin [173] and Na^+/K^+-ATPases [172, 174] on BLMs. Pre-steady state analysis was restricted to enzymes that could be activated either directly or indirectly with light, because of the low mechanical stability of the BLM. In case of the ATPase, "caged"-ATP was used as a substrate, that is chemically modified ATP, that forms ATP when exposed to light.

The development of SSM based electrophysiology enabled a rapid activation of transporters with arbitrary substrates and successful studies have been performed for example on sugar and amino acid transporters [166, 175]. Nevertheless, these experiments require a very high standard of equipment to provide the required time resolution. Time constants of pre-steady state

currents are usually in the order of 10-20 ms. The SURFE^{2}R N1 instrument used in this project at best has a time resolution of 20-30 ms, which is often too low for this kind of analysis.

In this final paragraph of this section, some practical aspects are discussed that highlight the potential advantages of the SSM based electrophysiology over the standard patch clamp technique, but also its downsides. A key advantage of SSM based electrophysiology is that it can be applied to systems with small internal volumes like bacteria, organelles or proteoliposomes which in most cases are impossible or, at the very least, extremely difficult to investigate with patch clamp techniques. Besides this, the technique is particularly useful for investigating transport proteins. Even though patch clamp is a perfectly suitable technique to detect activity of transporters, they can be more challenging to work with than ion channels. Because transporters have a much lower turnover compared to the ion conductivity of ion-channels, it is generally more challenging to get a decent signal-to-noise ratio. In SSM based electrophysiology, the signal is enhanced by the large number of transporters investigated at the same time. Geibel et al. have compared the performance of the two techniques and found that currents from the sodium/calcium exchanger NCX1 recorded on the SSM were about 10 times larger than in corresponding whole cell patch-clamp experiments with a better signal-to-noise ratio. This makes the SURFE^{2}R technique at the very least a strong competitor to patch clamp methods, including au-

tomated patch-clamp, when it comes to performing drug screens. This is especially true when considering that the SURFE^{2}R fulfils the conditions of high robustness, automation and easy handling that are very useful for this task.

When it comes to ion channels, the SURFE^{2}R so far has found much less application. A major disadvantage is that the membrane potential, which drives transport through ion channels, cannot be fully controlled. To compensate for the lack of a membrane potential, a gradient of the transported ion has to be applied instead [167]. Furthermore, there is less of a problem with the signal-to-noise ratio of ion channels in patch clamp experiment and hence in this respect there is not much gain using the SURFE^{2}R. Nevertheless, the other mentioned advantages for drug screening purposes remain and therefore the SURFE^{2}R remains a viable alternative to automated patch clamp for these types of experiments.

2.5 Non electrophysiological transport assays

Even though electrophysiogical methods are the gold standard when it comes to measuring activity of membrane transport proteins, there are alternative methods that are frequently used in practice as well. These methods, in general, are either based on detecting a change in fluorescence upon substrate translocation or they use a radiolabeled substrate. Both principles can be applied to study either ion channel or transporter activity and will be briefly introduced in the following sections.

2.5.1 Fluorescence transport assays

Fluorescence based assays are indirect methods to detect ion transport as ionic currents are not recorded directly, but either membrane-potential dependent or ion-concentration-dependent changes of fluorescence signals are measured [176]. Fluorescence based methods find widespread application in primary drug screens, where whole cells, overexpressing the target protein, are loaded with a cell-permeable dye that detects ion influx when a hit binds to the target. High-throughput versions of these assays makes them particularly useful for that purpose [176].

The principle of using fluorescent probes can be applied as well to measure uptake of reconstituted protein into proteoliposomes. Depending on the desired time resolution, uptake can be measured in a normal fluorometer or, when high time resolution is required, on a stopped flow apparatus. A high time resolution is often required when the goal is to obtain biophysical parameters, such as transport rate constants or Michaelis constants for particular substrates. To obtain a K_M, the initial rates of transport have to be measured at different substrate concentrations where the highest concentration has to yield the maximum rate of transport. With sufficient quality of data, a rate constant for transport (k_{cat}) can be calculated as well. One condition that has to be met is that the fluorescent response is linear with substrate concentration over a certain range, such that the change in fluorescence can be directly related to the change in substrate concentration

inside the vesicles. An example is provided by Chao et al. for the Zn^{2+} transporter ZitB of the CDF family [177]. It has to be added though that the turnover number obtained in this paper may still contain a large error because the authors had to assume that all their protein was functionally reconstituted.

Although fluorescence based methods are a very useful tool to study transmembrane transport of proteins, there are some drawbacks in their application, one of these being the requirement for a dye. Finding a suitable dye for a specific assay is not always an easy task. Sometimes it is hard to find a dye with a high enough selectivity for the substrate. Although highly selective dyes exist for sensing sodium, potassium or calcium ions, the same cannot necessarily said for transition metals. In particular there appears to be no dye selective for manganese. Other potential issues regarding dyes could be related to substrate affinity, absorption and emission wavelength and pH dependency.

2.5.2 Radioactivity assays

Radioactivity based assays are frequently used for measuring substrate uptake as they have the advantage over fluorescence based approach that they provide a direct measurement of transport and importantly, any arbitrary substrate can be made detectable by labeling it with an isotope. Assays can be performed with whole cells or proteoliposomes by simply adding radioactive substrate to the bath solution and then incubation to allow uptake to

Technique	Advantages	Disadvantages
Patch clamp	high time resolution single channel recordings control of membrane potential	low throughput not applicable for bacteria/organelles
SSM-based electrophysiology	very sensitive optimal for transporters medium throughput	no control of membrane potential not optimal for ion channels
Fluorescence transport assays	Slow and fast transport detectable	low sensitivity requires dye
Radioactivity assays	Any substrate can be labelled	availability of substrates low time resolution safety precautions

Table 2.1: *An overview of different techniques and assays to measure membrane transport. Advantages and disadvantages are lited that are generally associated with the respective technique.*

be completed. After isolating the cells/proteoliposomes from the bath by either filtration or ultracentrifugation, radioactivity of the sample will be indicative of protein activity. A drawback is that often radioactive substrates are not commercially available and their synthesis can be laborious and expensive. The assay is also not suitable if the substrate for a certain transporter are not known yet. A low signal-to-noise ratio might be another issue, in particular when dealing with transition metal ions. These will bind unspecifically to lipid headgroups and therefore lead to a high background. Similarly it might be hard to distinguish ions that are transported from ions that are competitive binders and do not get transported. Finally, the assay requires safety precautions to be met, which can be circumstantial. A general overview of the techniques discussed in this chapter is found in table 2.1 together with their advantages and disadvantages.

Chapter 3

Materials and methods

3.1 Materials and suppliers

Common lab chemicals such as buffers, media components, salts and solvents were purchase either from Sigma (Aldrich) or Melford unless specified otherwise in the chemicals list. Water used in this study was of nanopure grade (resistivity > 18.2 MΩcm^{-1}) and was prepared using a Milli-Q system (Millipore).

Lipids & detergents

E. *coli* polar lipid extract: Avanti polar lipids

1,2-diphytanoyl-*sn*-glycero-3-phosphocholine: Avanti Polar lipids

n-Dodecyl β-D-maltoside: Anatrace (Maumee Ohio, USA)

2,2-Dioctylpropane-1,3-bis-β-D-maltoside: Anatrace (Maumee Ohio, USA)

n-Octyl-β-D-glucopyranoside: Melford

(Transition) metal salts

Manganese(II) chloride tetrahydrate, 99.99 % trace metal basis: Sigma Aldrich

Manganese(II) sulfate monohydrate, ReagentPlus®, ⩾ 99 %: Sigma Aldrich

Manganese(II) gluconic acid, purity not verified: Sigma Aldrich

Iron(II) chloride tetrahydrate, puriss., p. a. ⩾ 99 %: Sigma Aldrich

Cobalt(II) chloride hexahydrate, BioReagent: Sigma Aldrich

Nickel(II) chloride hexahydrate, 99.9999 %: Acros Organics

Copper(II) chloride dihydrate, Reagent, 99 %: Acros Organics

Zinc(II) chloride, Reagent, ⩾ 98 %: Sigma Aldrich

Magnesium chloride, pure: Acros Organics

Calcium chloride dihydrate, BioReagents®: Fisher

Cell culture

Cell culture flasks: TC treated Cellstar® flasks, greiner bio-one

Trypsin-EDTA: Life technologies

Zeocin™: InvivoGen

Blasticidine: Sigma

Tetracycline: Sigma

Dyes and ionophores

Carbonyl cyanide *m*-chlorophenyl hydrazone (CCCP): Fluka

Nigericin: SLS

Valinomycin: Sigma

2-Mercaptopyridine N-oxide sodium (pyrithione): Sigma

Calcium ionophore A23187 (calimycin): Sigma Aldrich

Trisodium 8-hydroxypyrene-1,3,6-trisulfonate (HPTS): Fluka

Calcein: Sigma

Calcium green-1, hexapotassium salt: Fisher Scientific

Fluozin^{TM}-1, tripotassium salt: Fisher Scientific

Fluo-3, pentaammonium salt: Fisher Scientific

SDS-PAGE Gel & Western Blot

PageRuler^{TM} (unstained protein ladder; 10-250 K): Thermo Scientific

PageRuler^{TM} Plus (prestained protein ladder; 10-200 K): Thermo Scientific

Pierce^{TM} 1-Step Ultra TMB Blotting Solution: Thermo Scientific

3.2 Media and Media components

SB media [no salt]

Component	Quantity in 200 mL	Concentration
Tryptone	6.4 g	3.2 % (w/v)
Yeast Extract	4 g	2 % (w/v)

20xNPSC

Component	Quantity (in 500 mL)	Concentration
H_2O	450 mL	-
Na_2HPO_4	35.5 g	0.5 M
KH_2PO_4	34 g	0.5 M
Na_2SO_4	7.1 g	0.1 M
NH_4Cl	26.75 g	1 M

50x5052

Component	Quantity (in 200 mL)	Concentration
Glycerol	50 g	0.5 % (w/v)
H_2O	146 mL	-
Glucose	5 g	0.05 % (w/v)
α-lactose	20 g	0.2 % (w/v)

SB-5052 medium for autoinduction

Component	Quantity (in 400 mL)	Concentration
SB [no salt]	372 mL	-
1 M $MgSO_4$	0.4 mL	1 mM
50x5052	8 mL	1 %
20xNPSC	20 mL	1 x

3.3 Culture of HEK293 cells

TRPM2 was expressed from a stable, tetracycline-inducible, human embryonic kidney (HEK293) cell-line. The cell line was been established in work prior to this thesis [178]. In the expression construct, TRPM2 carries a FLAG tag at the N-terminus. Cells were grown in Dulbecco's modified Eagle Medium F12 (DMEM-F12) that was enriched with 10 % of fetal bovine serum along with penicillin (50 units/mL) and streptomycin (0.5 mg/mL). Growth conditions were 37 °C and 5 % CO_2. Splitting of flasks was performed when cells reached approximately 70 % confluence. The general split ratio was 1:5. To detach cells from the surface, the bottom of the flasks was rinsed briefly with trypsin-EDTA (1 mL, Life Technologies). Excess trypsin-EDTA was removed and flasks incubated for 2 min at 37 °C. After each split selection antibiotics blasticidin (5 μg/mL) and zeocin (400 μg/mL) were added to the flasks. Expression of TRPM2 was induced by tetracycline (1 μg/mL) 24 h prior to harvest. To harvest cells medium was removed and exchanged for ice-cold PBS/EDTA (137 mM NaCl; 2.7 mM KCl; 10 mM Na_2HPO_4; 1.8 mM KH_2PO_4; 1 mM EDTA). After 15 min incubation cells were resuspended with a pipette. Suspended cells were concentrated by centrifugation (850 x g, 10 min, 4 °C). This step was repeated 3 times where each time the supernatant was replaced by fresh PBS/EDTA. From 15 T175 flasks typically a yield of ca. 3 mL of packed cell volume

(PCV) was obtained.

3.4 Isolation of membrane extracts

3.4.1 Isolation of plasma membranes

The membrane samples were kept at 4 °C for the whole procedure, including the centrifugation steps. Ultra centrifugation steps were carried out using an SW40 rotor (Beckman Coulter) on a Beckman ultra centrifuge (Optima^{TM} L-90K or Optima^{TM} L-80). The PCV was first resuspended in homogenisation buffer (25 mM HEPES, pH 7.4; 250 mM sucrose; 1 mM DTT; 0.5 mM PMSF; 1 mM EDTA; "Complete" [Roche, Cat. No. 1836145])in a ratio of 1:1 v/v. Breaking of cells was performed by 5-10 passes through a ball-bearing homogeniser (isobiotec). To purify plasma membranes a protocol was followed that has been designed for membrane preparations for SURFE^{2}R experiments [179]. The homogenate was centrifuged for 10 min at 6000 x g to pellet the nuclei, mitochondrial membranes and cell debris. The supernatant of that step was centrifuged at 100,000 x g for 30 min to pellet the residual membranes. The pellet was resuspended and the sucrose concentration was adjusted to 54 % by adding an appropriate amount of 70 % sucrose solution in homogenisation buffer. The pellet was then overlaid with sucrose solutions of three different concentrations (44 %; 31 %; 9 %). The gradient was run for 1.5 h at 100,000 x g. The bands at the 9/31 and 31/44 interface were collected and diluted ca. 5x with resting buffer (25 mM HEPES, pH 7.4; 2 mM $MgCl_2$). Fractions were pooled at 100,000 x g for

OptiPrep medium volume (μL)	Gradient dilution buffer volume (μL)	Final volume (μL)	OptiPrep final concentration (% w/v)
567	1434	2000	17
666	1334	2000	20
383	617	1000	23
900	1100	2000	27
500	500	1000	30

Table 3.1: *Table of Opti-Prep density gradient medium steps*

30 min. Pellets were resuspended in resting buffer and protein concentration was determined by a BCA assay. 10 % glycerol and 1 mM DTT were added to the buffer and samples were aliquoted (10 - 20 μg total protein per aliquot) and frozen in liquid N_2. Membranes were stored at -80 °C.

3.4.2 Purification of lysosomes

To isolate lysosomes the same protocol was applied as described in the previous section up to and with the homogenisation step. From then on the procedure was different and was based on a protocol reported by Zhao et al. [180]. Centrifugation of the homogenate was done at lower speed (800 x g) to remove only nuclei and cell debris. The supernatant was directly loaded onto an OptiPrep gradient. The constitution of this gradient is shown in table 3.1. The gradient dilution referred to in table 3.1 has the following composition: 25 mM HEPES (pH 7.4), 250 mM sucrose, 2 mM EDTA. Before the sample was loaded OptiPrep^{TM} density gradient medium (60 % w/v iodixanol; sigma) was added to a concentration of 15 % w/v iodixanol. The gradient was run for 3 h at 100,000 x g. The top band containing lyso-

somes was collected, diluted 5x with resting buffer (25 mM HEPES, pH 7.4; 2 mM $MgCl_2$) and pelleted (100,000 x g; 30 min.) BCA assay, aliquoting and freezing was done in the same way as for plasma membranes.

3.5 BCA assay

BSA standards used for calibration ranged between 0.2 and 1.0 μg. Samples and standards were incubated with BCA reagent (50:1 mixture of A: 1.0 % sodium bicinchonic acid; 2.0 % Na_2CO_3; 0.16 % NaK tartrate; 0.4 % NaOH, 0.95 % $NaHCO_3$ and B: 4 % $CuSO_4$) for 30 min at 37 °C. Absorptions were measured in a plate reader at 562 nm.

3.6 SDS PAGE

Resolving gels: 40 % Acrylamide (3.475 mL); 2 % Bis-acrylamide (0.36 mL); 1.5 M Tris, pH 8.8 (2.81 mL); 10 % SDS (0.1 mL); milliQ (4.267 mL); ammonium persulphate (45 μL); tetramethylethylenediamine (24 μL). Stacking gels: 40 % Acrylamide (0.77 mL); 2 % Bis-acrylamide (0.39 mL); 1.5 M Tris, pH 6.8 (0.75 mL); 10 % SDS (0.05 mL); milliQ (3.2 mL); ammonium persulphate (30 μL); tetramethylethylenediamine (9 μL). Gels with the composition indicated above were run as described previously [181]. Samples were mixed with loading buffer (Final conc.: 62.5 mM Tris-HCl, pH 6.8; 2.5 % SDS; 0.00125 % Bromophenolblue; 1.25 % β-mercaptoethanol; 10 % glycerol)and were prepared by warming at 40 °c for 1 h or alternatively boiling at 90 °C for 5 min. After taking the gel out of the chamber it was stained

with coomassie brilliant blue R-250 as reported elsewhere [182].

3.7 Western Blot

To perform western blotting a SDS PAGE gel was run as described in the previous section. After completion of the electrophoresis the gel was soaked in transfer buffer (47.9 mM Tris; 38.6 mM Glycine; 10 % w/v methanol) for 15 min. That gel together with a nitrocellulose membrane were sandwiched between two sheets of filter paper on each side and put into a transfer chamber. The membrane and filter papers have been wetted in transfer buffer prior to use. A current of 50 mA was applied for 42 min to transfer proteins from the gel to the membrane. Binding sides of the membrane were blocked overnight with 3 % bovine serum albumin in TBS-T (50 mM Tris, pH 7.4; 150 mM NaCl; 0.05 % Tween20). The membrane was washed twice for 5 min in TBS-T before incubating with HRP-conjugated anti-FLAG monoclonal antibody (1:1000 in TBS-T) for 1 h. Antibody was washed off 6x with TBS-T for 5 min. Bound antibody was visualised by wetting the membrane with a 1:1 mixture of a luminol enhancer solution and a stable peroxide solution from a kit (SuperSignal® West Pico; Thermo Scientific). The blot was then imaged in a dark box designed for this purpose (G:BOX; Syngene).

The western blot staining procedure was slightly different when blotting for MntH2. For transfer a Trans-Blot® Turbo^{TM} Transfer System (BioRad) was used, following the standard procedure for 1 mini gel (25 V const.; 30 min). Transfer buffer, transfer stacks and nitrocellulose membranes were

used from the Trans-Blot® Turbo^{TM} Transfer Kit (BioRad). After transfer, membranes were blocked as above, before incubating with Anti-His$_6$-HRP conjugated antibody (1:5000) for 1 h. The membrane was washed 3x in blocking buffer (5 min. each) followed by staining with Ultra TMB Blotting Solution (Pierce^{TM}).

3.8 Transformation of competent cells

For transformation of competent cells 1 μL of plasmid DNA was added to 50 μL of competent cells on ice. After an incubation time of 50 min on ice cells were heat shocked at 42 °C for 60 s followed by another 2 min incubation on ice. Cells were then diluted 1:10 with LB medium and incubated in an orbital incubator (37 °C; 230 rpm) for 50 min. Cells were spun down at 16,200 g for 2 min and 200 μL of the supernatant was removed. The pellet was resuspended in the remaining supernatant and spread on a LB-agar plate containing the appropriate antibiotic that was incubated overnight at 37 °C.

3.9 Purification of plasmids

Following a transformation (section 3.8 into omnimax cells, single colonies were selected from the plates and cells transferred into 5 mL LB medium including antibiotics. After incubation overnight in an orbital incubator (37 °C; 230 rpm) plasmids were purified using the ChargeSwitch®-Pro Plasmid MiniPrep kit (invitrogen).

3.10 Overexpression of metal transporters

Overexpression of all metal transporters was performed in SB-autoinduction medium. All media in the process contained 100 μg/mL carbenicillin as the selection antibiotic. BL21*(DE3) cells harbouring the plasmid pRARE2 were transformed as described in section 3.8. Cells from single colonies were transferred into 5 mL of LB medium in a 50 mL Falcon tube and incubated overnight in an orbital shaking incubator (37 °C; 230 rpm). SB-autoinduction medium (500 mL) was prepared in baffled flasks (2 L) and each of the flasks was inoculated with a single LB starting culture (5 mL). Flasks were incubated (37 °C; 230 rpm) for 22 - 24 h to complete overexpression of protein.

3.11 Expression in the fermentor

For a fermentor growth an agar plate with bacterial colonies transfected with the pBT294CVH plasmid (3.8 were provided to the fermentation facility together with the dry components for 30 L SB-autoinduction medium. All further steps were then carried out by Dr David Sharples. The fermentation system in use was an Applikon fermentor (ADI075/ADI 1010, 40 L Bio Pilot System) which has a Steam In Place (SIP) system with a working volume of 30 L of medium.

3.12 Overexpression of HRV-3C protease

Overexpression of HRV-3C protease followed mainly the same procedure as applied for metal transporters. Competent BL21*(DE3) cells without the plasmid pRARE2 were transfected with the plasmid pET28-His-HRV-3C. Overexpression was performed in SB-autoinduction medium and was performed at 30 °C. The selection antibiotic was kanamycin (25 μg/mL).

3.13 Isolation of bacterial inner membranes

3.13.1 Large scale expression

Cultures from autoinduction were spun down in a high-speed centrifuge (Sorvall Evolution RC) for 15 min at 7,000 x g using a SLC-6000 (Sorvall) rotor. The supernatant was removed and cells were resuspended in lysis buffer (100 mM HEPES, pH 7.0; 150 mM NaCl). From this step the cells were constantly kept at 4 °C throughout the whole procedure. To the resuspended cells PMSF (0.5 mM) was added not more than 30 min before the lysis step. Cells were then homogenised using a cell-homogeniser (IKA®T18 basic, ULTRA-TURRAX®) and lysed by passing them twice through the cell disruptor (CONSTANT SYSTEMS LTD) at 30 kpsi. Unbroken cells were removed by centrifugation at 12,000 x g for 30 min. Membranes were harvested by centrifugation at 100000 x g for 60 min and resuspended in lysis buffer. The membranes were washed twice by resuspension in lysis buffer and centrifugation, then snap frozen in liquid nitrogen and stored at

-80 °C.

3.13.2 Small scale expression

If expression of protein was performed only in a small culture (50 mL), the protocol for isolating spheroplasts was different from when protein was expressed in a 4 L culture. This protocol is based on water lysis and adapted from a method by Kaback [183]. 50 mL culture from overnight growth were spun down in a JLA16.250 rotor on a Sorvall highspeed centrifuge (6500 x g ; 8 min; 10 °C). The pellet was resuspended in 10 mL 0.2 M Tris-HCl, pH8. This was followed by shaking the cells for 20 min in an orbital incubator (250 rpm; 25 °C). After shaking, 4.85 mL of a sucrose containing buffer (1 M sucrose; 1 mM EDTA; 0.2 M Tris-HCl, pH 8.0) was added to the cells, followed by brief vortexing. Precisely 1.5 min after adding the sucrose buffer, 65 μL of lysozyme (10 mg/mL) resuspended in the sucrose buffer was added on top, which was followed again by briefly vortexing the mixture. The lysozyme was allowed to act for 30 seconds (timed) before 9.6 mL of nanopure water was added. The final suspension was shaken in the orbital shaker (20 min; 25 °C) for another 20 min to allow spheroplast formation. Inner membranes were pelleted by centrifugation (25'000 x g; 20 min; 4 °C) followed by resuspension in 15 mL of nanopure water and incubation for 30 min at room temperature. The membranes were collected as in the previous step and washed in sodium phosphate buffer (pH 7.2) containing 1 mM mercaptoethanol. This step was repeated twice, before membranes

were frozen in liquid nitrogen and stored at -80 °C.

3.14 IMAC purification of MntH2

For purification, membranes were solubilised in solubilisation buffer (25 mM HEPES, pH 8.0; 300 mM NaCl; 5 % glycerol; 1.5 % DDM, 10 mM Imidazole) at a concentration of 3 mg/mL total membrane protein and incubated on a roller mixer at 4 °C for 2 h. The sample was centrifuged at 100,000 x g for 1 h to remove insoluble material. Purification was performed on an AKTA (Äkta^{TM} pure; GE Healthcare Bio-Sciences AB) using a Ni-NTA column (His Trap HP, 5 mL). The flowrate was kept at 0.5 mL/min throughout the experiment. The column was equilibrated with 5 column volumes (CV) of equilibration buffer (25 mM HEPES, pH 7.0; 300 mM NaCl; 5 % glycerol; 0.05 % DDM, 10 mM imidazole). After loading the sample the column was washed with 10 CV of wash buffer containing 80 mM imidazole. To elute the protein the imidazole concentration was then increased gradually up to 400 mM (16 CV). Fractions containing pure protein, as confirmed by SDS-PAGE, were pooled and imidazole was dialysed out against dialysis buffer (25 mM MES, pH 6.0; 150 mM NaCl; 5 % glycerol; 0.05 % DDM)(1:500 V/V sample/buffer) for 2 days with 2 changes of buffer.

3.15 IMAC purification of HRV-3C protease

The PBS buffer used in this protocol had the following composition: 10g/L NaCl; 0.25 g/L KCl; 1.8 g/L Na_2HPO_4; 0.3 g/L KH_2PO_4.

3.15 IMAC purification of HRV-3C protease

Cells were centrifuged using an SLC-6000 rotor on a Sorvall centrifuge (15 min, 7000 x g, 4 °C). The pellet was resuspended in 2 mL of disruption buffer (PBS, pH 7.4; 0.5 mM EDTA) per g of cells using a cell homogeniser (IKA®T18 basic, ULTRA-TURRAX®). The cells were lysed by two passages through the cell disruptor (CONSTANT SYSTEMS LTD) at 30 kpsi. Cell debris was removed by centrifugation on a JA25.50 rotor on a Sorvall centrifuge (27'000 x g; 15 min; 4 °C). The supernatant was diluted in PBS buffer (pH 8.0) containing Triton X-100, imidazole and DTT. The concentration of these compounds were previously determined such that the final concentrations in the sample were 0.1 % Triton X-100, 7.5 mM imidazole and 1 mM DTT. Before loading onto the IMAC column, the sample was filtered through a stericup filter (0.45 μm). IMAC chromatography was performed on the Äkta on a Ni-NTA column (His-trap HP, 5 mL) that was pre-equilibrated with 5 CV of equilibration buffer (PBS, pH 8.0; 1 mM DTT; 7.5 mM imidazole). After the sample was loaded, the column was washed with another 20 CV of equilibration buffer followed by a wash of 5 CV with extra wash buffer (PBS, pH 8.0; 1 mM DTT; 200 mM NaCl; 30 mM imidazole). Following this step the buffer was changed to extra wash buffer without NaCl and the protein eluted in a gradient from 30 mM to 250 mM imidazole over 15 CV. Fractions from the Äkta containing HRV-3C were pooled and dialysed overnight in dialysis buffer (50 mM HEPES, pH 7.5; 200 mM NaCl; 1 mM EDTA; 10 % glycerol). For storage the protein was

concentrated to 5 mg/mL and glycerol was added to a final concentration of 50 % glycerol.

3.16 Size exclusion chromatrography

After HisTrap purification of MntH2 the protein eluates were pooled and concentrated to a volume of 1 mL or less using 30 kDa concentrators (vivaspin). Size exclusion chromatography (SEC) was then performed on a superdex 200 pg column using the AKTA at a flowrate of 0.5 mL/min. The exact buffer composition used for SEC varied between experiments and details can be found in chapter 7.

3.17 Reconstitution

3.17.1 Reconstitution of MntH2 using OGP

E. coli polar lipid extract (Avanti) from chloroform stock were dried under nitrogen flow and residual solvent was removed by desiccation under vacuum for 2 h. Lipids were hydrated with reconstitution buffer (25 mM HEPES/NaOH, pH 7.0; 150 mM NaCl) to result in a cloudy, but homogeneous suspension (5 mg/mL lipid concentration). Lipids were dissolved by adding OGP from 0.25 M aqueous stock up to a final concentration of 55 mM OGP. MntH2 from -80 °C (concentration of 1.3-1.8 mg/mL) was added to give the desired ratio of protein/lipid w/w (typically 1:10) and sample was incubated for 15 min on ice. All the following incubation steps were performed on ice. In the next step biobeads were added to a concentration

of 0.07 g/mL protein-lipid-detergent suspension followed by incubation for 30 min. Reconstitution was completed by another three subsequent steps of biobead addition: Addition of 0.07 g/mL biobeads and incubation for 60 min. Addition of 0.14 g/mL biobeads and incubation for 60 min. Addition of 0.14 g/mL biobeads and incubation for 120 min. Finally the supernatant was collected and aliquots were frozen in liquid nitrogen and stored at -80 °C.

3.17.2 Reconstitution of MntH2 using DDM

Reconstitution of MntH2 was performed based on the protocol by Geertsma et al. [184] optimised for MntH2. *E. coli* polar lipid extract (Avanti) from chloroform stock were dried under nitrogen flow and residual solvent was removed by desiccation under vacuum for 2 h. Dried lipids were resuspended in reconstitution buffer (10 mM HEPES, pH 7.0; 150 mM NaCl) to a concentration of 5 mg/mL. Lipids were extruded by at least 11 passages through a 200 nm track-edged polycarbonate membrane filter. The lipid concentration was adjusted to 4 mg/mL and DDM was added to a final concentration of 1 %. Some reconstitutions have been carried out using less DDM (0.2 / 0.5 %) but these samples did not perform as well in electrometric measurements. Protein was added to a concentration of 1:10 protein/lipid (w/w) and incubated for 15 min on ice. Detergent was removed by stepwise addition of biobeads as described elsewhere [184].

3.18 CPM assay

7-Diethylamino-3-(4'-Maleimidylphenyl)-4-Methylcoumarin (CPM) from 5 mg/mL stock (DMSO) was diluted 1:50 in aliquots of each assay buffer (100 μL) to make CPM working stock solutions. Aliquots were vortexed and equilibrated for 10 min at 20 °C. In 0.3 mL PCR tubes 50 μL reactions were set up first by diluting protein into assay buffer to yield a final concentration of 0.05 mg/mL protein. CPM from the corresponding working stock solution was then added to the reaction as well to a 10^{th} of the total reaction volume. Reactions were vortexed and left on ice for 10 min before the samples were run through a temperature ramping program on a PCR machine (Stratagene Mx3005P, Agilent Technologies). The temperature ramping program equilibrated samples for 3 min at 25 °C and then increasing temperature in 70 cyles of 15 s at 1 °C per cycle.

3.19 SEC-MALS

SEC-MALS runs were performed by Dr Maren Thomsen. Protein samples of 10-30 g of purified protein (1-3 mg/mL) were subjected to analytical size exclusion chromatography using a Schimadzu UFLC HPLC system. The eluting samples were analysed with the coupled Wyatt Optilab rEX UV absorbance and refractive index, and Wyatt miniDAWN TREOS multi angle laser light scattering detectors. Molecular mass, as well as protein and detergent contents were calculated with Wyatt ASTRA software. MntH2 was

run on a Superdex 200 10/300 column (GE Healthcare) pre-equilibrated with running buffer (for details see section 5.5) for 16 hrs at room temperature. A control run with carbonic anhydrase was performed on the pre-equilibrated column before the experimental runs. This step allowed to factor and correct for the time delay of the sample between each detector, when aligning the traces.

3.20 Mass Spectrometry

Mass spectrometry experiments were performed at the mass spectrometry facility of the faculty of biological sciences at the University of Leeds. Samples of MntH2 protein were provided in concentrations of 0.4 mg/mL (Peak1 from IMAC) and 0.3 mg/mL (Peak2 from IMAC) in SEC running buffer (25 mM MES, pH 6.0; 150 mM NaCl; 0.05 % NMDG).

3.21 SURFE^{2}R experiments

3.21.1 Sensor preparation

Sensors were prepared according to the manufacturer's protocol [179] with slight modifications. Sensors were incubated with 0.1 mM 1-ODT solution in 50 % IPA for 15 min. Thiol was rinsed away with IPA three times and the sensor was dried under a nitrogen flow. It was left to dry for 15 - 30 min to allow residual IPA to evaporate. 3 μL of SensorPrep B (7.5 mg/mL 1,2-diphytanoyl-phosphatidylcholine in decane) was added to the sensor followed immediately by 50 μL of non-activating buffer B (25 mM HEPES/NaOH,

pH 7.0; 150 mM NaCl; 2 mM $MgCl_2$). This was incubated for 30 - 60 min at 4 °C. From this step on the sensor preparation protocol differed slighly, depending on whether the sample was constituted of proteolipsomes (MntH2), eukaryotic membranes (TRPM2) or bacterial inner membranes (NupC, metal transporters).

MntH2

MntH2 proteoliposomes were thawed from frozen stock, diluted 1:50 in non-activating buffer B and sonicated with 10 pulses (UPH50, Dr. Hielscher GmBH, tip-size = 1 mm, Amplitude = 0.5, cycle = 0.2). The buffer was removed from the sensor and replaced by 100 μL of the proteoliposome sample. Sensor preparation was completed by centrifugation of the sensors (800 g; 45 min; 4 °C).

Eukaryotic membranes

All buffer was removed from the sensor and replaced by buffer C (25 mM HEPES/NMG, pH 7.4; 100 mM NMGCl; 2 mM $MgCl_2$), where membrane samples have been suspended in by pipetting up and down 30 times. Typically the amount of sample was such that 10 μg of total protein was added to the sensor. Adsorption of membrane fragments was assisted by centrifugation of the sensors (800 g; 45 min; 4 °C).

Bacterial inner membranes

Spheroplasts containing transport protein were mixed with 200 nm vesicles from E. *coli* polar lipids prepared as described in section 3.17.2 in a ratio of

1:9 lipid/total protein (w/w) and treated with 100 pulses of tip-sonication (UPH50, Dr. Hielscher GmBH, tip-size = 1 mm, Amplitude = 0.5, cycle = 0.2). 2 μg of total protein (5 μL of mixed proteoliposome suspension) was then added to a sensor that was preloaded with 100 μL buffer B (composition varied depending on protein; details are specified in chapter 6)). Centrifugation of sensors was performed as above (800 g; 45 min; 4 °C).

3.21.2 Experiments with TRPM2

For experiments with TRPM2 on the SURFE^{2}R a protocol with two solution exchanges and three buffers A, B and C was used. The exact composition of buffers varied (see chapter 4, table 4.1) but some rules are generally applied: 1. The base components for all buffers were 25 mM HEPES, pH 7.4 and 2 mM $MgCl_2$. Depending on whether KCl or NaCl were added to the base buffer, the buffer pH would be adjusted accordingly by KOH or NaOH. Buffer C and B are identical except that NaCl and KCl concentrations are exchanged (eg. if buffer C contains 140 mM KCl, buffer B would contain 140 mM NaCl instead). Buffer A is identical to buffer B, but it contains varying concentrations of the activating compound(s) (Ca^{2+} and/or ADPR). The flow rate was kept at 200 μL/s during measurements.

3.21.3 Experiments with MntH2

Experiments on the SURFE^{2}R N1 instrument at were performed at room temperature. Typically a three phase solution exchange protocol was used: (1) Non activating buffer B (1 second), (2) activating buffer A (= buffer

B + 100 μM of transition metal salt)(1 second), (3) non activating buffer B (1 second). The flow rate was set to 250 μL/s. Each measurement was repeated at least four times and sensors were used for up to three days. Experiments with his-tagged MntH2 were performed from in total three different expressions. An additional expression was performed to get his-tag cleaved MntH2.

3.22 Fluorescence based assays

3.22.1 Tryptophan fluorescence

Tryptophan fluorescence assays were performed on a fluorimeter (Photon Technology International) at 20 °C with an excitation wavelength of 280 nm. The protein concentration (BSA and MntH2) was 0.2 mg/mL in assay buffer (10 mM MHC, pH 8.0; 150 mM NaCl; 2 mM $MgCl_2$; 0.05 % DDM) and measurements were performed in a 400 μL quartz cuvette. Transition metal ion salts were added from freshly prepared stock solutions in assay buffer as appropriate. Before each measurement a waiting time of at least 2 min was included to allow equilibration of the metal ions with the sample.

3.22.2 Assay of H^+ cotransport using the pH sensitive dye HPTS

Vesicles for proton transport assays were prepared using the OGP reconstitution protocol (section 3.17.1) with some modifications. E. *coli* polar lipids were resuspended in reconstitution buffer (5 mM MOPS, pH 7.0; 150

mM KCl; 1 mM HPTS) and dissolved by adding OGP to a concentration of 55 mM. Protein was added to a protein/lipid ratio of 1:70 w/w followed by extensive dialysis (3 days with 2 changes of buffer) against reconstitution buffer. In the first dialysis step 1 mM HPTS was still added to the buffer but was left out in the following steps. For assays proteoliposomes were typically diluted 1:10 in reconstitution buffer to a concentration of 0.5 mg/mL lipid. To record changes in fluorescence, the emission at 510 nm was detected using two different excitation wavelengths of 400 and 448 nm on a fluorimeter (Photon Technology International). To get data points and confidence the ratio between the signal from the two excitation wavelenghts was calculated and monitored for 3x30 s with 30 s break in between for each data point measured. To create pH jumps in the outside buffer 1 μL of 0.5 M HCl or KOH was added to the cuvette. The control ionophore nigericin was added to a concentration of 0.1 μM from 0.1 mM aqueous stock.

3.22.3 Fluorescence transport assay with the transition metal sensitive dye calcein

To prepare proteoliposomes for calcein fluorescence based transition metal uptake assay a reconstitution was performed according to section 3.17.2 with a MOPS reconstitution buffer (5 mM MOPS, pH 7.0; 150 mM KCl; 250 μM calcein). Dialysis was performed in reconstitution buffer without calcein for 36 h with two changes of buffer. Liposomes were diluted 1:100 (0.04 mg/mL lipid concentration) and dye quenching was monitored at 515 nm with an

excitation wavelenght of 490 nm on a fluorimeter in a quartz cuvette. All buffers were filtered (PES; 0.22 μm) before the experiment.

3.22.4 Stopped-flow

Proteoliposomes for stopped flow experiments were performed as described in the previous section, but instead of removing the calcein by dialysis, the dye was washed out in ultracentrifugation steps: After the incubation with biobeads, the samples were diluted 1:60 and centrifuged in a Ti45 rotor (43'000 rpm; 1h 30 min; 4 °C). The supernatant was removed and the pellet washed once, by repeating the previous step. For experiments the proteoliposomes were diluted in reconstitution buffer to a final concentration of 0.2 mg/mL. Experiments were performed on a stopped-flow apparatus (SX20; Applied Photophysics) that has a dead time of ca. 1 ms. The excitation wavelength was set to 492 nm using a monochromator (bandpass = 4.65 nm/mm) and emission wavelengths were filtered by a high pass filter (515 nm; Applied Photophysics) with a transition of 50 % at 515 nm and $\geqslant$ 0.001 % at 492 nm. Fluorescence was detected by a fluorescence photomultiplier (Type R6095; Applied Photophysics) with a detection range of 300-650 nm. The temperature of the water bath was set to 20 °C. For measurements, proteoliposomes and solutions of manganese chloride in reconstitution buffer were prepared in separate syringes and mixed in a ratio of 1:1 in the reaction cell. Care was taken that buffers in both cells were exactly identical and were filtered (PES; 0.22 μm) before the experiment. Usually, the manganese

chloride concentration was 200 μM in the syringe to give a final concentration of 100 μM in the cell. To determine F_{max} by performing experiments with calimycin (0.5 μg/mL) added to the manganese chloride solution.

3.23 Crystallisation trials

Crystallisation trials were set with protein purified by IMAC and SEC as described in sections 3.14,3.16. The protein was concentrated in 30 kDa spin-concentrators (vivaspin) up to varying concentrations between 3 and 7 mg/mL. The exact concentrations for each trial and are specified in chapter 7. Trials were set up on MRC 96-well 3-drop plates with help of a crystallisation robot (NT8). As well solutions three different commercially available screens (MemGold, MemGold2, MemSys/MemStart; Molecular Dimensions Ltd) were used that are designed specifically for the crystallisation of membrane proteins. In each well one of the drops corresponded to protein from one of the two peaks obtained from the IMAC purification step. Normally protein was mixed in a 1:1 ratio with well solution (0.2 μL total drop volume) but optionally the third drop was used to test a different ratio of 1.75:1 protein to well solution. Plates were stored either at 4 °C or at 20 °C and were observed for at least one month for crystal growth.

3.24 Data analysis

For data analysis and figures the software package R was used throughout this thesis [185].

Chapter 4

TRPM2

In this chapter the work is presented that has been performed on the human TRPM2 channel. TRPM2 was studied to investigate its proposed role in the cell death of pancreatic β-cells. An introduction to this was given in section 1.3.2. The goal was to isolate plasma membrane- as well as lysosomal extracts from TRPM2 overexpressing cells and use these extracts to perform electrophysiological experiments with the SSM-based technique.

4.1 Expression and isolation of membrane extracts

This section provides a short version of protocols for TRPM2 overexpression and isolation of lysosomes and plasma membranes. More detailed protocols are described in chapter 3, sections 3.3-3.4.2. TRPM2 was expressed in HEK293 cells that was grown in DMEM-F12 medium. Added antibiotics were penicillin/streptomycin as well as the selection antibiotics zeocin and blasticidin. Expression was induced by tetracycline one day before cells were

harvested. Cells were collected by resuspension in ice cold PBS/EDTA and washed three times. The usage of trypsin in this step was avoided in order to prevent potential damage of TRPM2 by trypsin. Breaking up of cells was performed using a ball-bearing homogeniser. To isolate membrane fragments two different protocols were applied, depending on which organelles were to be purified. Plasma membranes were obtained from a sucrose gradient (9/31 interface; section 3.4.1) whereas lysosomes were purified in an OptiPrep gradient (table 3.1. In OptiPrep gradients 2-3 bands were obtained and lysosomes were isolated from the first band at low OptiPrep density. The membrane fragments were harvested by ultra centrifugation and resuspended in storage buffer (25 mM HEPES, pH 7.4; 2 mM $MgCl_2$; 10% Glycerol; 1 mM DTT). Membranes were frozen in liquid N_2 and stored at -80 °C. Western blot analysis was performed to ensure that TRPM2 was present in the samples (fig. 4.1). Lysosome and plasma membrane samples showed both a clear band at the correct molecular weight, confirming TRPM2 expression and localisation in plasma membrane and/or lysosomal fractions. The band at lower molecular weight indicates that some protein has degraded during membrane purification.

It was hypothesised that this degradation takes place due to proteolytic activity, that might be not inhibited by the "complete" protease inhibitor cocktail (see chapter 3, sections 3.4.1-3.4.2). Consequently, the protocol was adjusted by adding the protease inhibitor pepstatin, which reversibly in-

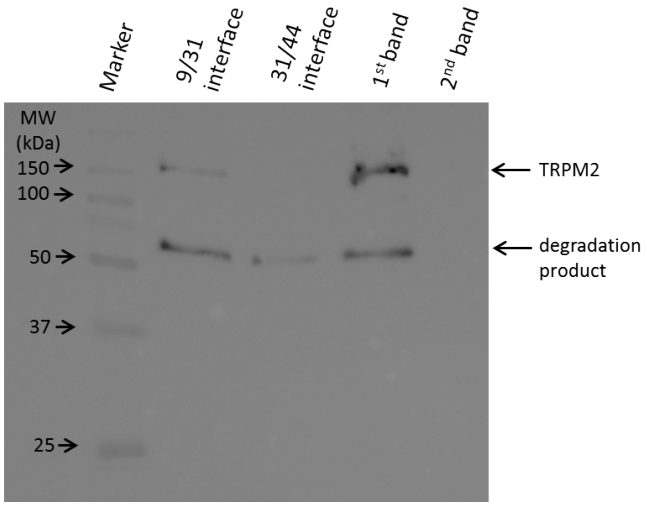

Figure 4.1: *Western Blot of samples obtained from density gradients. From left to right: Marker, 9/31 interface (sucrose), 31/44 interface (sucrose), 1^{st} band (OptiPrep, low density), 2^{nd} band (OptiPrep, medium density). Plasma membranes and lysosomes were isolated from the 9/31 and 1^{st} band respectively.*

hibits aspartyl proteases, to the homogenisation buffer and to the gradient diluent. To track at which stage degradation occurs, samples of membrane preparations were collected at different steps of the purification (whole cells, homogenised cells, post nuclear supernatant). The western blot showed clearly that degradation of the channel was prevented, as there is no low molecular weight band (fig.4.2). It does seem likely therefore, that pepstatin solved the problem of degradation by preventing proteolytic cleavage. The control bands on the blot (fig. 4.2) are from membranes of HEK293 cells not induced with tetracycline. The blot confirms that these cells did not express TRPM2.

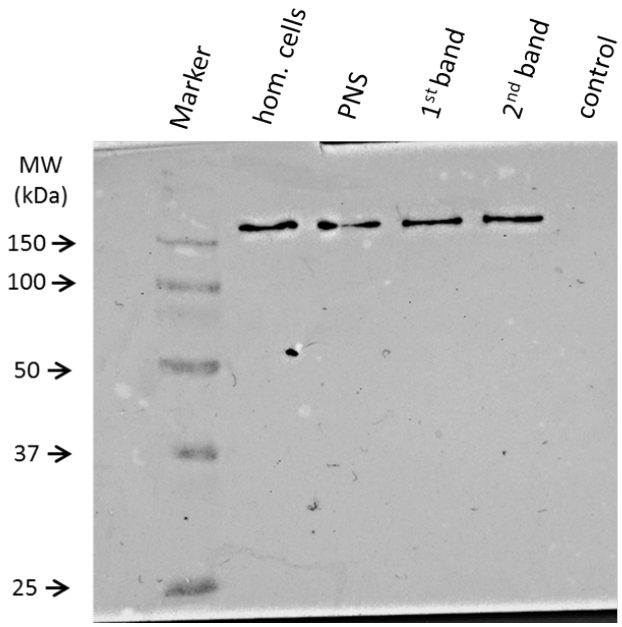

Figure 4.2: *Western Blot of TRPM2. The lanes were loaded with samples from different steps of an OptiPrep density gradient as indicated in the labels above the lanes. The control shows the first OptiPrep band from a preparation with non-induced HEK293 cells.*

4.2 SURFE^{2}R of TRPM2

When starting experiments with a new protein with the SURFE^{2}R, there are a few things that have to be optimized as for instance the amount of total protein added to the sensor or the lenght of sensor incubation to name only two [179]. This can be quite a challenging task, especially if, as in the case of TRPM2, it is not completely clear what the exact conditions are, that are needed to activate the channel. Even though there is no doubt that ADPR is an activator of the channel, a wide range of EC_{50} values from 1 to 100 μM has been reported ([83, 84, 186]). Moreover, Ca^{2+} has been

reported to influence the channel to some very different degrees. There is a general consensus that Ca^{2+} facilitates channel activation but it is less clear what concentration or whether intracellular, extracellular or both Ca^{2+} are needed [186]. Problematic in that context is that it cannot be excluded that Ca^{2+} alone is sufficient to activate TRPM2 [187]. This means that one cannot simply add Ca^{2+} to all buffers used in SURFE^{2}R experiments, because in this case TRPM2 might be permanently activated. The situation is further complicated by the fact that the orientation of TRPM2 in the membrane may matter a great deal for these measurements. The primary gating molecule, ADPR, has its binding side on the intracellular side of TRPM2. Hence, TRPM2 has the wrong orientation in plasma membrane for being activated by this molecule. Fortunately, experiments could be performed as well on TRPM2 in lysosomes, which has its intracellular side facing outwards.

Purified membrane samples were subjected to a number of different conditions where parameters indicated above were varied by adjusting buffer compositions used for the SURFE^{2}R workflow. As described in chapter 2, section 2.4, three different buffers (resting buffer C, non-activating buffer B and activating buffer A) are used for the two-solution exchange protocol to activate ion channels. A summary of the different buffer conditions tested is shown in table 4.1. First some fixed components were set, which were 25 mM HEPES, pH 7.4 and 2 mM $MgCl_2$ in all buffers. In addition the

concentration ADPR in the activating buffer was set to be 100 μM ADPR. Variable parameters included mostly the cationic species in buffer salts and the Ca^{2+} concentration in different buffers. In the beginning KCl and NaCl were used in concentrations of 100-140 mM to establish the cation gradient necessary to perform experiments. For instance, 140 mM KCl in buffer C would be compensated by 140 mM NaCl in buffers B and A or vice versa. Later it was preferred to replace Na^+ or K^+ in buffer C by a bulky cation, which could safely assumed to not leak out of membrane vesicles. Ca^{2+} was generally added in a concentration of 1-100 μM to buffers B and A, but not to buffer C. This was to exclude the possibility of TRPM2 being activated already in buffer C by the presence of Ca^{2+}. Nevertheless, some experiments were conducted in which 1 mM Ca^{2+} was added to all three buffers to allow time for Ca^{2+} to bind prior to the activation by ADPR. Finally, experiments were performed with 200 nM calmodulin. In this experiment the buffer salts were 100 mM NMGCl in buffer C and 100 mM NaCl in buffer B/A. Ca^{2+} was added in a concentration of 100 μM to buffers A and B. Despite all this effort no signal from the TRPM2 channel on the $SURFE^2R$ could be obtained. (fig. 4.3).

4.3 Discussion

In this chapter plasma and lysosomal membranes from HEK293 cells were successfully purified and subjected to a number of different conditions to monitor TRPM2 activity. Some optimisation was required until it was found

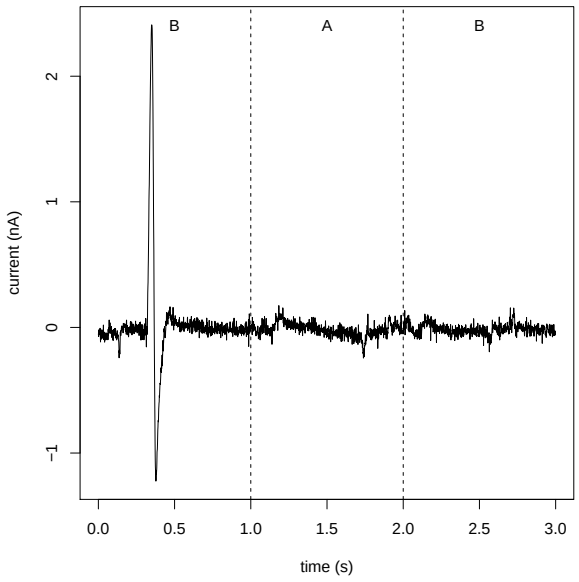

Figure 4.3: *SURFE^{2}R measurement of TRPM2. The trace is representative for all experiments with TRPM2. Samples from in total four biological replicates were used. The basic buffer used in the experiment was 25 mM HEPES/NMG, pH 7.4 with 2 mM $MgCl_2$. Buffer C contained in addition 100 mM NMG^+ and buffers A and B 100 mM NaCl and 100 µM $CaCl_2$. As the only buffer, A contained 100 µM ADPR. The vertical dashed lines indicate the change from B to A and back.*

that the addition of the protease inhibitor pepstatin during membrane purification is necessary to avoid channel degradation. This was important because it could not be excluded that the degraded channel renderes membranes leaky to cations which could dissipate the ion gradient in SURFE^{2}R experiments. Nevertheless, no ion transport could be detected with the SURFE^{2}R methodology. As discussed in the introduction (section 1.2.2) TRPM2 can adopt an inactive state after repeated activation. It is thus possible that TRPM2 was isolated in an inactive state, either a physiological relevant inactive state or one due to experimental procedures that were

	C resting buffer	**B** non-activating buffer	**A** activating buffer
1	100-140 mM NaCl	100-140 mM KCl 1-100 μM $CaCl_2$	100-140 mM KCl 1-100 μM $CaCl_2$ 100 μM ADPR
2	100-140 mM KCl	100-140 mM NaCl 1-100 μM $CaCl_2$	100-140 mM NaCl 1-100 μM $CaCl_2$ 100 μM ADPR
3	100 mM NMGCl	100 mM NaCl 1-100 μM $CaCl_2$	100 mM NaCl 1-100 μM $CaCl_2$ 100 μM ADPR
4	100 mM NMGCl 1 mM $CaCl_2$	100 mM NaCl 1 mM $CaCl_2$	100 mM NaCl 1 mM $CaCl_2$ 100 μM ADPR
5	100 mM NMGCl 200 nM calmodulin	100 mM NaCl 200 nM calmodulin 100 μM $CaCl_2$	100 mM NaCl 200 nM calmodulin 100 μM $CaCl_2$ 100 μM ADPR

Table 4.1: *Buffer compositions for SURFE^{2}R experiments on TRPM2. The table shows the different salt- and activating components that were added to buffers A, B and C. All experiments used the same basic buffer: 25 mM HEPES, pH 7.4; 2 mM $MgCl_2$.*

followed. Alternatively, there is a chance that there are cellular factors required for TRPM2 activation that have not yet been identified [104]. The lack of response would then be caused by the absence of these factors in SURFE^{2}R experiments.

Chapter 5

Expression & purification of MntH2

A purification protocol for MntH2 has been established in preceding work [108, 154]. Here, this protocol was developed further and this chapter will discuss some adjustments that have been made. The purified protein was characterised by several techniques addressing different properties of the detergent solubilised protein. These included oligomeric state analysis by SEC-MALS (sec. 5.5 and 5.6), molecular mass determination by mass spectrometry (sec. 5.6.1) and thermal stability analysis by the CPM-assay (sec. 5.7).

5.1 Expression of MntH2

The plasmid for MntH2 overexpression, named pBPT0294-CVH, was designed prior to this thesis [108, 154]. Overexpression is described in detail in section 3.10 and was performed in SB-autoinduction medium (sec. 3.2). The amount of growth culture could vary between expressions from 50 mL (small scale) to 4 L (large scale) up to 30 L (fermentor). From a 4 L growth culture typically a yield of ca. 80 g cells was obtained. For a fermentor growth an agar plate with bacterial colonies transformed with the pBPT0294-CVH plasmid, were provided to the fermentation facility together with the dry components for 30 L SB-autoinduction medium. The yield from a 30 L fermentor growth was between 250 - 300 g cells per growth.

5.2 Extractions of inner membranes

For small sample sizes (∼1 g of cells) inner membranes were isolated following a protocol based on water lysis (section 3.13.2). This protocol uses the osmotic shock from a high sucrose buffer to lyse cells and strip off their outer membranes. More typically, inner membranes were purified from a larger amount of cells, between 80 and 120 g. In this case a cell disruptor was used for cell lysis (section 3.13.1). Expression of protein was confirmed by western blotting (fig. 5.1).

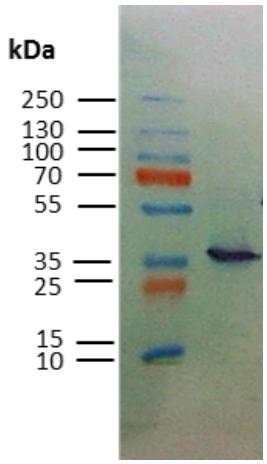

Figure 5.1: *Western blot of bacterial inner membranes containing MntH2. The construct, which has a tag with eight histidine residues on the C-terminus, was stained using HRP conjugated anti-his$_6$ antibody. Overexpression was performed in E. coli BL21* (DE3) harbouring the plasmid pRARE2 using SB-autoinducting medium.*

5.3 IMAC purification

IMAC was performed using two slightly different protocols. The first protocol is similar to the published method [154], with the difference that a linear imidazole gradient is applied to elute the his-tagged MntH2 from the Ni-NTA column, rather than a step gradient. This protocol was applied to improve the purity of MntH2 from the IMAC chromatography step. The second protocol was designed to maximise the yield of MntH2. It is similar to the first protocol but contains some minor changes. The most important change was to increase the solubilisation time of MntH2 into DDM from 1 h to 2 h. To minimise unspecific binding of proteins to the Ni-NTA column the salt concentration in the buffer was raised from 150 mM to 300 mM NaCl. Protein that was purified with the second protocol was purified further by

size exclusion chromatography as described in the following section. Fig. 5.2a shows a purification of MntH2, following the first protocol and fig. 5.2b is from a purification, where the second protocol has been applied.

There are clear differences between the two chromatograms. The most striking one is that when the second protocol is applied, protein does not elute in only one, but in three peaks. By coomassie stain analysis of an SDS-PAGE gel it was confirmed that all three peaks correspond to MntH2 (not shown). Despite this, fractions from the three peaks were kept separately. Protein yields were determined by BCA assays as described in section 3.5: Following the original protocol (fig. 5.2a) yields of 4.0-4.6 mg MntH2 were obtained, starting from $\sim$ 600 mg total protein in extracted inner membranes. Yields from purifications following the second protocol (fig. 5.2b) mounted up to 19 mg (protein from the first two peaks combined), starting from $\sim$ 240 mg total protein. The yields between the two protocols are not directly comparable, because purifications were performed from different expressions.

For storage, samples were dialysed against dialysis buffer (25 mM MES, pH 6.0; 150 mM NaCl; 5 % glycerol; 0.05 % DDM) for 2 days with 2 changes of buffer. Samples were concentrated to a concentration of 1-2 mg/mL followed by freezing in liquid N_2 and storage at -80 °C.

Fraction from IMAC purifications were subjected to coomassie stain and western blot analysis of SDS-PAGE gels (fig. 5.3). Fig. 5.3 shows the bands of the peak fraction from fig. 5.2a. The coomassie stained gel revealed that

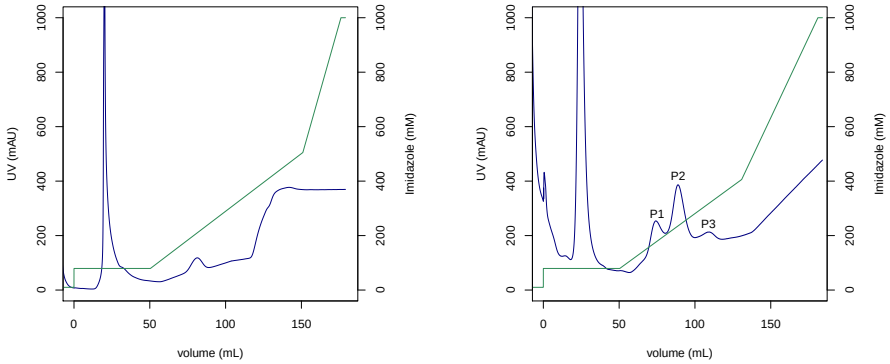

(a) *IMAC chromatogram of MntH2 purification following protocol one (membrane solubilisation for 1 h). Running buffer: 25 mM HEPES, pH 8.0; 150 mM NaCl; 10 % glycerol; 0.05 % DDM; 10 mM imidazole (sample load). The purification was started from ∼600 mg total protein.*

(b) *IMAC chromatogram of MntH2 purification following protocol two (membrane solubilisation for 2 h). Running buffer: 25 mM HEPES, pH 8.0; 300 mM NaCl; 10 % glycerol; 0.05 % DDM; 10 mM imidazole (sample load). The purification was started from ∼240 mg total protein.*

Figure 5.2: *IMAC purification of MntH2 was performed on a Ni-NTA column. Blue: UV, green: Imidazole. The profiles are shown from the wash step (80 mM imidazole), where most impurities come of. After this the imidazole concentration is gradually raised in a shallow gradient. MntH2 is eluted in this gradient as a single peak at ca. 210 mM imidazole in (a) or as three different peaks in (b). Comparing the imidazole concentration at the onsets of the peaks, the second peak in (b) corresponds to the peak in (a). After the shallow gradient the imidazole concentration is raised to 1 M in a steep gradient, to wash off residual protein.*

MntH2 is pure (≥80 %) but for a contaminant at low molecular weight. In the Western blot it was confirmed that the purified protein is MntH2. It was noted that the band of MntH2 showed up at considerably lower molecular weight than its actual mass: The MntH2 construct has a total molecular weight of 61.4 kDa but the protein is running at ca. 40 kDa. It is common for membrane proteins to migrate at a lower than expected molecular weight due to the fact that membrane proteins can retain partial folding in SDS [188]. Results from mass spectrometry experiments showed that the protein

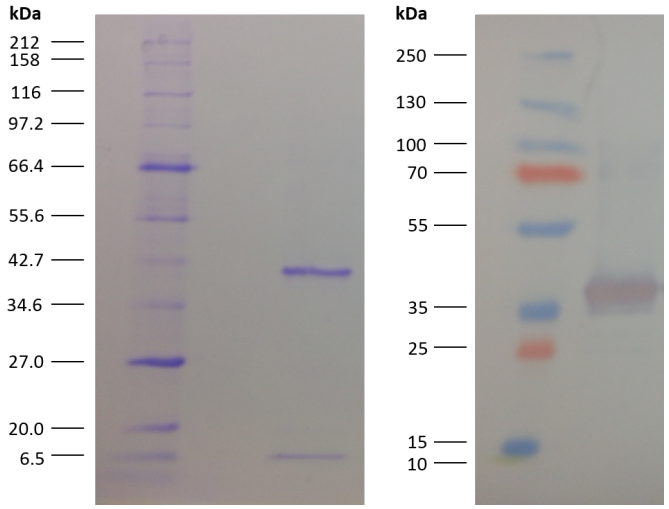

Figure 5.3: *Coomassie stained SDS-PAGE gel and western blot of MntH2 purified by IMAC as in fig. 5.2a. The protein appears to be pure with the exception of a small contaminant at 6.5 kDa. Blotting was performed using HRP-conjugated anti-his$_6$ antibody.*

was intact (sec. 5.6.1)

5.4 Size exclusion chromatography

Size exclusion chromatography was performed exclusively on samples purified following the second purification protocol in IMAC chromatography (fig. 5.2b). As mentioned, samples from the first two peaks were kept separately and from now on are named P1 and P2. The third peak was not collected. Before loading onto the SEC column samples were concentrated to a volume of ca. 1 mL. Along with purifying MntH2, SEC can be used to exchange buffers and the running buffer was identical to MntH2 storage buffer (25 mM MES, pH 6.0; 150 mM NaCl; 5 % glycerol; 0.05 % DDM). P1 and P2 were both run on a superdex 200 pg column and they elute at

the same volume (fig. 5.4). P2 has a larger shoulder than P1, which might indicate that there are more aggregates in P2. This does not necessarily mean that P2 is more prone to aggregate, because aggregation is correlated to protein concentration, which is higher in P2 than in P1. MntH2 purified by SEC was loaded on an SDS-PAGE gel which was stained with coomassie brilliant blue (fig. 5.5). Both samples run at the same molecular weight of ca. 40 kDa and no impurities are detected on the gel. The yields from this purifications were ca. 3-3.8 mg protein for P2 and 1-1.5 mg for P1 (nanodrop), starting from 7-8 mL inner membrane samples with a total protein concentration of ca. 30 mg/mL.

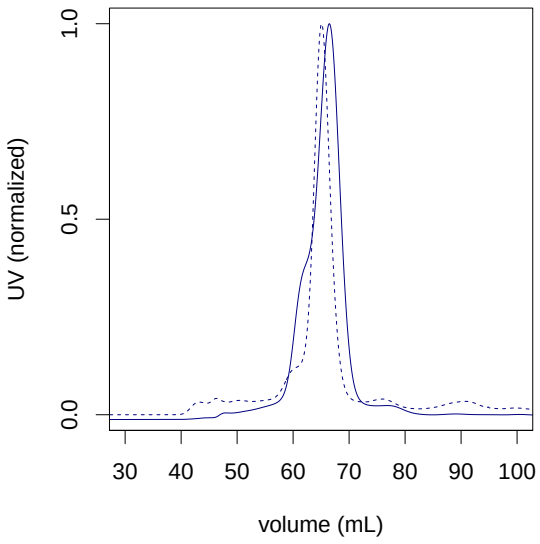

Figure 5.4: *Size exclusion chromatography of P1 (dashed line) and P2 (straight line) on a superdex 200 pg column. Within error, both samples elute at the same volume. The chromatogram is representative for three independent experiments from the same expression. Running buffer: 25 mM MES, pH 6.0; 150 mM NaCl; 5 % glycerol; 0.05 % DDM.*

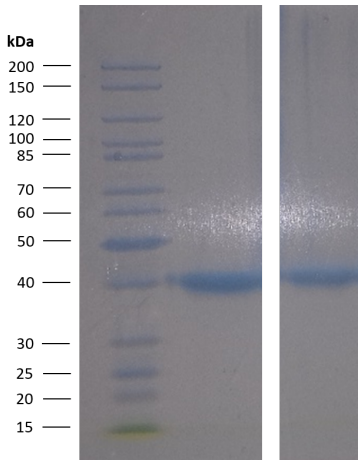

Figure 5.5: *Coomassie stained SDS-PAGE gel of samples P1 and P2 after purification with SEC. From left to right: M; P1; P2. In neither sample impurities are detectable on the gel. Both samples were run on the same gel.*

5.5 SEC-MALS

SEC-MALS is a valuable tool for assessing the quality of a (membrane) protein sample, because not only does it confirm a proteins purity, but also its homogeneity. For certain applications it is important to have a homogeneous sample, *i.e.* only one oligomeric state. Determining the oligomeric state of a membrane protein is not an easy task. The main issue is related to the circumstance that membrane proteins in solution are assembled in detergent micelles. The amount of detergent associated with a protein is generally not known and may vary considerably dependent on the specific protein [189]. The SEC-MALS technique approaches the problem by using size exclusion chromatography coupled to a combination of measurements of the solution refractive index, the absorbance at 280 nm and light scattering. The three detection methods together provide sufficient information to

calculate a weight averaged mass of the protein in the sample [190]. The purpose of SEC (in SEC-MALS) is to physically separate the different species in solution by their size. This is to ensure that only one species at a time is in the measuring chamber, which allows determining the molecular mass of the corresponding oligomeric state.

To get optimal data from SEC-MALS experiments it is required that micelles containing protein are well separated from empty micelles on the column. In SEC-MALS chromatograms, a micelle peak shows up because the concentration of micelles in the sample is always slightly different than in the equilibration buffer [190]. This difference is detected by the very sensitive measurements of refractive index and light scattering. Generally the best columns to meet this requirement are the WTC columns (Wyatt Technology), which have been specifically developed for SEC-MALS applications. It was found, however, that MntH2 sticks to the WTC columns and therefore SEC-MALS was performed on a superdex 200 10/300 column instead. The results for samples P1 and P2 are shown in fig. 5.6. Both chromatograms show a single, symmetrical peak in the UV, which indicates that the samples are pure and homogeneous. Despite this, it was not possible from the data to accurately calculate the molecular mass of MntH2. The analysis of the peaks is shown in fig. 5.7. The calculated molecular masses were 39 $\pm$ 0.5 kDa for P1 and 47 $\pm$ 0.3 kDa for P2. This is significantly below the expected mass of a monomer (61.4 kDa), which might be due to poor separation of

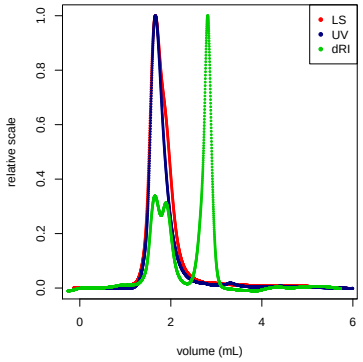

(a) *SEC-MALS run of P1 on a superdex 200 10/300 column.*

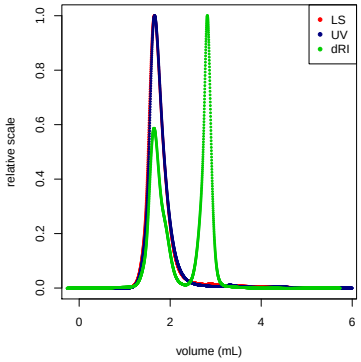

(b) *SEC-MALS run of P2 on a superdex 200 10/300 column.*

Figure 5.6: *SEC-MALS chromatograms of samples P1 and P2 purified by SEC. In the two chromatograms, the first peak represents the protein-detergent complex. In the light scattering (LS) and refractive index (dRI) data a second peak is seen on the right, which is overlapping with the first peak. This is the detergent peak. The large peak in the dRI at an elution volume between 2.5 and 3.0 mL is due to minor differences between the sample and running buffer.*

the protein- from the micelle peak. Overlapping of the micelle peak with the protein peak will lead to overestimation of the contribution of detergent in the protein-detergent complex and consequently the mass contribution from the protein will be underestimated. Regardless of this issue, the conclusion is that in DDM the protein is monomeric.

5.6 Purification in DMNG

Decyl maltose neopentyl glycol (DMNG) is a detergent which has been reported to have favorable properties for membrane protein stability [191]. In previous work, MntH2 has been found stable in DMNG [108] Here, it was examined whether purifying MntH2 in this detergent would be of advantage, in particular with respect to membrane protein crystallisation. Purification

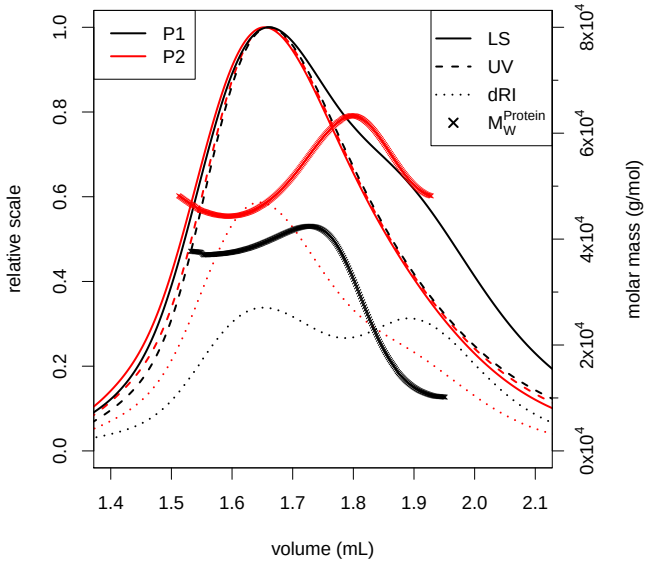

Figure 5.7: *Overlap of the peak region in fig. 5.6a and 5.6b. All data related to P1 is shown in black, whereas data for P2 is shown in red. A plot of the molecular weight vs elution volume is included (cross shaped points, which appear as a thick line). This plot has to be flat throughout the peak volume for it to be a reliable estimate of the molecular weight.*

in DMNG was performed as described in the previous section, but starting from the solubilisation of inner membranes, DDM was replaced by equivalent amounts of DMNG in buffers. For IMAC purification the second protocol was used (fig.5.2b), meaning that inner membranes were solubilised for two hours. Similarly to the purification in DDM, the protein eluted in two major peaks from the IMAC column (fig. 5.8). In line with previous purifications in DDM, these two peaks were run separately on the SEC. Surprisingly, in DMNG the elution volume between P1 and P2 was different and P2 eluted earlier than P1 (fig. 5.9). The purification in DMNG has been performed

only one single time and yields were 2.7 mg protein for P1 and 1.0 mg for P2, starting from the same amount of total protein as in purifications with DDM. The yield for P2 was low, because due to a technical problem sample was lost during SEC. The chromatogram in fig. 5.9 shows that a small

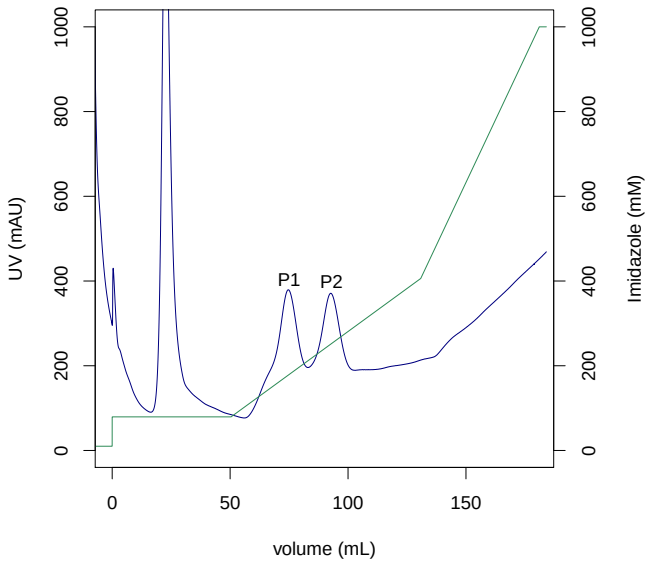

Figure 5.8: *IMAC purification of MntH2 in DMNG buffer. The experiment was performed analogous to purifications in DDM (fig. 5.2b) where inner membranes were solubilised for 2 h, but DDM was replaced by equivalent amounts of DMNG in buffers. MntH2 was eluted in two peaks (P1 and P2) during the first imidazole gradient, which were collected separately. Running buffer: 25 mM HEPES, pH 8.0; 300 mM NaCl; 10 % glycerol; 0.05 % DMNG.*

fraction of P1 eluted at the same volume than P2 and vice versa. This indicates that either P1 is in equilibrium with P2 or that the two peaks were not completely separated after IMAC purification.

P1 and P2 from the purification in DMNG were run in a SEC-MALS experiment (fig. 5.10). Compared to the previous run in DDM (fig. 5.6) the

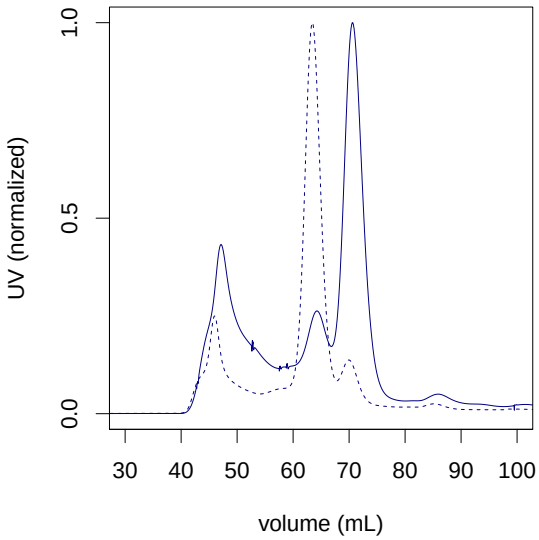

Figure 5.9: *Size exclusion chromatography of P1 and P2 on in DMNG buffer. The elution volumes differ for P1 (straight line) and P2 (dashed line) suggesting that P2 forms larger entities than P1. Running buffer: 25 mM MES, pH 6.0; 150 mM NaCl; 0.05 % DMNG.*

micelle peak is better separated from the protein peak. DMNG micelles are smaller in size than DDM micelles, which increases the difference in size between the protein-detergent complex and empty micelles. Better peak separation increases the accuracy of mathematical analysis to determine the oligomeric states (fig. 5.11). In fig. 5.11, the calculated molecular protein mass is constant over time, which is a clear improvement when compared to fig. 5.7. Nevertheless, the calculated molecular weights did not match exactly with the mass of MntH2 (61.4 kDa) or multiples thereof. Calculated masses were 67.5 kDa ± 0.5 kDa for P1 and 152.7 kDa ± 1.1 kDa for P2. This shows that P1 is monomeric. In case of P2 the interpretation is less

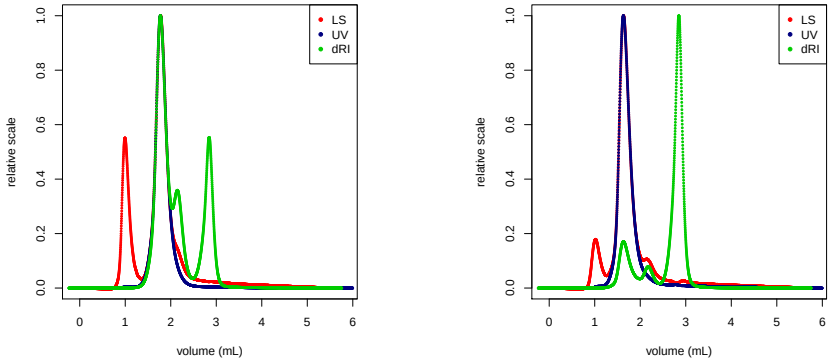

(a) *SEC-MALS run of P1 on a superdex 200 10/300 column.*

(b) *SEC-MALS run of P2 on a superdex 200 10/300 column.*

Figure 5.10: *SEC-MALS of P1 and P2 in DMNG buffer (25 mM MES, pH 6.0; 150 mM NaCl; 0.05 % DMNG) on a superdex 200 pg column. The protein peak is better separated from the micelle peak compared to previous runs in DDM buffer (fig. 5.6).*

obvious because the calculated average molecular mass is almost exactly 2.5 times the mass of an MntH2 monomer. One explanation is that purified MntH2 is bound to a natural binding partner, which could be a low molecular weight protein. An alternative explanation would be that MntH2 is complexing metal ions. A protein metal complex could affect the extinction coefficient of MntH2 at 280 nm, which would cause an error in the calculation of protein concentration.

As an side note, the SEC-MALS experiment in DMNG was performed two days after the protein was purified by SEC. The fact that P1 and P2 showed a different oligomeric state in this experiment therefore shows, that there is no noticeable equilibration between the two forms.

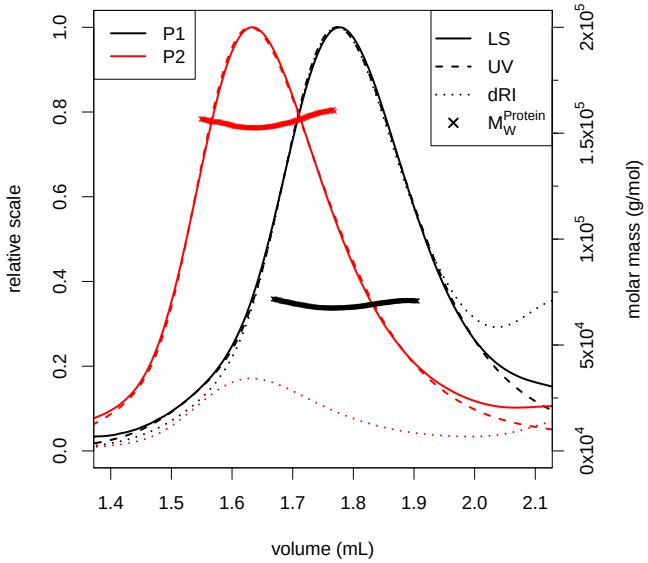

Figure 5.11: *Overlap of the peak region from SEC-MALS runs of P1 and P2 in DMNG buffer (25 mM MES, pH 6.0; 150 mM NaCl; 0.05 % DMNG). Analysis of peaks yields an averaged molecular weight of 67.5 ± 0.5 kDa for P1 and 152.7 ± 1.1 kDa for P2 (data shown in cross-shaped points). Compared to fig. 5.7 the calculated molecular weight is constant over the whole section of both peaks, which shows that the calculations were not influenced by an overlap of the micelle peak. Nevertheless, the calculated masses do not match well with the mass of MntH2 (61.4 kDa) or multiples thereof.*

5.6.1 Mass Spectrometry

In mass determination experiments of P1 and P2 in DMNG buffer by mass spectrometry, the exact molecular mass of both forms was determined. The experiments confirmed that P1 and P2 share the same mass of 61354 Da. (fig. 5.12). This matches almost exactly with the mass of the full MntH2 expression construct, which is 61359 Da. The additional peaks in the spectrum at 62303 Da correspond to protein with one bound detergent molecule. The experiments also conclusively show that the protein is pure and samples

are not contaminated by some protein binding partner of MntH2.

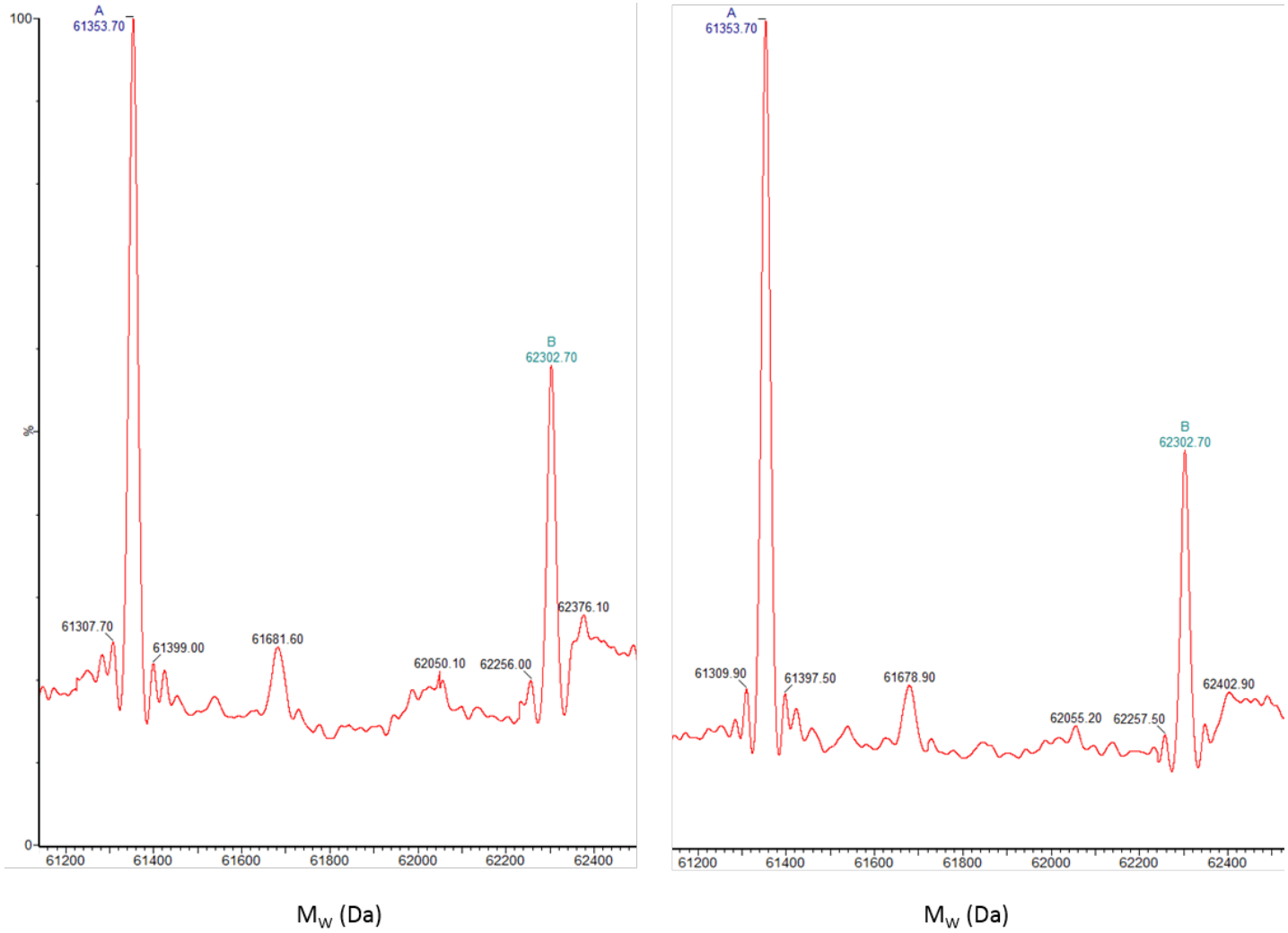

Figure 5.12: *Mass determination of P1 and P2 in DMNG buffer using mass spectrometry. The figure shows excerpts with the two main peaks of the spectra from P1 (left) and P2 (right). The major peak at 61353.70 kDa corresponds to the molecular weight of the MntH2 construct, which is 61359 Da. The peak at 62303 corresponds to protein with one bound detergent molecule (M_{DMNG} = 949.08 g/mol). The third peak at 63252 (protein with two detergent molecules) is not shown.*

5.6.2 Overexpression and purification of HRV-3C protease

HRV-3C protease was purified to get his-tag cleaved MntH2. Overexpression of HRV-3C protease is performed similarly to MntH2 with details specified in section 3.12. Cell growth for overexpression was performed at a reduced temperature of 30 °C because otherwise the majority of the protein ended up in the insoluble fraction after cell disruption. HRV-3C was purified using IMAC chromatography in a linear gradient of imidazole. Fractions from the run were analysed using coomassie stain (fig. 5.13) and western blot (not shown). Fractions containing the protein were pooled and subjected to dialysis overnight. Before storage the protein is concentrated to 5 mg/mL followed by addition of glycerol to a concentration of 50 %. Samples are frozen in liquid N_2 and stored at -80 °C. The yield was 119 mg of protein for 4 L of growth culture as estimated by a BCA assay.

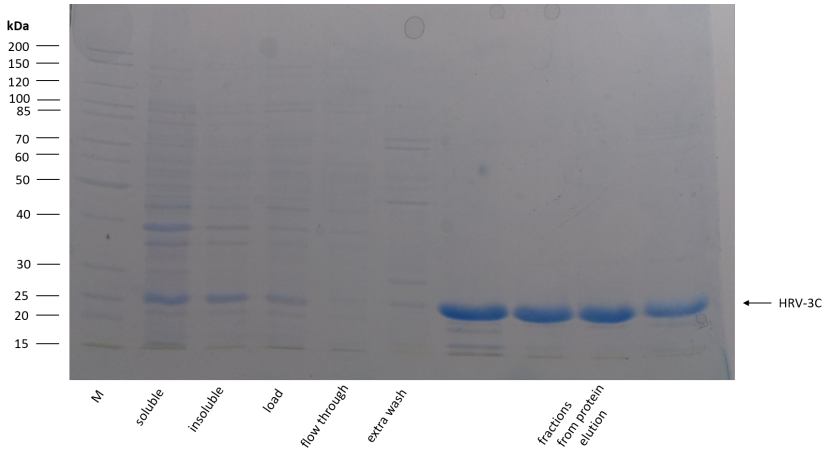

Figure 5.13: *IMAC purification of HRV-3C protease. Samples were subjected to SDS-PAGE and stained with instant blue^{TM}. The amount of sample was 0.5 µL/lane for lane 1-5, 15 µL for lane 6 and 9 and 5 µL for lane 7-8. The first two lanes were taken from the soluble and insoluble fractions after cell disruption.*

5.6.3 Cleavage of the MntH2 his-tag

Performance of MntH2 cleavage was tested at different ratios (w/w) of MntH2:HRV-3C (1:2, 1:5, 1:10) and samples were left for cleavage for 6 and 24 h. This experiment was performed both at room temperature and at 4 °C. Western blot analysis showed that under all conditions a high percentage of MntH2 was cleaved (fig. 5.14). To obtain larger amounts of

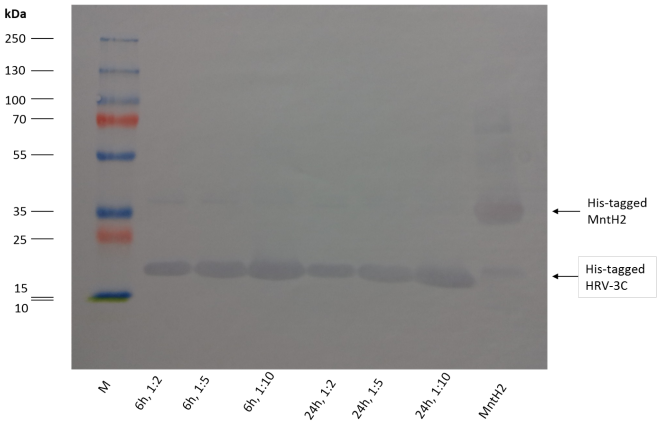

Figure 5.14: *Western blot analysis of MntH2 cleavage by his-tagged HRV-3C protease. Cleavage was performed in different ratios of MntH2:protease, as labelled in the figure, and reactions were stopped after 6 h or after 24 h. The band on the very right shows the control where uncleaved MntH2 was added that has not been subjected to protease. For each lane, the total amount of loaded MntH2 was 11 µg. The results shown are from an experiment conducted at room temperature but the outcome was not affected by when the experiment was performed at 4 °C. The blot was stained with HRP-conjugated anti-his_6 antibody.*

cleaved MntH2, the protein was purified as described before using IMAC chromatography (fig. 5.2b). After elution, MntH2 was concentrated to 1 mg/mL with a spin-concentrator (30 kDa) and incubated with HRV in a ratio of 1:2 (w/w). was added in a ratio of 1:2. For cleavage the sample was left in dialysis buffer (25 mM HEPES, pH 8.0; 300 mM NaCl; 10 mM

imidazole; 10 % glycerol; 0.05 % DDM) for 6 - 24 h at 4 °C. After cleavage was complete, as confirmed by western blot analysis, a reverse IMAC purification was performed. As MntH2 purification, the reverse purification was performed on a Ni-NTA column using an imidazole gradient. Cleaved

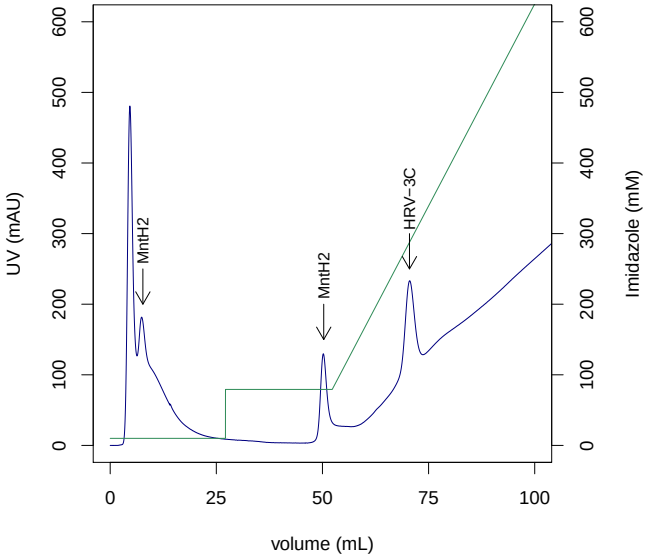

Figure 5.15: *Reverse purification of His-tag cleaved MntH2. Cleaved MntH2 elutes from the column right at the start (arrow). Even before that a large amount of a low molecular weight protein is eluted, which likely is a degradation product of MntH2. Of the two remaining peaks in the chromatogram the first one represents cleaved MntH2 as well and the second one correspond to HRV-3C protease.*

MntH2 elutes right at the start of the run, as without His-tag MntH2 has no high affinity towards Ni^{2+}. The cleaved MntH2 from this run is contaminated by a low molecular weight impurity as seen in coomassie stained SDS-PAGE gels (fig. 5.16). The impurity elutes even before MntH2 but complete separation cannot be achieved. It is possible that this contam-

inant is a degradation product of MntH2. Two more peaks are observed in the chromatogram at higher elution volumes. Analysis (western blot & coomassie stain) of these peaks revealed that the first peak corresponds to cleaved MntH2 as well (not shown). Probably this protein was uncleaved when it was loaded onto the column, and was cleaved while on the column by HRV-3C. It is unclear, however, why given this explanation, this protein would elute at exactly this position in the chromatogram in such a sharp peak. The third peak shows HRV-3C protease. The final yield was ca. 4 mg starting from inner membrane samples with ∼240 mg total protein.

The obtained yield was not optimal and could be potentially significantly improved by amending the protocol. It was observed that there was significant aggregation of protein during the cleavage step in dialysis buffer. In addition there are losses connected to each time the protein is purified with IMAC. To limit these losses it one could try to cleave MntH2 directly when it is bound to the column during IMAC purification.

5.7 CPM assay

The CPM assay is a relatively new method to assess the (thermal) stability of (membrane)-proteins and an alternative to circular dichroism (CD) spectroscopy [192]. It was performed here to test whether purified MntH2 is folded, but also to measure thermal melting curves of MntH2 in different solutions and in the presence of transition metals. The assay makes use of the dye 7-Diethylamino-3-(4'-Maleimidylphenyl)-4-Methylcoumarin (CPM),

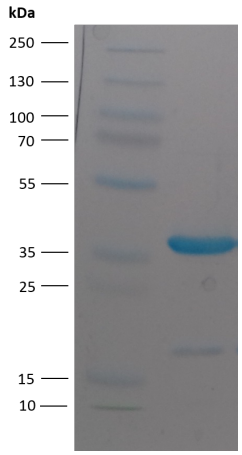

Figure 5.16: *Coomassie stained gel of cleaved MntH2 after reverse purification. The low molecular weight contaminant at ca. 18 kDa probably represents a degradation product of MntH2.*

which reacts with cysteine residues. In solution this dye is non-fluorescent, but after reaction with the thiol group of a cysteine, it starts emitting light at 463 nm (excitation ∼387 nm). Cysteines, buried in the hydrophobic core of the protein do not react with CPM. However, if the protein denatures, the originally buried cysteine becomes exposed to the bulk solution and after reacting with CPM, this will lead to an increase in fluorescence. Naturally, this method requires for the protein to contain one or more buried cysteines. In addition, cysteines on the surface of the protein will interfere with the assay, as in that case CPM can react with folded protein. For MntH2, which has only one cysteine in its sequence, tests showed that the assay works very well.

In a first set of conditions the stability of MntH2 was tested at different pHs. All buffers contained 30 mM MES, 30 mM HEPES, 30 mM CHES, 150 mM

NaCl and 0.05 % DDM, which covered the whole range of pHs investigated (6.0 - 9.0). Varying concentrations of glycerol (0 % and 5 %) and magnesium (0 mM, 2 mM, 10 mM) were also tested. The influence of these two compound on protein stability was of interest because glycerol is added to buffers during protein purification while magnesium, as will be shown later, is required in SURFE^{2}R experiments. The result of the assay is shown in fig. 5.17. The figure shows the first derivatives of the melting curves, the peaks of which correspond to the different melting temperatures. The assay revealed that of the tested factors, the pH had the largest impact on MntH2 stability. Melting temperatures ranged from 57.9 - 59.6 °C at pH 6.0 to 42.1 - 45.6 °C at pH 9.0. MntH2 was previously found to be most stable at pH 5.5 in an assay using light scattering [193]. The presence of 5 % glycerol has a minor stabilising effect at lower pH (pH 6.0 and 7.0) but no effect at pH $>$ 7.0. Finally, the presence of magnesium did not appear to influence melting curves.

The dependence of MntH2 stability on salt (K^+) concentration was also determined because potassium was used in transport experiments with valinomycin (chapter 6). Two of the conditions in this assay contained 2 mM EDTA. This was done in case MntH2 remain bound to a metal during purification. The results of the second assay are shown in fig. 5.18. It is revealed that in all conditions the protein has a very similar stability. Neither the salt concentration nor the presence of EDTA induces a shift of the melting

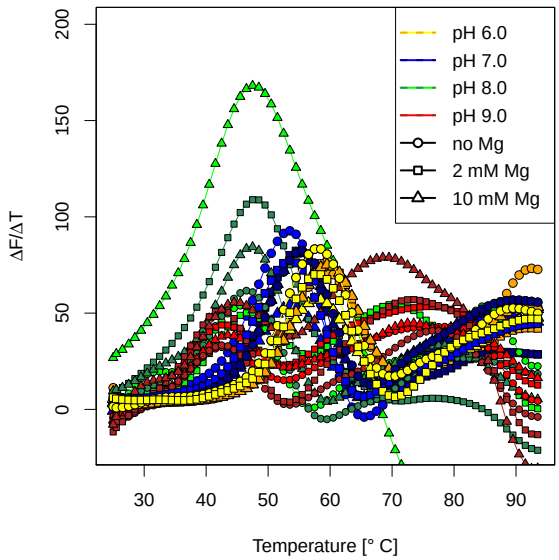

Figure 5.17: *CPM assay on MntH2. The buffer conditions varied in this assay included pH (6.0, 7.0, 8.0, 9.0), glycerol (0 %, 5 %) and magnesium (0 mM, 5 mM, 10 mM). The base buffer was 30 mM MES, 30 mM HEPES, 30 mM CHES and 150 mM NaCl. The figure shows the derivatives of the different melting curves which have been smoothened in OriginPro using fast Fourier transformation. The data shows that of the tested parameters, the pH had the largest impact. Curves from conditions with the same pH have been drawn in two different, but similar, colours as indicated in the figure legend. The darker of the two colours represent the conditions where 5 % glycerol was present. The different magnesium concentrations are indicated by the plot symbols of the data points. The assay was performed with a concentration of 0.05 mg/mL protein.*

point.

A third CPM assay was designed with the goal to optimise the buffer used for reconstitution. Different detergents were added in a concentration of 1 %. It was examined if different concentrations of glycerol (5 % or 10 %) may support protein stability during reconstitution. The base buffer for this experiment was 20 mM MES/HEPES/CHES, pH 7.0 and 150 mM KCl. The assay showed that OGP has an effect that is detrimental to MntH2 stability

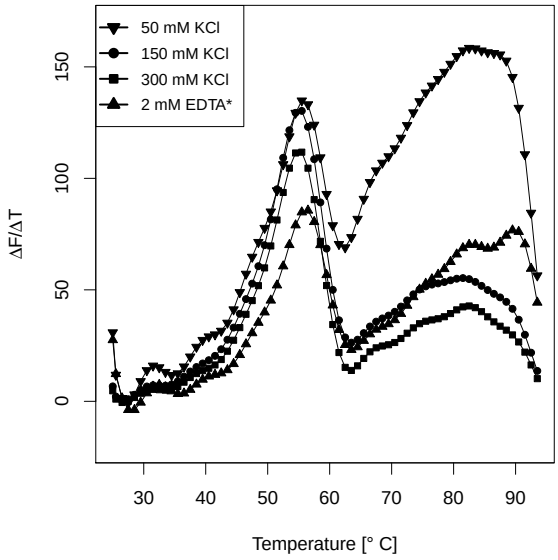

Figure 5.18: *CPM assay on MntH2 with varied K^+-salt concentrations. The buffer was 5 mM MOPS at pH 7.0 and salt concentrations were as shown in the figure legend. The figure shows the derivatives of the different melting curves smoothened by fast Fourier transformation (OriginPro). The stability did not greatly vary between the different conditions. Each dataset represents the average of three measurements on the same plate. *In the EDTA sample the salt concentrations was 150 mM KCl.*

(fig. 5.19). Stability is improved in Triton X-100 but clearly is highest in DDM. Raising DDM from 0.05 % to 1 % does not influence thermostability (compare fig. 5.19 to fig. 5.17). Glycerol does have some stabilising effect, but it is minor. Glycerol was therefore left out from the reconstitution buffer.

In the final assay, it was investigated whether the presence of transition metal ions (i.e. possible substrates) would have any effect on the stability (fig. 5.20). If a metal substrate binds to its binding pocket, it is likely to induce a shift in the melting point. In the assay two metal ions, Mn^{2+} and

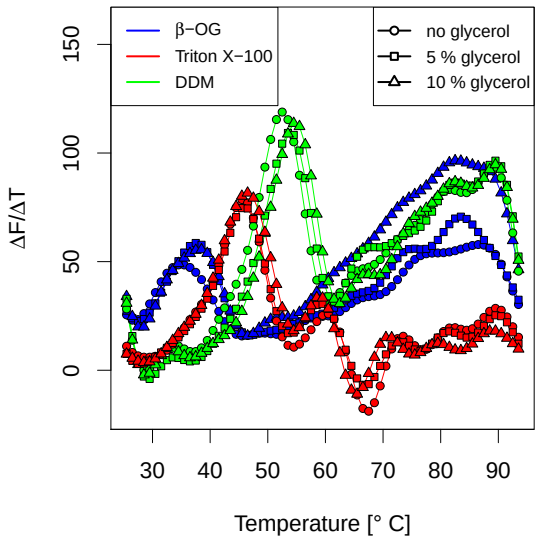

Figure 5.19: *CPM assay on MntH2 using different detergents. All detergents were used in a concentration of 1 % in base buffer (20 mM MES/HEPES/CHES, pH 7.0; 150 mM KCl). Glycerol concentrations were varied as specified in the right figure legend. The melting temperature was clearly mostly affected by the nature of the detergent. Including the variability in glycerol concentrations, melting temperatures were 34.9 - 37.7 °C for OGP, 45.2 - 46.1 °C for Triton X-100 and 52.4 - 54.6 °C for DDM. For each set of conditions in different detergents, the highest melting temperatures were found in the probes with 10 % glycerol.*

Ni^{2+}, were tested at low (1 μM) and high (100 μM) concentrations. This was done at pH 6.0 as well as at pH 8.0, as binding might be affected by the pH. The results show that neither metal appears to have a significant effect on protein stability: Under all conditions tested, the melting point is stable compared to the samples without metals, although at 100 μM Ni, pH 8.0, there appears to be a second peak at higher temperature. This may indicate that in this sample the protein is distributed between two states, but this possibility has not been further investigated.

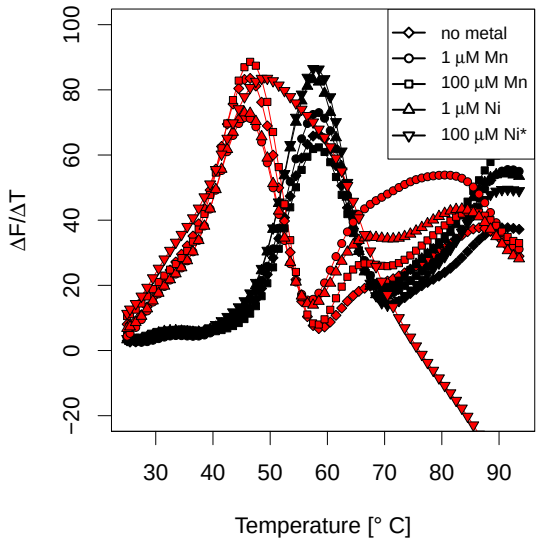

Figure 5.20: *CPM assay testing the effect of metal binding at pH 6.0 (black) and pH 8.0 (red). At neither pH the addition of Mn^{2+} or Ni^{2+} at the given concentration significantly affected the melting temperature. An exception appears to be the condition of 100µM Ni^{2+} at pH 8.0. The melting curve of this sample was 49.1 ± 0.5 °C compared to 45.7 ± 0.7 °C measured for the metal free condition. However, in a successive assay this difference was not confirmed (see text). *For visual reasons this data has been scaled down to match amplitudes with the data for the metal free condition.*

5.8 Tryptophan fluorescence

Due to their aromaticity, tryptophan residues are a natural fluorescent label in protein with an excitation wavelength of 280 nm. The fluorescence intensity of tryptophan residues in proteins is strongly dependent on their environment (polarity/solvent accessibility) in the protein. Conformational changes of the protein, that alter the environment of a tryptophan residue can therefore be detected as a change in the fluorescencent signal. This may be a shift in the emission wavelength or a decrease/increase in fluorescence

intensity. In MntH2 there is a tryptophan residue, W65, that is right next to N64, which is part of the conserved metal binding pocket. Therefore it was possible that metal binding to the protein could be detected via the fluorescence of this tryptophan. However, no change in tryptophan fluorescence was observed when Ni^{2+} or Mn^{2+} in concentrations of up to 100 μM were added to MntH2. For Cu^{2+} this assay turned out to be not compatible, because in experiments with bovine serum albumin (BSA) Cu^{2+} induced strong non-specific fluorescence quenching at a concentration of 10 μM.

5.9 Discussion

Even though MntH2 has been purified before this work, the data presented here shows some interesting new insights. Starting from IMAC chromatography, when comparing the two purifications represented in fig. 5.2, a much higher yield was obtained, when the solubilisation time of inner membranes was increased. In the first purification a yield of 4-4.6 mg (from ∼600 mg total protein) and in the second purification a total yield of 19 mg (from ∼240 mg total protein) was obtained. Even though the yields are not directly comparable, because the purifications were from different expressions, this strongly suggests that increasing the solubilisation time leads to improved yields. It appeared that MntH2 obtained from protocol two was somewhat less pure than when purified according to protocol one. These impurities, however, can be removed by SEC, which yields highly pure protein as confirmed by SDS-PAGE, SEC-MALS and mass spectrometry.

In IMAC purifications following protocol two, MntH2 eluted from the column in two or even three peaks (P1, P2 and P3). It was expected that these peaks would represent different oligomeric states of MntH2. However, SEC-MALS data (even though calculated molecular weights were not accurate) clearly showed that protein from both peaks is monomeric when MntH2 was solubilised in DDM. That there is a difference between P1 and P2 only shows when MntH2 is solubilised in DMNG, when SEC-MALS data show that P2 is multimeric. Because mass spectrometry data show that P1 and two P2 share the same molecular mass it remains unclear what distinguishes the two forms. Possibly they represent two different states of the protein.

MntH2 was successfully cleaved from its his-tag using HRV-3C protease. An excess ratio of 2:1 (w/w) protease was enough to cleave more than 80 % of MntH2 within 6 h. Protease was removed by reverse purification on a Ni-NTA column. The final yield of 4 mg cleaved MntH2 was good, but it could be further improved. A protocol, where MntH2 is cleaved directly when bound to the Ni-NTA column, should lead to increased yields, because it reduces the amount of required steps.

The CPM assay showed that purified MntH2 was folded and stable in a wide range of conditions. Binding of metal ions to the protein could not be observed, neither in the CPM nor in the tryptophan fluorescence assay. In both cases this could be either because the assay is not sensitive enough or because in detergent micelles the protein adopts a conformation that does

not bind metals. The latter seems plausible, given that the SLC11 homologue EcoDMT was crystallised in a structure that did not bind any metal ions [123].

5.9.1 Conclusions

For future purifications of MntH2 I suggest to use the second purification protocol using a combination of IMAC and SEC. This protocol yields highly pure protein and the final yield of ca. 4-5 mg (P1 and P2 combined) from 250 mg total protein is very good for a membrane protein. Data from mass spectrometry, SEC-MALS and CPM assays show that the protein is intact, monodisperse and thermally stable under various conditions. These are promising characteristics to perform functional and structural studies on MntH2, which are presented in the following two chapters.

Chapter 6

Biophysical characterisation of *Enterococcus faecalis* MntH2

This chapter deals with the biophysical characterisation of the transition metal transporter *Enterococcus faecalis* MntH2. MntH2 is a homologue of the SLC11 (Nramp) family and as such it is hypothesised to be a high-affinity metal-uptake protein. This property makes it contribute to bacterial virulence for reasons that have been explained in section 1.7. MntH2 was chosen as a model protein, to demonstrate the applicability of the SURFE^{2}R technique to investigate transition metal transport. The procedure, that led to the selection of MntH2, is presented in section 6.1 followed by an in depth characterisation of metal transport by MntH2.

6.1 Selecting a suitable transition metal transporter

To investigate if transition metal transporters can be biophysically characterised with the SURFE^{2}R, a protein had been found that would be suitable for that task. A library of proteins was available that has been created by the Steve Baldwin group in Leeds as part of the MPSIL (Membrane Protein Structure Initiative Leeds) project. From this library six transition metal transporters were chosen from three distinct families (table 6.1). CDF (cation diffusion facilitator) transporters are a family of Me^{2+}/H^+ antiporters with Zn^{2+} and other transition metal ions as substrates [177, 194]. ZIP (Zrt/Irt-like Protein) transporters are involved in uptake of Zn^{2+} and Fe^{2+} [195, 196]. As mentioned, Nramp homologues (MntH2) are supposed to be responsible for H^+-coupled transition metal uptake with a broad substrate specificity, but with Mn^{2+} being one of the main substrates [135, 147].

The expression protocol for all constructs has been established in previous work [108, 197] and was performed as described in section 3.10. Because expression of the different constructs was performed on a small scale (50 mL), inner membranes were purified by water lysis (section 3.13.2). All constructs had a his-tag attached and expression was confirmed by Western blotting of inner membrane samples (fig. 6.1). Five of the six proteins showed up as a signal in the western blot. Three constructs showed acceptable expression levels, migrated in SDS-PAGE as a single band and were chosen for further

MPSIL code	Family	Organism
63A	CDF (SLC30)	*Escherichia coli* K12
67E	CDF (SLC30)	*Corynebacterium diphtheriae* NCTC 13129
294CVH	Nramp (SLC11)	*Enerococcus faecalis* V853
295G	Nramp (SLC11)	*Escherichia coli* K12
414MBP	ZIP (SLC39)	*Desulfovibrio vulgaris* subsp. vulgaris str. Hildenborough
600DAT	ZIP (SLC39)	*Achromobacter xylosoxidans*

Table 6.1: *Table of the expression constructs of transition metal transporters examined. Enterococcus faecalis MntH2 is encoded by the combination 294CVH. CDF: Cation Diffusion Facilitator family; Nramp: Natural resistance associated macrophage protein family; ZIP: Zrt/Irt-like Protein family.*

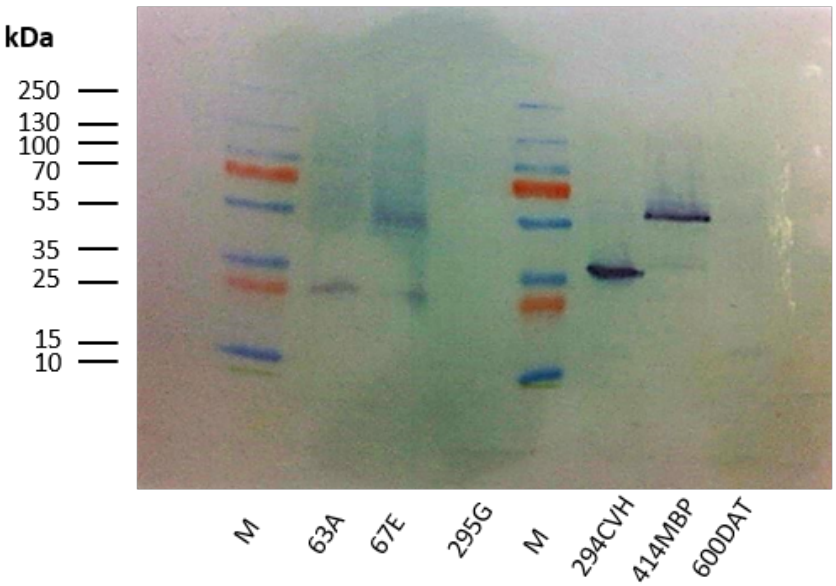

Figure 6.1: *Western blot on inner membranes containing transition metal transporters. All constructs were stained using HRP conjugated anti-his$_6$ antibody. Overexpression was performed in E. coli BL21* (DE3) harbouring the plasmid pRARE2 using autoinducing medium.*

study.

6.1.1 SURFE^{2}R experiments using bacterial inner membranes

SURFE^{2}R experiments were performed using bacterial inner membrane extracts containing the constructs 63A, 294CVH and 414MBP. The inner membranes were not applied in pure form to the sensors, but instead a special sensor preparation protocol was applied. Bacterial inner membranes extracts containing transport protein, have not been tested successfully in the past in SURFE^{2}R experiments. The reason for this is unconfirmed, but might be related to outer membrane fragments in the sample that may hinder the adsorption of the inner membrane to the surface. The protocol applied here dilutes inner membrane exctracts with "pure" lipids and has been established for the nucleoside transporter NupC [198]. When inner membrane vesicles containing NupC were mixed with liposomes by tip-sonication, uptake signals due to NupC could be observed in SURFE^{2}R experiments. Here, inner membranes containing transition metal transporters were treated as described in section 3.21.1.

To screen for a signal, the transition metal ions Mn^{2+}, Zn^{2+} and Co^{2+} were tested as a substrate for the three transporters. The signal obtained with 63A and 414MBP was very small, or absent, but a signal was observed for the construct 294CVH (fig. 6.2). Besides testing different substrates, the signal was recorded at varying buffer pH and compared to signals from control experiments, set up using samples from inner membranes of *E. coli* BL21*

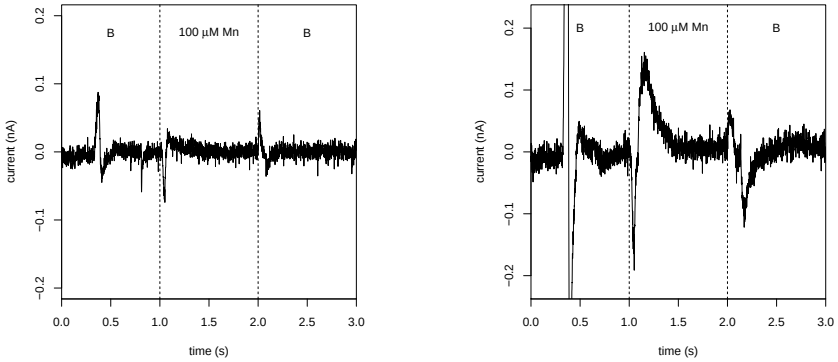

(a) *Control with mixed inner membranes from E. coli BL21*.*

(b) *Mixed inner membrane sample with MntH2 (294CVH)*

Figure 6.2: *SURFE^{2}R experiments on mixed inner membrane samples. The difference of the MntH2 sample to the control is significant, but the amplitude of ca. 150 pA is too low for biophysical characterisation using SURFE^{2}R experiments.*

bacteria (fig. 6.3). Importantly, the signal-to-noise was too low to conduct experiments for biophysical characterisation. To improve signal amplitudes, samples of purified MntH2 (294CVH) reconstituted in proteoliposomes were tested.

6.2 Reconstitution of MntH2

As with expression and purification, a protocol for reconstitution of MntH2 has been described previously [154]. The original method starts by dissolving lipids to a micellar suspension by adding OGP in a sufficiently high amount (see section 3.17.1 for details). The membrane protein in detergent solution is added to that mixture and proteoliposomes are generated by slowly removing the detergent by adding hydrophobic polystyrene beads (bio-beads) that absorb the detergent.

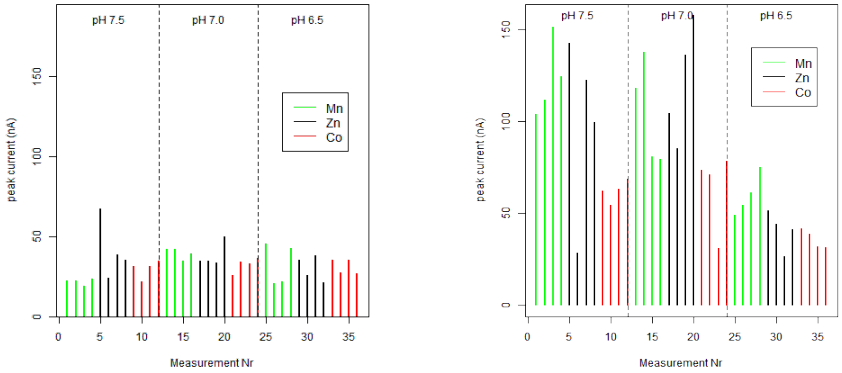

(a) *Control with mixed inner membranes from E. coli BL21*.*

(b) *Mixed inner membrane sample with MntH2 (294CVH)*

Figure 6.3: *Peak amplitudes of SURFE^{2}R experiments with varying conditions on mixed inner membrane samples. Of the four repeats of each condition, the first two were performed with 50 μM- and the other two with 100 μM substrate.*

The protocol for MntH2 reconstitution was optimised during the course of the project. Modifications were made after a protein stability assay (CPM assay, section 5.7, fig. 5.19) showed that OGP destabilises MntH2 compared to other detergents, such as Triton X-100 and DDM. To minimise potential loss of protein, DDM was used as DDM is the detergent in which the protein was most stable. Reconstitutions in DDM, or other detergents with a low CMC, are slightly more complicated than reconstitutions in OGP, which has a relatively high CMC. In a publication on the reconstitution of ABC-transporters in Triton X-100, Geertsma et al. [184] give their suggestions of general guidelines to establish a reconstitution protocol in a low CMC detergent. These suggestions have been followed here. Unilamellar liposomes are prepared by extrusion and saturated with detergent (or slightly oversaturated). An important parameter to determine is the right concentration of

detergent to use. The saturating concentration is determined by titrating a concentrated detergent solution to the proteoliposomes and monitoring the OD_{540}. The concentration at which the OD_{540} reaches its maximum should be the saturating concentration. This experiment has been done here using liposomes (200 nm) of *E. coli* 'polar' lipids and titrating DDM in steps of 0.05 - 0.1 %. Contrary to expectations, the graph showed no maximum and therefore no saturating concentration could be determined (fig. 6.4). Because the titration experiment did not inform on a suitable DDM con-

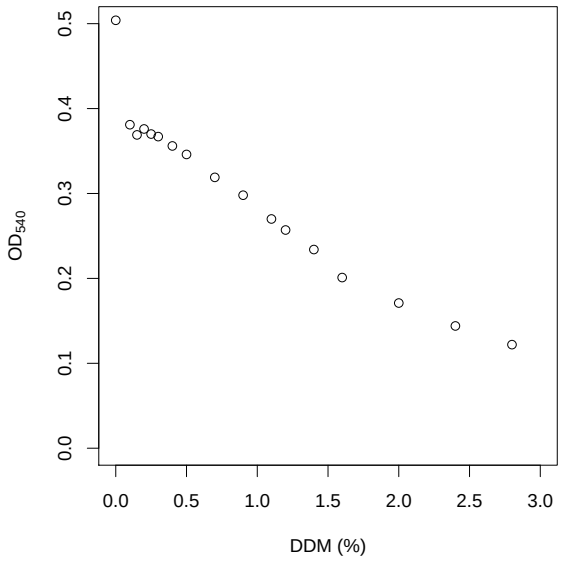

Figure 6.4: *DDM titration of liposomes from E. coli polar lipids prepared by extrusion (200 nm). After each titration step the sample was left to equilibrate for at least 1 min. With increasing concentrations of DDM the OD at 540 nm steadily decreased and no maximum was observed. Therefore a saturation radius could not be determined.*

centration to use, three reconstitutions were performed in parallel, using

different DDM starting concentrations of 0.2 %, 0.5 % and 1 % DDM. To determine which concentration works best, samples of the three reconstitutions were tested in SURFE^{2}R experiments. The reconstitution which has 1 % DDM, showed a significantly larger current than the other two samples. Consequently, all reconstitutions were performed with 1 % DDM and results shown in this thesis have been obtained from proteoliposome samples following the DDM reconstitution, unless specified otherwise.

6.3 SURFE^{2}R experiments on MntH2

6.3.1 Background Signals

In experiments with the SURFE^{2}R care has to be given to background signals due to solution exchanges on the sensor surface. The redistribution of charges on the SSM leads to a capacitive current response. This solution exchange artefact is usually not a great concern when uncharged substrates are used that do not interact with the SSM. In contrast, the problem becomes more severe with transition metals, as these carry a twofold positive charge and metals can interact with the polar phospholipid head groups of the SSM. This may lead to serious background signals. A strategy to reduce these artefacts is to "saturate" the SSM with Mg^{2+} ions. Mg^{2+} ions can prevent transition metal ions from binding non specifically to the phospholipids. To experimentally test the effect of Mg^{2+} ions, a control sensor (liposomes from *E. coli* polar lipids) was prepared and the amplitude of the solution exchange artefact of 1 mM Ca^{2+} was measured as a function of

Mg^{2+} concentration in the buffer (fig. 6.5). Without any Mg^{2+}, the am-

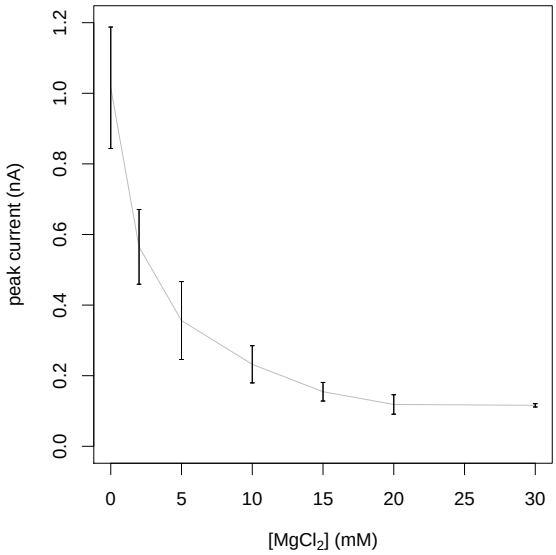

Figure 6.5: *Solution exchange artefact from Ca^{2+} ions in SURFE^{2}R experiments. The figure shows the amplitude of the solution exchange artefact of 1 mM Ca^{2+} on a control sensor with liposomes from E. coli polar lipid extract as a function of Mg^{2+} concentration in the buffer. The components of the base buffer were 25 mM Tris, pH 8.0 and 150 mM NaCl.*

plitude of the artefacts was high with a maximum current of more than 1 nA. 2 mM Mg^{2+} already reduced the amplitude to almost 50 %. Adding more Mg^{2+} further reduced the amplitude up to a concentration of 20 mM, after which no further decrease was observed. However, sensors with $\geqslant$ 10 mM Mg^{2+} appeared to have a shorter lifetime than sensors with only 2 mM Mg^{2+}, so it was decided to use 2 mM Mg^{2+} as the working concentration in all buffers.

6.3.2 The valinomycin control experiment

A problem concerning SURFE^{2}R experiments is that the background varies for each individual sensor and cannot always be accurately determined from experiments with control liposomes. One way to determine background would be to add an inhibitor to the sensor, completely stopping protein activity. A second way to eliminate the protein specific signal was developed here and comprises the use of valinomycin. When valinomycin is added to a sensor containing K^+ ions, the activity of the valinomycin transporting K^+ ions down the electrical potential gradient will cancel the electrometric signal from the protein. This is shown in fig. 6.6 for the example of the nucleoside/H^+ symporter NupC. Cancellation of the electrometric signal will occur if K^+ transport activity is faster than transporter activity (e.g. from NupC or MntH2). It was observed that 1 μM valinomycin in 150 mM KCl is able to fully cancel transport signal in the order of 1 nA.

6.4 SURFE^{2}R experiments with MntH2 proteoliposomes

Before activity of MntH2 in proteoliposomes was measured on the SURFE^{2}R, it was known that proteins of this family have been found to be most active at pH 5.5-6.0 ([142], [199]). It was also known that the protein has been reported to be most stable at pH 5.5 [193] and fluorescence experiments measuring Zn^{2+} transport in stopped-flow experiments were obtained at pH

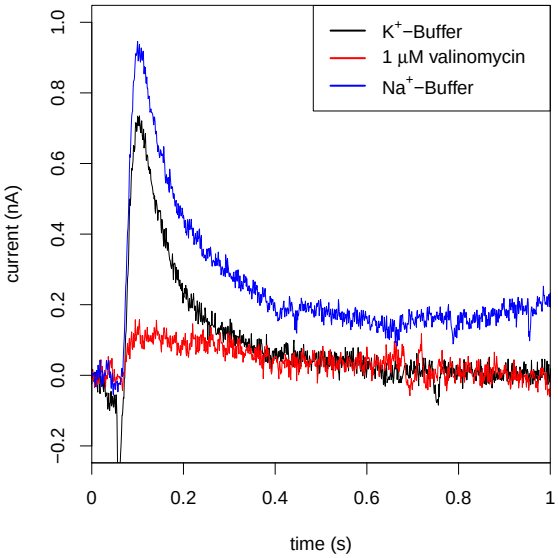

Figure 6.6: *Effect of valinomycin on NupC currents in SURFE^{2}R experiments. In buffer containing 150 mM KCl the presence of 1 µM valinomycin leads to almost complete inhibition of the NupC current, even though NupC does not transport potassium (red trace). Evidently, any potential gradient built up from NupC H^+ symport is immediately dissipated by counter transport of K^+ by valinomycin. When KCl is replaced by NaCl in the buffer, the signal reappears, confirming that valinomycin does not interfere otherwise with NupC activity.*

6.8 [154]. Therefore it was surprising that when activity of MntH2 was tested as a function of pH, highest activity was observed at pH $\geq$ 7.5. The conditions under which the most "robust" signal is obtained was at pH 8.0 with an activating buffer containing 100 μM Mn^{2+} (fig. 6.7). For prolonged experiments it is not advisable to measure MntH2 currents at pH $\geq$ 8.0 because the stability of the protein decreases at high pH (fig. 5.17). PH dependencies of the signal are shown in fig. 6.8a for uncleaved MntH2 and in fig. 6.8b for MntH2 where the his-tag was cleaved (section 5.6.3). Both pH profiles in fig. 6.8 look similar, indicating that the pH dependency of the

signal is not influenced by the his-tag. Before each experiment at different pH, the sensor was rinsed with 1 mL buffer, followed by a waiting time of 900 s. This was to make sure, that the buffer pH between in- and outside of the proteoliposomes on the sensor surface was equilibrated before the start of the experiment. The waiting time in between experiments at the same pH was 300 s. The experimental sequence was performed in two directions, that is from low to high pH and vice versa (fig. 6.8a). At pH 6.0 almost no signal is seen and the amplitude increases with increasing pH.

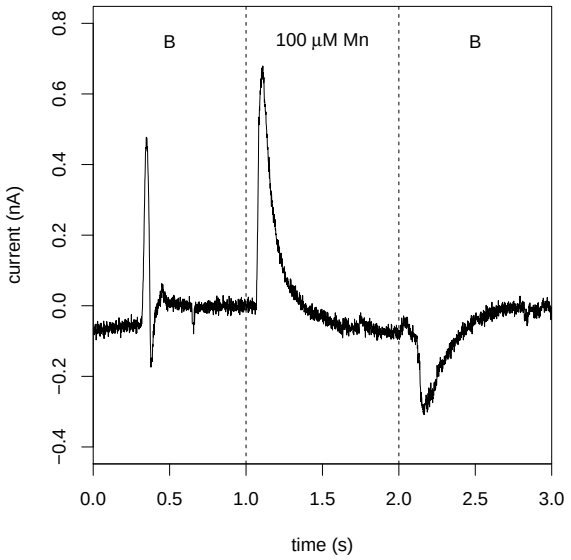

Figure 6.7: *SURFE^{2}R measurement of reconstituted MntH2 (LPR 1:10; uncleaved) activated by 100 µM Mn^{2+} at pH 8.0. These conditions were used as a standard for experiments with MntH2. Buffer: 10 mM MES/HEPES/CHES, pH 8.0; 140 mM KCl; 2 mM $MgCl_2$. A after two seconds results in a peak in the opposite direction due to reverse transport of the substrate. The trace is representative for experiments from three biological replicates.*

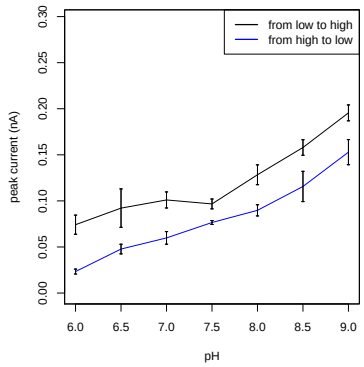

(a) *PH profile for uncleaved MntH2. The sample used in this experiment was reconstituted in OGP. Buffer: 10 mM MES/HEPES/CHES with 140 mM NaCl and 10 mM $MgCl_2$.*

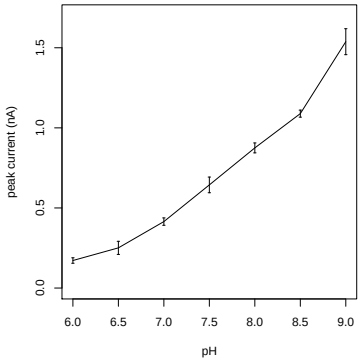

(b) *pH profile for his-tag cleaved MntH2. Currents represented in this figure were corrected for background, as determined by valinomycin (6.3.2). Buffer: 5 mM MES/HEPES/CHES; 150 mM KCl; 2 mM $MgCl_2$.*

Figure 6.8: *pH dependency of Mn^{2+}-currents for uncleaved and cleaved MntH2. Both profiles look similar. In fig. 6.8a the experiment was performed in both directions (started at low pH and moving to high pH and vice versa) to eliminate the possibility of a bias due to the sequence in which buffer pHs are changed. Errorbars are representative of four measurements on the same sensor.*

6.4.1 Experiment with different LPRs

Here, the effect of different lipid to protein ratios (LPRs) is tested. The idea of the experiment is to prove that the observed signal is due to ion transport: In case of transport the signal is expected to be broadened with a decreasing LPR as at a low LPR, substrate uptake should be slower. This leads to lower currents and an increased decay time of the signal. In practice, this has been shown to hold true for LacY, where proteoliposomes with LPRs of 1:5 and 1:10 were used to demonstrate lactose transport [200]. For electrogenic events other than transport (conformational change or electrogenic substrate binding), the decay time is expected to be independent of

the LPR.

MntH2 was reconstituted at LPRs of 1:5, 1:10 and 1:20. A BCA assay was performed to confirm that the LPRs after reconstitution are as expected. LPRs of 1:5, 1:11 and 1:20 were determined, assuming no lipids were lost during reconstitution. In SURFE^{2}R experiments all samples produced a similar signal. Neither the amplitude, nor the decay time of the signal varied greatly between sensors (fig. 6.9). This behaviour is atypical, because

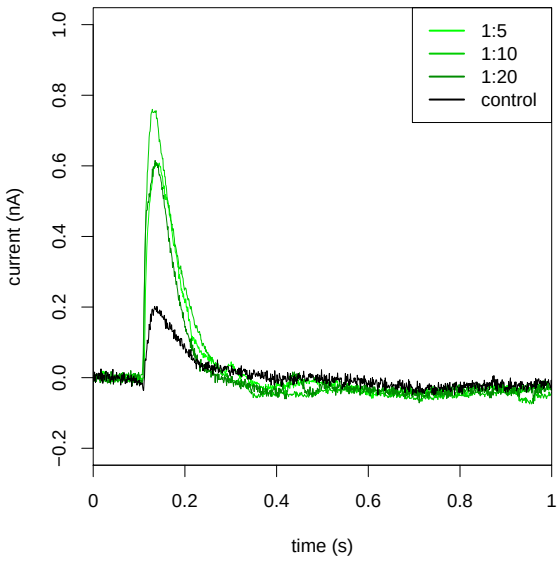

Figure 6.9: *Mn^{2+}-induced currents of MntH2 as a function of the LPR. His-tag cleaved MntH2 was used for this experiment. The decay phase of the currents is not influenced by the LPR, which would be expected if the signal represents transport. As discussed in the text, the reason for this could be, that the signal may represent only one single turnover. The highest amplitude is seen for the LPR 1:10, which was used throughout this thesis. The control was performed with empty liposomes that were prepared in the same reconstitution along with the proteoliposome samples. Traces are representative for four measurements on the same chip. Buffer: 10 mM HEPES, pH 8.0; 150 mM KCl; 2 mM $MgCl_2$.*

regardless of the origin of the signal, the amplitude should be higher at a

high LPR (even though the amplitude is also dependent on the sensor coverage). Consequently, this result neither confirms nor disagree with substrate transport. I hypothesise this behaviour is related to the very small space available in the lumen of proteoliposomes: In proteoliposomes with a diameter of 200 nm, a concentration of 100 μM Mn^{2+} corresponds to a total number of only ca. 250 Mn^{2+} ions. In the same proteoliposome, with an LPR of 1:20, the number of MntH2 is ca. 250 as well, estimated using a surface area per lipid of 0.6 nm^2. Therefore, even at the lowest LPR, one turnover of each protein is enough to bring the Mn^{2+} concentrations to equilibrium. Especially since a build up of an electrochemical gradient might stop transport before the inside concentration reaches equilibrium with the outside. In case of LacY experiments, a substrate concentration of 10 mM has been applied, which allows for more turnovers of the protein before the equilibrium is reached [200].

6.4.2 Substrate profile and K_M of different metals

Of the first row transition metals, it was found that besides Mn^{2+}, Co^{2+} and Zn^{2+} are substrates of MntH2. In addition, the toxic Cd^{2+} ion, of the second row transition metals, was identified as a substrate. Other transition metal substrates that were tested, which included Fe^{2+}, Ni^{2+} and Cu^{2+} did not show transport activity and neither did the earth-alkali metal ion Ca^{2+}. The summary of these results is shown in fig. 6.10 as a barplot: The

bars represent the average of four measurements (technical repeats) using 100 μM substrate at pH 8.0. The experiments for the transported cations (Mn^{2+}, Co^{2+}, Zn^{2+}, Cd^{2+}) have all been recorded on the same sensor. The data of Fe^{2+} and Ca^{2+} has been added by normalisation to Mn^{2+} activity. To determine the K_M of substrates, the peak amplitude was measured as

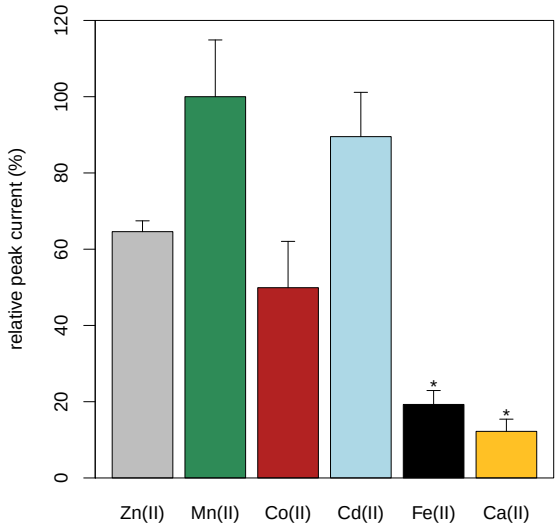

Figure 6.10: *Relative peak currents obtained with 100 μM of different transition metals. Currents of transported substrates (Zn(II), Mn(II), Co(II), Cd(II)) were all recorded on the same sensor where each measurements was repeated four times. The errorbars represent standard errors with a confidence intervall of 95 %. *Fe(II) and Ca(II) currents were recorded on a different sensor and amplitudes were calculated by normalisation to Mn(II) currents recorded on this sensor. Fe(II) currents were recorded in the presence of 1 mM of ascorbic acid in order to prevent oxidation to Fe(III).*

a function of substrate concentration (fig. 6.11). This experiment was performed for Mn^{2+}, Co^{2+} and Zn^{2+}, as well as for Ca^{2+} as a control, with substrate concentrations varying between 0 and 200 μM. As an additional

control, the same experiment was performed on a sensor with empty liposomes (using Mn^{2+}). The peak current showed very similar dependency for

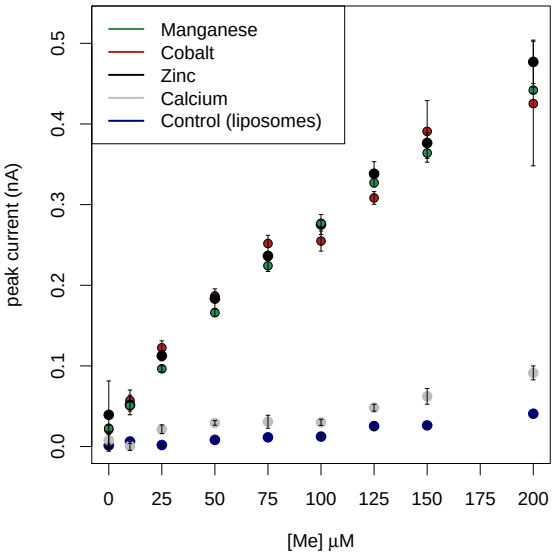

Figure 6.11: *Peak currents plotted as a function of Mn^{2+}, Co^{2+} and Zn^{2+} concentrations. As controls, the equivalent data obtained from measurements with a cation that is not transported (Ca^{2+}) is shown as well as a control of data with Mn^{2+} currents obtained on a different sensor with empty liposomes devoid of protein. Data is shown as mean ± SEM of four measurements on the same chip. Data is representative for one (Ca^{2+}), two (Zn^{2+} and Co^{2+}) or three (Mn^{2+}) biological replicates.*

all transported cations on substrate concentration. This dependency did not follow Michaelis-Menten-type behaviour, but was more linear. Because the data does not plateau, it is not possible to mathematically determine a K_M for this data. Even so, a lower limit of a K_M^{app} of 50 μM can be estimated. This is considerably higher than would be expected, because, as discussed, the physiological concentrations of these transition metals are in the range of nano- to low micromolar. There are different reasons why this could be the

case and I propose that the lack of an electrochemical gradient in SURFE^{2}R experiments leads to an increase in the apparent K_M. This possibility will be discussed in more detail in the section about MntH2 cotransport (sec. 6.5). For Mn^{2+} the experiment was also repeated for cleaved MntH2 (see appendix fig. A1a).

6.4.3 Inhibition experiments with non-transported metals

Given that some of the transition metal ions do not appear to be transported, it was tested how the presence of these ions influences Mn^{2+} transport. Experiments were performed where 100 μM of Cu^{2+}, Ni^{2+} or Fe^{2+} were present throughout the experiment while 100 μM Mn^{2+} was a constituent only of activating buffer. The results showed that Ni^{2+} and Cu^{2+} strongly inhibited Mn^{2+} uptake. In case of Ni^{2+} the inhibition was fully reversible, eg. when Ni^{2+} was washed out of the system, Mn^{2+} uptake signals would return to previous amplitude. In contrast, when inhibition was performed with Cu^{2+} the signal would recover only very slowly (incubation overnight) and often the amplitude would remain lower (ca. 70 %) than before inhibition. Only when Cu^{2+} was washed out with 10 mM EDTA the signal would recover close to its initial amplitude. This suggests that Cu^{2+} binds very tightly and specifically to the protein, likely in the same site as Mn^{2+} (i. e. competitive inhibition), although this was not experimentally verified. In tryptophane fluorescence experiments, Cu^{2+} binding could not be confirmed

due to its property of unspecific fluorescence quenching (section 5.8). Fe^{2+} did not cause a significant effect on the signal and therefore does not appear to interact with the metal binding site of the protein.

In order to demonstrate that inhibition of MntH2 is not caused by interac-

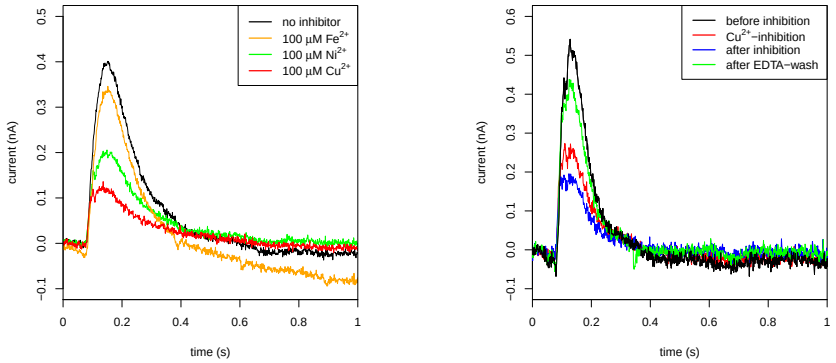

(a) *Influence of 100 µM of non-tranported metal ions on Mn^{2+} currents. Fe^{2+}, Ni^{2+} and Cu^{2+} were added to both, activating and non-activating buffer. Whereas Fe^{2+} has no significant effect, the presence of Ni^{2+} and Cu^{2+} strongly reduces the current. This suggests that Ni^{2+} and Cu^{2+} are competitive inhibitors whereas Fe^{2+} does not interact strongly with the protein.*

(b) *(Ir)-reversibility of Cu^{2+} inhibition. After MntH2 was inhibited with Cu^{2+}, Mn^{2+} currents would not return when no Cu^{2+} is added to buffers in the following experiment. Only after the sensor is washed with 10 mM EDTA, the amplitude would come back. For this experiment uncleaved MntH2 was used.*

Figure 6.12: *Inhibition of MntH2 with non-transported transition metal ions. Data in (a) and (b) is representative for two independent experiments on different sensors. In addition (a) was repeated with his-tag cleaved MntH2 (fig. A1b).*

tion of Ni^{2+} or Cu^{2+} with the his-tag, the previous experiment was repeated with his-tagged cleaved MntH2. This data is shown in the appendix (fig. A1b).

6.5 MntH2 cotransport

6.5.1 Influence of Cation and Anion composition in buffers

In summary, the experiments so far have shown that MntH2 transports Mn^{2+}, Cd^{2+}, Zn^{2+} and Co^{2+} and that it is inhibited by Ni^{2+} and Cu^{2+}. Next, it was attempted to get an understanding of the cotransport in MntH2. Although it is generally believed that MntH proteins are proton symporters [199, 201–204], there is only one publication so far that investigates of this aspect with purified protein [123]. In order to exclude that other monovalent cations (Na^+ or K^+) are involved in cotransport, experiments were carried out with buffers containing either 150 mM NaCl or 150 mM KCl, respectively. Mn^{2+}-induced currents were the same in both buffers which confirmed that neither Na^+ or K^+ is the cosubstrate (fig. 6.13). As an alternative, it was considered, if chloride ions are used as a cosubstrate. This may seem unlikely, but it has been suggested in previous work that anions might have a role in SLC11 cotransport [205]. This hypothesis came from the observation that $^{55}Fe^{2+}$ uptake into oocytes expressing DCT1 was strongly reduced when chloride was replaced by gluconate in the medium. Consequently, here experiment were conducted where chloride was replaced by gluconate in all buffers. It turned out that indeed, in gluconate buffer the signal was strongly suppressed (fig. 6.14). However, replacing chloride by sulfate did not lead to any alteration of the signal. Because it seemed

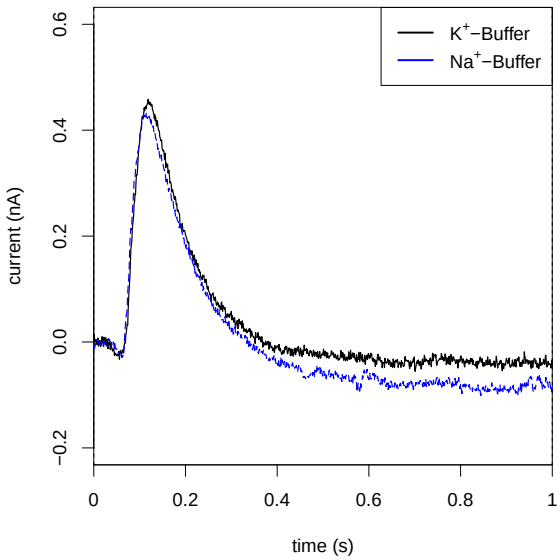

Figure 6.13: *MntH2 transport dependency on cationic buffer salt component. Mn^{2+} induced currents do not change when the salt component of the buffer is exchanged from 150 mM KCl to 150 mM NaCl. The conclusion is that MntH2 transport is neither K^+ nor Na^+ dependent. The data is representative for four measurements on the same sensor.*

unlikely that chloride and sulfate could be involved in the same transport mechansim, the hypothesis that anions are involved in cotransport was rejected. There are other reasons why the signal could be suppressed in gluconate buffers. One of them is that gluconate at this high concentration might complex the metal ions.

6.5.2 H^+ cotransport

Experiments with pH gradient

Given the results from the experiments described in the previous section, H^+ is still a likely cosubstrate in MntH2 transport. However, the difficulty in

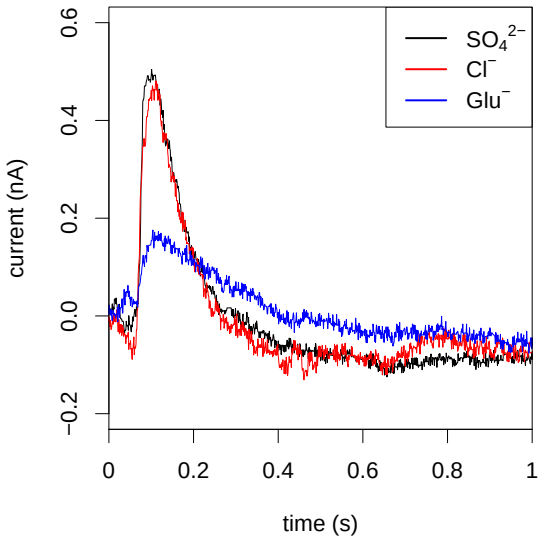

Figure 6.14: *Impact of anions on Mn^{2+} currents. Salt components in buffers for the different experiments were 1): 150 mM KCl, 2 mM $MgCl^{2+}$, 100 µM $MnCl_2$; 2): 150 mM NaGlu, 2 mM $MgGlu_2$, 100 µM $MnGlu_2$; 3): 30 mM K_2SO_4, 2 mM $MgSO_4$, 100 µM $MnSO_4$. The buffer was 10 mM HEPES, pH 8.0. Mn^{2+}-currents are suppressed in Glu^--buffer but are not affected in SO_4-buffer. The data is representative for four measurements each on two different sensors.*

showing H^+ cotransport is that it cannot simply be removed from buffers. One experiment that can be done on the SURFE^{2}R, is to generate a pH gradient and study its effect on metal transport. This can be achieved by adding a third buffer to the workflow and following a protocol similar to the one applied for TRPM2 (section 4.2). A pH gradient in the same direction should promote Me^{2+} transport, whereas a pH gradient opposite to the transport direction should hamper it. A problem with establishing a pH gradient in SURFE^{2}R experiments is that buffers with different pHs show very large signals upon solution exchange affecting the measurement.

For this reason it difficult to create a gradient of more than 0.5 pH units. Experiments were performed with buffers at pH 8.0 and 8.5. No difference in amplitudes could be determined between experiments where the pH was low on the inside or where it was low on the outside (fig. 6.15). Proton

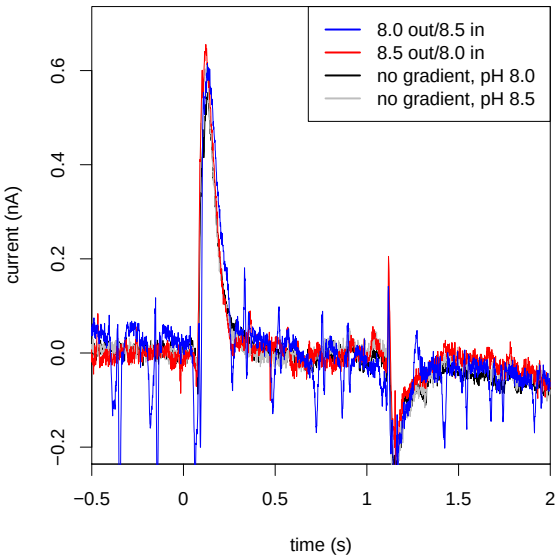

Figure 6.15: *SURFE^{2}R experiments on MntH2 making use of a pH gradient. If MntH2 is a H^+ symporter, a proton gradient in either direction should have an influence on the magnitude of the currents. The results show that regardless of the direction of the gradient the amplitude does not change. The black and grey trace were recorded without pH gradient and can be barely seen, because they are almost identical to the black and red trace. The experiment was repeated on two different sensors.*

symport could therefore not be confirmed in these types of experiments.

Experiments with the protonophore CCCP

A further method that allows observing proton (co)-transport in SURFE^{2}R experiments involves using a protonophore. In case of MntH2, if H^+ is a co-substrate, the electrometric currents will result from a combination of Mn^{2+}

and H^+ transport. Adding a protonophore, like CCCP (carbonyl cyanide m-chlorophenyl hydrazone), to the sensor changes the proton permeability of the proteoliposomes, which should lead to an alteration of the signal. To illustrate this effect, experiments were first performed with CCCP and NupC. NupC is a bacterial nucleoside/proton-symporter for which proton symport has previously been experimentally verified (Fig. 6.16B; [198]). In case of NupC, the addition of CCCP clearly led to a decrease in amplitude and importantly in width. This is expected as CCCP will dissipate any proton gradient very soon after transport starts. The leak current will then equalise the NupC pump current, which leads to a fast decrease in signal and explains the narrowing of the peak. The amplitude of the peak current (at t = 0), in theory, is not affected by the increased membrane conductivity. The peak current is recorded immediately after the start of substrate transport before an electrochemical potential gradient has built up and therefore leaking is not yet significant [172, 206]. In practice, however, the peak current will decrease due to the time required for solution exchange.

In contrast to NupC, no change was observed upon addition of CCCP to MntH2 (fig. 6.16A). This result strongly suggests that there is no contribution from proton flux to the signal.

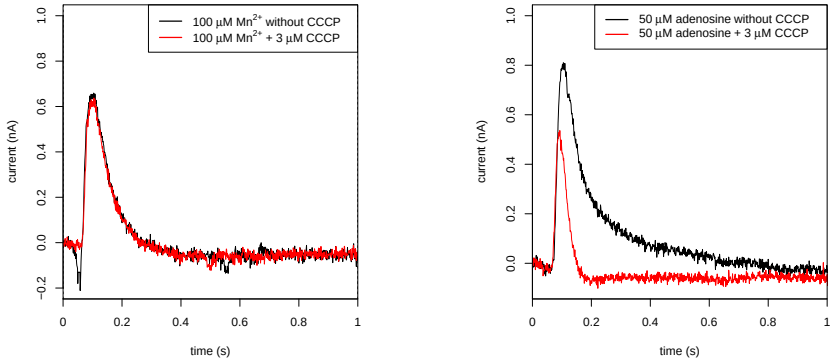

(a) *The presence of 3 µM CCCP in buffers A and B did not alter MntH2 currents, suggesting that protons do not contribute to the signal.*

(b) *Control with NupC currents. To test the effect of CCCP on proton currents, the experiments were performed under the same conditions as in A with the Adenosine/H^+ symporter NupC. The presence of CCCP clearly leads to a a decrease in amplitude and narrowing of the proton-current, providing evidence that under these experimental conditions CCCP does increase proton-permeability of the membranes.*

Figure 6.16: *Impact of the protonophore CCCP on SURFE^{2}R signal from different proteins. Data in (a) is representative for experiments on three different sensors. The experiment in (b) was performed on a single chip.*

6.6 Fluorescence Spectrometry

6.6.1 Proton transport assay using HPTS

Because in SURFE^{2}R experiments no signs of H^+ cotransport were detected, proton transport was monitored with a different method. In a fluorescence based method, the proton sensitive dye 8-Hydroxypyrene-1,3,6-trisulfonic acid trisodium salt (HPTS) was encapsulated in proteoliposomes containing MntH2. HPTS is a ratiometric dye: The emission is detected at 510 nm

but the dye is excited at two different excitation maxima at 400 and 448 nm. The ratio in fluorescence intensity is sensitive to the pH of the solution. This ratio was measured as a functions of pH to get a calibration curve. The calibration curve was measured with 0.5 μM of HPTS in assay buffer (5 mM MOPS; 150 mM KCl) with pH varying between 6.0 and 8.0. The ratio is not linear with pH but is following a Boltzmann equation (eq.6.1).

$$y = \frac{A_1 - A_2}{1 + e^{x - x_0}/dx} + A_2 \tag{6.1}$$

The Boltzmann equation yields four parameters (A_1, A_2, x_0 and dx) and adequately fits the calibration data (fig. 6.17).

When measuring proton transport into proteoliposomes, it has to be made certain that the proteoliposomes are sufficiently tight. This is important for transported protons not leaking back on a shorter time scale than is relevant for the measurement. A protocol to make proton tight liposomes has been introduced by Tsai and Miller [207]. The main finding of these authors was that a lipid composition of 3:1 POPE/POPG showed a much higher resistance to proton leaks than other lipid compositions, including *E. coli* polar lipid extract. In addition, the authors noticed that proton leakage was strongly dependent on the protein content in the vesicles: Proteoliposomes with a protein content higher than 15 μg protein/mg lipid, proton leakage became much more significant.

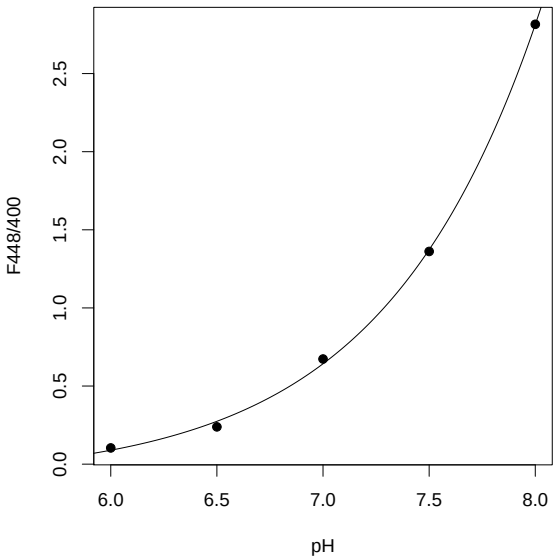

Figure 6.17: *HPTS fluorescence in solution as a function of pH. The ratio of fluorescence intensities at 510 nm from excitation at 448 and 440 nm was measured at five different pH in assay buffer (5 mM MOPS, pH 7.0; 150 mM KCl) with a concentration of 500 nM HPTS. The calibration curve is obtained by fitting the data to a Boltzmann equation.*

However, when test experiments with liposomes were reproduced in this thesis, liposomes prepared from *E. coli* polar lipids were observed to be less leaky than those prepared from POPE/POPG. Hence, the natural *E. coli* polar lipids were preferred to the synthetic lipid combination.

The experiment was performed at pH 7.0 and pH 8.0 using a low buffer strength, in order to make sure that transported protons would have an effect on the pH. After adding Mn^{2+} at different concentrations, a control was performed by adding HCl followed by the H^+/K^+ exchanger nigericin (fig. 6.18A). This was to reassure that the proteoliposomes under investigation

are sufficiently resistant to proton leaking.

The results shown in fig. 6.18 have been recorded at pH 7.0. The con-

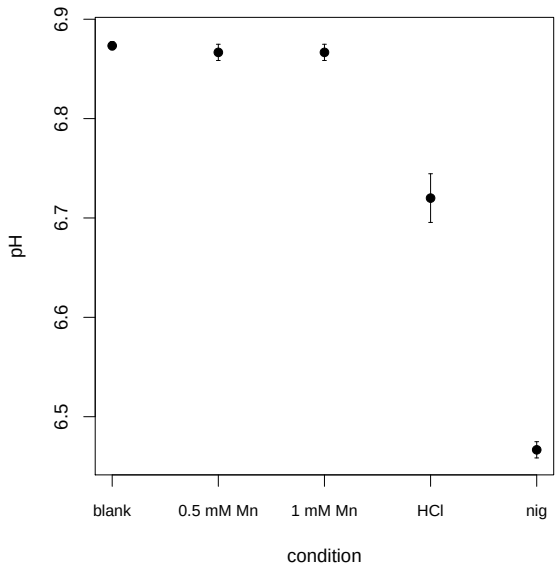

Figure 6.18: *Examination of MntH2 proton cotransport in fluorescence assays using the proton sensitive dye HPTS. A: Experiment at pH 7.0. Addition of up to 1 mM Mn^{2+} did not lead to a decrease of the pH inside the liposomes. The addition of HCl (0.5 µM) followed by the K^+/H^+ exchanger nigericin (0.1 µM) served as a control to show that proteoliposomes were sufficiently tight to protons to perform the assay. Points are the average from data recorded for 3x30 s with 30 s break in between. Buffer: 5 mM MOPS, pH 7.0; 150 mM KCl.*

clusion was the same as for experiments performed at pH 8.0: The data shows no indication of H^+ symport. This confirmed the results from the SURFE^{2}R experiments. Consequently, it is proposed that MntH2 works as a uniporter and does not require a cosubstrate for transport: The driving force for metal transport is provided by the electrochemical gradient only, where the twofold positive charge of the metal ions will cause them to be strongly attracted towards the negative potential inside the bacteria. When

evaluating equation (1.2), assuming a membrane potential of -70 mV and a concentration gradient of 100x more substrate inside, the free energy is still negative by ca. 2.1 kJ. This shows that at least from a thermodynamic point of view MntH2 could transport its substrate even against a large concentration gradient. This is especially the case when considering that inside the cell, the largest part of the Mn^{2+} is likely to be bound by proteins or small ligands and therefore removed from the equilibrium of MntH2 transport.

In line with the above considerations, the focus was on finding a method that could establish the importance of the electrical potential on MntH2 transport. For this purpose two techniques could be considered: One possibility was to use the SURFE^{2}R and perform experiments similar to the ones described in section 6.5.2 with the difference of using an electrical- instead of a pH gradient. The electrical gradient can be established by the use of valinomycin. It will be mentioned in the discussion to this chapter that these experiments failed due to technical problems. The second possibility was to perform fluorescence based measurements using a metal sensitive dye. The results from these experiments will be presented in the following two sections of this chapter.

6.7 Fluorescence assays of MntH2 metal ion transport

To assay metal ion transport in MntH2 it was required to decide on a suitable dye first. The dye calcein was chosen, because it is sensitive to a variety of different metal ions, including Mn^{2+}, Ni^{2+} and Co^{2+}. Calcein had the additional advantages that it is stable at room temperature and notably has been employed in functional studies on the two SLC11 homologous proteins of which the structure has been solved [122, 123]. A drawback of calcein is that it is not sensitive at pH 8.0, where the highest activity was seen in SURFE^{2}R experiments. As a consequence, the pH of the assay buffer was chosen to be 7.0. The sensitivity of calcein towards different metals was tested first in solution of the assay buffer (5 mM MOPS, pH 7.0; 150 mM KCl). The results confirmed the metal sensitivity of calcein, where the response towards Ni^{2+} ions is greater than for Mn^{2+} ions at the same concentration (fig. 6.19). Co^{2+}, Ca^{2+} and Cu^{2+} have been tested as well. The sensitivity of the former two metals was similar to that of Mn^{2+}, whereas Cu^{2+} completely quenched calcein fluorescence already at a concentration of 10 μM (data not shown).

The next step was to show that control vesicles devoid of protein do not allow transition metals to leak in. This test was performed with Mn^{2+}, Ni^{2+}, Ca^{2+} and Cu^{2+} (6.20). As expected, the liposomes were clearly im-

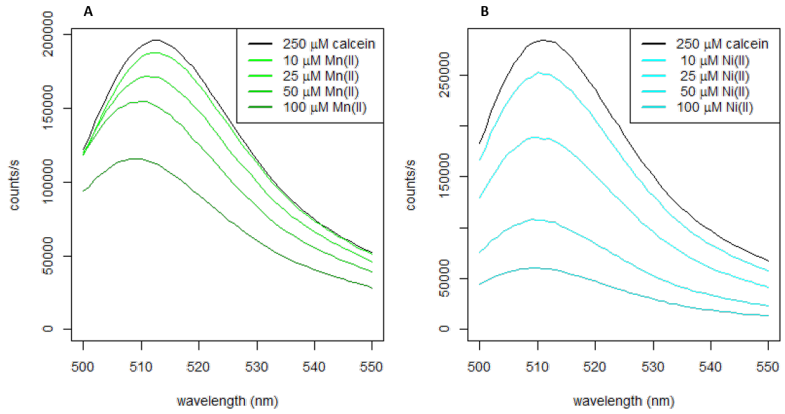

Figure 6.19: *Quenching of calcein dye in solution as a function of metal ion concentration. A: Quenching in response to Mn^{2+}. B: Quenching in response to Ni^{2+}. The comparison shows that the dye is more sensitive to Ni^{2+} than to Mn^{2+}. Buffer: 5 mM MOPS, pH 7.0; 150 mM KCl.*

permeable towards Mn^{2+}, Ni^{2+} and Ca^{2+}, but not to Cu^{2+}. The latter was quenching calcein fluorescence already at a concentration of 10 μM, indicating that Cu^{2+} could not be used in these studies. To determine the maximal fluorescence response of the calcein loaded vesicles, the Me^{2+}/H^{+} exchanger calimycin was added. After addition of 0.5 μg/mL calimycin, the fluorescence drops as the metal ions equilibrate with the inside of the liposomes. It was noted that the performance of the calimycin varies between metals and is less effective for Ni^{2+}-transport (fig. 6.20).

Time dependent metal ion uptake into MntH2 proteoliposomes are shown in fig. 6.21. The time resolution in these experiments was between ca. 10 - 20 s (the time required to take out the cuvette from the instrument, inject the sample and put the cuvette back in). Each of the tested metals was added at a concentration of 100 μM to proteoliposomes with an LPR of

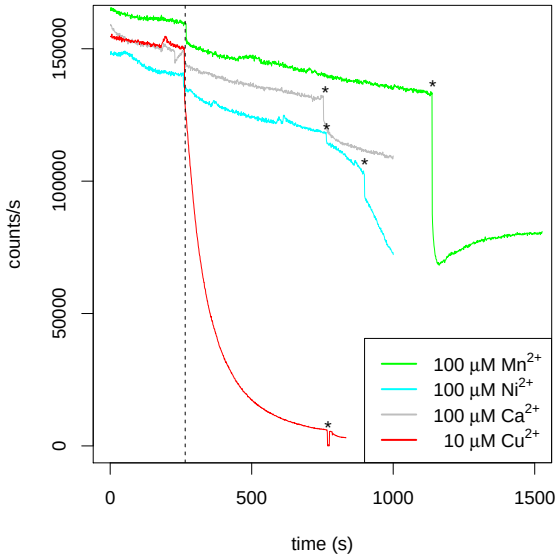

Figure 6.20: *Quenching of calcein dye inside lipsomes by different metal ions. When metal ions are added at a concentration of 100 µM to liposomes, that have calcein encapsulated, the fluorescence is greatly affected. The exception is Cu^{2+}, which almost completely quenches calcein fluorescence already at a concentration of 10 µM. When the Me^{2+}/H^{+} exchanger calimycin (0.5 µg/mL) is added (asterisk symbols), calcein fluorescence drops indicating metal induced quenching.*

1:50. An exception to this was the experiment with Zn^{2+}, which does not quench calcein fluorescence. The method to detect whether Zn^{2+} interacts with the protein is by investigating how the presence of Zn^{2+} affects uptake of Mn^{2+}. The procedure for this was adapted from Ehrnstorfer et al. [122] and accordingly 1 mM of Zn^{2+} was added to the sample at the start of the experiment. In the experiment calcein fluorescence was quenched upon addition of either Mn^{2+} or Ni^{2+}. While the former was expected as it confirms Mn^{2+} transport, the latter was more of a surprise, given that in SURFE^{2}R experiments, Ni^{2+} inhibited Mn^{2+} induced currents. An explanation for

this can be found by closer inspection of the results in fig. 6.21. It can be seen that Ni^{2+} uptake occurs at a much slower rate than Mn^{2+} uptake. In SURFE^{2}R experiments the peak amplitude is proportional to the speed of uptake, which can be the reason why Ni^{2+} transport does not show up as a current, but instead acts as a competitive inhibitor. The effect would be similar to that of Zn^{2+} in the fluorescence experiment. The presence of Zn^{2+} interferes with Mn^{2+} uptake, demonstrating that Zn^{2+} interacts with MntH2, even though from the fluorescence data alone it cannot be concluded whether Zn^{2+} is transported or is an inhibitor. The last cation used in this assay was Ca^{2+}. As expected, Ca^{2+} is not transported.

The calcein assay was repeated to test the concentration dependent response of Mn^{2+} and Ni^{2+}. The dose dependent initial velocity of the fluorescence quenching can be used to determine the Michaelis constant of transport, as described in section 2.5.1. Because of the low time resolution of the assay, proteoliposomes were prepared at different LPRs (1:70, 1:90, 1:110). Ni^{2+} uptake, which was expected to be slow, was measured at the highest LPR of 1:70 (fig. 6.22A). Because calcein fluorescence is sensitive to Ni^{2+}, the response was measured starting from a low concentration of 1 μM up to 100 μM. For Mn^{2+}, a faster uptake was expected, and therefore measurements were performed with the LPR 1:110 proteoliposomes. Mn^{2+} uptake was measured at concentrations between 10 and 200 μM (fig. 6.22B). In both experiments a clear dose-dependence of the calcein quenching was

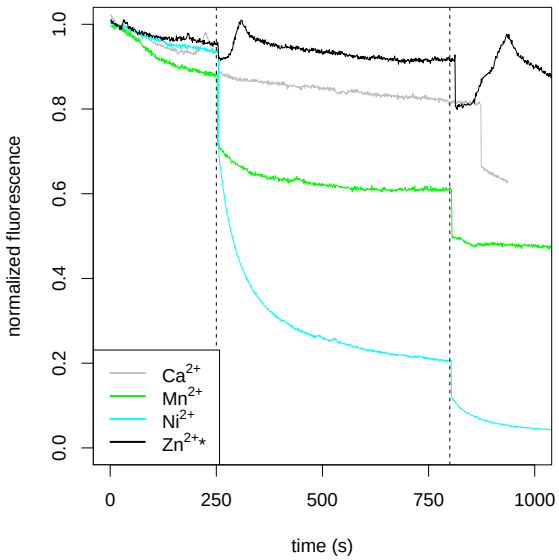

Figure 6.21: *Time dependent measurement of metal ion uptake into proteoliposomes with encapsulated calcein dye. The first vertical dashed line represents the addition of 100 μM of the corresponding metal ion (colours indicated in figure legend). In the special case of Zn^{2+}, at this point 100 μM Mn^{2+} is added, because calcein is insensitive to Zn^{2+}. Instead Zn^{2+} is present in an excess concentration of 1 mM in the background during the whole experiment. Addition of 100 μM Ni^{2+} or 100 μM Mn^{2+} leads to quenching of calcein fluorescence indicating metal ion uptake. The presence of excess Zn^{2+} interferes with Mn^{2+} uptake, which suggests that Zn^{2+} is either transported, or is an inhibitor of MntH2. Ca^{2+} is not transported. The second dashed line represents the addition of calimycin (slightly delayed for Ca^{2+}), which is to determine the maximal quenching to be observed.*

observed. To determine the initial velocities v_i, the data from the first 20 s of metal uptake were fitted to a straight line. The slope of that line was used as the estimate for the quantity v_i. From these quantities a K_M value of 14 μM was obtained for Ni^{2+} uptake by using the Michaelis Menten equation (eq. 1.5, fig. 6.22C). For Mn^{2+} not enough data was available to perform such a fit. Initial velocities plateaued already at 50μM Mn^{2+} which would suggest a $K_M << 50$ μM.

To get a better time resolution it was decided to repeat the experiments on

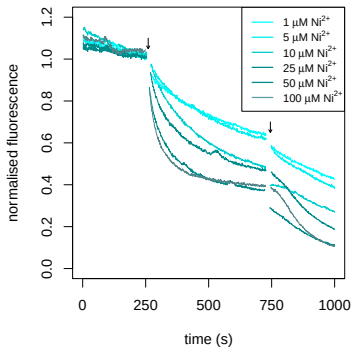

(a) *Ni^{2+}-uptake measured by quenching of calcein dye.*

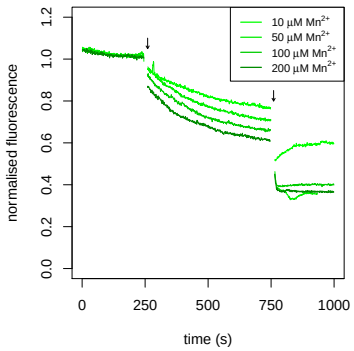

(b) *Mn^{2+}-uptake measured by quenching of calcein dye.*

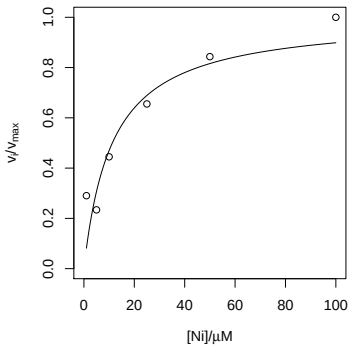

(c) *Michaelis fit of Ni^{2+} uptake.*

Figure 6.22: *Concentration dependent quenching of calcein in metal uptake assays. Calcein dye was incapsulated into proteoliposomes with MntH2 at LPRs of 1:70 (a) and 1:110 (b). Arrows in (a) and (b) indicate addition of metal ($t \sim 250$ s) and calimycin ($t \sim 750$ s). The initial velocities v_i were obtained by a linear fit to the first 20 s of data recorded after Ni^{2+} addition. v_i at 200 μM Ni^{2+} was assumed to be the maximum velocity v_{max}. (c): Michaelis Menten fit (eq. 1.5) of the data extracted from (a). The estimated K_M value from this fit was 14 μM. Experiments in (a) and (b) were performed just once.*

a stopped flow apparatus.

6.8 Fluorescence transport assays using the stopped flow

Fluorescence transport assays on the stopped flow apparatus work in principle the same as the assay described in the previous section. The difference is that this approach yields a much higher time resolution which is in the order of ca. 1 ms for the apparatus used here. Measuring at such low time resolution has some practical consequences. An important one to consider is, that integration times to accumulate fluorescent signal are much shorter in stopped flow experiments lowering fluorescence intensity and increasing noise.

Before measuring metal uptake by MntH2, it had to be evaluated what the maximal response of the system (F_{max}) would be, to make sure that the assay had a high enough sensitivity. To determine F_{max}, calimycin induced Mn^{2+} uptake into control liposomes was measured. It turned out, that when liposomes were prepared according to the same protocol as they have been for the experiments on the fluorimeter, there was almost no response seen in stopped flow experiments. To resolve this issue, the protocol was changed in the step to remove the external dye: Instead of using dialysis, dilution of residual dye in the bulk was achieved in steps that included ultracentrifugation. By this change the protocol is accelerated by ca. one day. This appeared to make a big difference as now calcein quenching could be clearly

observed in control experiments. MntH2 proteoliposomes were prepared in LPRs of 1:30, 1:70 and 1:110 together with control liposomes. However, neither sample containing MntH2 showed any uptake of Mn^{2+} in these experiments (fig. 6.23). Only when Mn^{2+} was added together with calimycin, fluorescence quenching was observed, which occurred to a similar degree as in control liposomes.

Naturally, it was tested whether the samples used in the stopped flow exper-

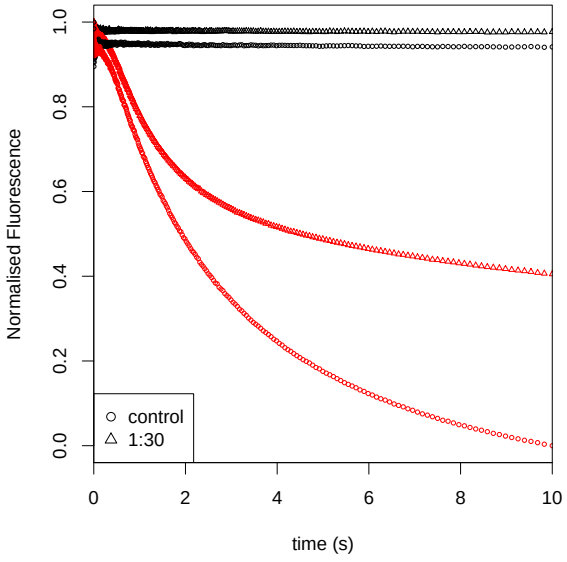

Figure 6.23: *Transport assay with incapsulated calcein vesicles on the stopped flow. One syringe was loaded with 200 µM Mn^{2+} in assay buffer (5 mM MOPS, pH 7.0; 150 mM KCl) either without (black) or with 1 µg/mL calimycin (red). The other syringe was loaded with (proteo)liposomes in a concentration of 0.2 mg/mL lipid. Samples of the two syringes were mixed in a ratio of 1:1 in the mixing chamber. Fluorescence excitation was performed at 492 nm and for detection a long pass filter with a cut-off wavelength of 515 nm was used. Mn^{2+} induced quenching of was observed neither if the sample was liposomes (control) or proteoliposomes (data shown for LPR 1:30) in the absence of calimycin. Only in the presence of calimycin, mixing of samples with Mn^{2+} led to a strong quenching of calcein fluorescence. This confirms that the assay is sensitive enough for Mn^{2+} uptake to be detected, but it is not observed for MntH2. This experiment has not been repeated.*

iments would show a signal on the fluorimeter. If for some reason transport was very slow, compared to previous experiments, it might be unnoticeable on a short time scale. These control experiments, however, confirmed the negative result. These negative results were confirmed when the experiment was repeated a second time, which means that the data presented in section 6.7 could not be reproduced. It was not possible within the time frame of this project to figure out where the problem lies but potential reasons for this will be discussed in section 6.9.

6.9 Discussion

The results presented in this chapter demonstrate that the SURFE^{2}R technique is applicable to investigate the transition metal transporter MntH2. Currents measured with this technique may correspond to any electrogenic process that is related to transport activity (substrate binding, conformational change and transport) but in case of MntH2 the signals were assigned to substrate transport. The alternatives were excluded for the following reasons: MntH2 currents do not represent electrogenic substrate binding, because currents are inhibited by Ni^{2+} and Cu^{2+}, two ions that on their own do not give rise to a signal. Inhibition of Ni^{2+} and Cu^{2+} has to be competitive: Structures of ScaDMT including different transition metal ions show that Ni^{2+} and Cu^{2+} bind to the same conserved binding pocket as Mn^{2+} [122]. If binding to the substrate pocket was electrogenic these ions

would also evoke currents in SURFE^{2}R experiments with MntH2. It has also been excluded that binding of ions to the his-tag contributes to the signal. Even though most experiments were performed with his-tagged MntH2, key experiments were repeated with his-tag cleaved protein and the obtained results were qualitatively the same. It is possible that MntH2 signals are caused by a conformational change, but it does not seem plausible: A conformational change is normally followed by substrate transport and is unlikely to be observed on its own. Therefore MntH2 currents are resulting from substrate transport. This conclusion is reached even though an attempt to show transport directly, by comparing proteoliposomes with varying LPRs, did not yield the expected result. A possible explanation for this is that substrate turnover stops rapidly due to the build up of the electrochemical gradient, as discussed in section 6.4.1.

The data obtained in SURFE^{2}R experiments shows that MntH2 is a Mn^{2+} transporter as has been proposed for members of the MntH family. Apart from Mn^{2+}, MntH2 is able to transport Cd^{2+} as well as Zn^{2+} and Co^{2+} albeit at a slower rate. Ni^{2+} is transported, but at such a low rate that no signal is observed in SURFE^{2}R experiments. This broad substrate specificity is consistent previous studies on homologous proteins which found that members of the family transport a wide range of transition metal ions [122, 141]. Our findings are slighly different from the ones of Richer et al. [151], who have examined metal sensitivity of *E. coli* overexpressing MntH2.

We observe Mn^{2+} but not Fe^{2+} transport while their study suggests it is the other way round. The problem of whole cell studies is that overexpression will always have side effects on the bacteria that are beyond control. For instance, one issue that these authors had was that MntH2 turned out to be cytotoxic when overexpressed in *E. coli*. Considering that Mn^{2+} is not as cytotoxic as other transition metals it might be that Mn^{2+} toxicity might have been masked under the MntH2-overexpression induced toxicity.

There is as well contradiction between our results and the study of Abrantes et al. [152], where they have shown that expression of MntH2 is downregulated in the presence of Mn^{2+} and Cu^{2+} and upregulated by excess Zn^{2+} or Fe^{2+}. It has been suggested that transcription of the *mntH2* gene is coupled with transcription of the next gene upstream the sequence [153]. This gene (*uspA*), encodes a member of the universal stress protein family (UspA) [208]. Proteins of this family have been studied in *E. coli* where it has been found that they are overexpressed under a number of different stress conditions [208]. It seems plausible that this protein is overexpressed in the presence of excess Fe^{2+} or Zn^{2+}. It remains unclear though, why MntH2 is downregulated in the presence of Cu^{2+}.

Interestingly, the trend that we see for the interaction of MntH2 with transition metals aligns with the well-known Irving Williams Series. This series predicts the stability of high-spin octahedral complexes of first row transi-

tion metal ions as follows:

$$Mn^{2+} < Fe^{2+} < Co^{2+} < Ni^{2+} << Cu^{2+} > Zn^{2+}$$

It is generally assumed that this trend applies for metal binding sites in proteins [209]. Mn^{2+} has the lowest affinity and is transported most efficiently, binding only weakly and is therefore released the fastest. Co^{2+} binds more strongly and is transported less efficiently. Very strong binding metals like Ni^{2+} and Cu^{2+} bind so tightly that they might not dissociate from the binding site at all and therefore block transport. An exception to this trend is Fe^{2+}, which does not appear to strongly interact with the protein.

The transport kinetics suggest K_M values that are high compared to physiologically relevant metal concentrations. This is contrary to the belief that MntH2 functions to efficiently scavenging trace elements from its surroundings. The most likely explanation for this is that the absence of a proton electrochemical gradient ($\Delta\overline{\mu}_{H^+}$) influences the kinetic parameters of the protein. The LacY transporter is a well studied example where the absence of a membrane potential causes a marked increase in apparent K_M: In membrane vesicles K_M^{app} increased more than a 100 fold in the absence of $\Delta\overline{\mu}_{H^+}$ [210]. Later qualitatively similar results have been obtained with LacY reconstituted in proteoliposomes [211] and in particular increased K_M values have been obtained as well when reconstituted LacY was probed in

SSM-electrophysiological experiments [200].

Complementary to SURFE^{2}R experiments, fluorescence based transport assays using the metal sensitive dye calcein were performed to observe metal uptake in MntH2. This experiments showed uptake for Mn^{2+} and Ni^{2+}. Ni^{2+} uptake was very slow, which fits well with the observation in SURFE^{2}R experiments, that Ni^{2+} inhibits Mn^{2+} currents. Despite this, there is a caveat to these results as later they could not be reproduced. Because this issue could not be reproduced within the time frame of this project, it was not possible to perform experiments investigating the effect of a membrane potential. It is hard to determine why the results of the fluorescence assay are not as reproducible as the experiments on the SURFE^{2}R. A reason could be that problems were caused by the ultracentrifugation step, that was introduced to optimise experiments for the stopped-flow.

Apart from the question which substrates are transported by MntH2 studies are presented to elucidate the cosubstrate of this putative symporter. Na^+ or K^+ are ruled out as substrates in line with published propositions that MntH proteins are proton symporters [199, 201–204]. However, in experiments which were designed to observe proton co-transport, no evidence could be found that H^+ is involved in the turnover cycle. This has led to the hypothesis that MntH2 is a uniporter and transport is driven solely by the electical potential gradient. Because there are many studies that have observed proton symport in SLC11 tranporters, it should be discussed

here whether this hypothesis can realistically be true. First, it is important to recall that although SLC11 proteins are widely considered proton symporters it has been recognised already in early studies that proton co-transport does not follow a strict stoichiometric ratio, but depends on the external conditions [142, 212]. These observations have led to the model that was introduced in section 1.6, fig. 1.13. In this very complicated model DMT1 is a Me^{2+}/H^{+}-symporter but sometimes may work as a H^{+} or Me^{2+} uniporter. Here, an alternative model is proposed that is less complicated. In this model DMT1 is a uniporter for Me^{2+}, but leaky to protons. This is not a new proposition as the phenomenon of "leak currents" or "mechanistic slips" in SLC11 proteins is well known and has been discussed in a review [213]. The decisive point in the proposal made here is that when DMT1 is transporting its substrates, it must become more leaky to H^{+}. This could be the case if for instance due to conformational changes in the protein some pathways open up, where H^{+} can slip through. If this suggestion is right, this would imply that when investigating proton flux in SLC11 transporters, it is hard to distinguish between coupled and uncoupled proton co-transport. This is the case in particular in studies conducted with whole cells which includes most of the ones mentioned above. An exception is the study by Courville et al. [203] where in addition to experiments with whole cells, uptake measurements have been conducted on activated *E. coli* membrane vesicles. In these experiments the authors have investigated the influence of

the different components of the electrochemical gradient (the electrical potential $\Delta\Psi$ and the pH gradient ΔpH) on *E. coli* MntH uptake of $^{109}Cd^{2+}$. In activated membrane vesicles ΔpH or $\Delta\Psi$ can be selectively deleted (in presence of potassium salt) by adding either nigericin (deletion of ΔpH) or valinomycin (deletion of $\Delta\Psi$). Based on their results of these experiments the authors claim to have found evidence that MntH forward transport is proton dependent. However, we cannot follow how the authors came to that conclusion as in our view their results suggest that the opposite is the case: They found that in the presence of nigericin $^{109}Cd^{2+}$ transport was increased, while it was abrogated by valinomycin. This implies that MntH transport does not rely on ΔpH but rather on $\Delta\Psi$ and hence this data supports the theory that protons are not required as a cosubstrate. We can only speculate that the authors came to a different conclusion because they found that when no external potassium was present MntH transport was abrogated by the protonophore CCCP. However, CCCP will dissipate ΔpH and $\Delta\Psi$ and hence this finding does not prove that transport is H^+ dependent and is perfectly consistent with the idea that these proteins might be uniporters.

Another important study has been mentioned in section 1.6.2 and was released recently together with the crystal structure of EcoDMT [123]. In that study, the authors characterised (co)-transport of EcoDMT in fluorescence experiments, similar to the ones performed in this thesis. Calcein was

incapsulated in proteoliposomes to measure metal uptake as described in section 6.7. To monitor H^+ co-transport the authors used the dye 9-amino-6-chloro-2-methoxyacridine (ACMA) instead of HPTS. Metal and proton transport was monitored under conditions with and without membrane potential. Interestingly, metal transport was observed under both conditions, but proton transport was observed only in the presence of a membrane potential. In case proton transport was strictly coupled to metal uptake, one would expect to see co-transport as well in the absence of a membrane potential. The observations made are in line with the hypothesis that binding or transport of metal renders the protein leaky to H^+ which in the presence of a membrane potential would lead to proton flow, but not in its absence. The authors also made a mutant of EcoDMT (H236A), where they replaced a histidine, which is hypothesised to have a role in proton transport, with an alanine. The mutant still showed metal uptake, albeit at a lower rate, but no proton transport was detectable. This could indicate that, as the authors suggest, H236 has a role of proton-coupling in the transport mechanism. At the same time, considering that the H236A mutant is still able to transport Mn^{2+}, this shows that metal transport in principle can work without proton coupling.

In order to strengthen the hypothesis that MntH2 is a uniporter, it was attempted here to measure substrate uptake of MntH2 under the influence of an electrical potential. In SURFE^{2}R experiments, an electrical gradient

can be established using a two-solution-exchange protocol in the presence of valinomycin. These experiments failed because of technical issues: A large artefact was seen where the exchange between non-activating and activating buffer occurs, which made it impossible to measure protein activity in this set up. The origin of this artefact is unknown. The influence of a membrane potential could have been tested in fluorescence experiments using calcein. The problem was that when it was attempted to optimise these experiments to be performed on a stopped-flow apparatus, they did not work and there was no time left to fix this issue.

6.9.1 Conclusions

The results presented in this chapter show that MntH2 transports a range of substrates including Mn^{2+}, Cd^{2+},Co^{2+} and Zn^{2+}. Ni^{2+} and Cu^{2+} are not transported and in fact inhibit manganese uptake. MntH2 cotransport could not be observed, neither in SURFE^{2}R experiments making use of the protonophore CCCP, nor in fluorescence based assay using the pH sensitive dye HPTS. These results strongly suggest that MntH2 is a uniporter, even though there may not be sufficient proof. In any case this topic deserves more investigation because inspection of data from literature shows that the matter of co-transport in SLC11 is far less clear that it is generally assumed.

Chapter 7

Crystallisation trials

7.1 Membrane protein crystallisation

Even though crystal structures have been solved of two SLC11 homologues, solving the structure of MntH2 would still be of great importance to understand how this protein transports its substrates. A full transport mechanism of SLC11 can not yet be established using the available structures. Moreover, it is uncertain how physiologically relevant the structures are, that have been published. In the structure of EcoDMT [123], no substrate was bound when the protein was co-crystallised with transition metal ions. This was in spite of the structure showing an outward open state. ScaDMT was crystallised in complex with a nanobody, which stapled the protein together in a dimer, which likely is not its native state [122]. Therefore it is evident that to get a more complete picture of transition metal transport, more structures are needed and MntH2 is an interesting candidate to get these.

If the two forms in which MntH2 is purified (P1 and P2; chapter 5) reflect different states of the protein (a possibility which has to be considered), crystal structures of P1 and P2 could be very helpful to establish a model of a transport cycle.

For crystallisation of membrane proteins (proteins in general) to succeed it is important to start crystallisation trials from a highly pure and homogeneous sample [214]. To achieve the required degree of purity, protein obtained from IMAC chromatography was purified further by using size exclusion chromatography (SEC; chapter 5). SEC has the advantage that not only are impurities eliminated from the sample, but it also removes aggregates and separates different multimers. This is especially important for crystallisation because, as mentioned, the quality of the preparation does not only depend on its purity, but also on its homogeneity.

Crystallisation trials for membrane proteins can be set up, in principle, in the same way as for soluble proteins. There are commercial screens available which have been designed especially for crystallisation of membrane proteins. These screens are based on findings about which buffer conditions have been successfully used in the past to obtain crystals from membrane proteins. For instance, screen conditions often contain PEG400, or other short-length PEGs, as these compounds work well as a precipitant [215]. There is also a different approach to crystallise membrane proteins, which is called the "lipidic cubic phase" crystallisation. With this method, membrane

proteins are crystallised in a lipidic rather than in a detergent environment. But even though there are certainly merits to this approach, this technique has not been applied here and will not be further discussed.

Attempts to crystallise MntH2 have been undertaken previously [108]. These trials also made use of commercial screens for membrane proteins and some crystals were obtained, even though they did not diffract. The approach taken here was to try and reproduce these hits first, and afterwards working on ways to optimise crystallisation conditions.

7.2 Crystallisation trials in DDM

MntH2 for crystallisation trials was purified by IMAC, followed by SEC as described in sections 5.3 - 5.4. After purification, the samples were immediately prepared for trials in order to minimise protein aggregation. The samples P1 and P2, which originated from the two different peaks in the chromatogram of IMAC purification (fig. 5.2b), were treated separately. Proteins were concentrated using a spin-concentrator (30 kDa; vivaspin) up to concentrations of 3.8 mg/mL (P1) and 8.4 mg/mL (P2) as confirmed by a BCA assay. The trials were set up using the commercial screens MemGold [216], MemGold2 [217] and MemSys/MemStart [214]. Each of these screens correspond to 96 different conditions. Plates were set up with the help of a crystallisation robot (NT8), where protein was mixed in a ratio of 1:1 with well solution to a total drop size of 0.2 μL. For all screens three drop 96-well plates were used where one drop per well was for P1 and another one for P2.

All plates were stored at 4 °C and trials were run for 34 days. In three of the conditions, crystals were formed which had the form of thin needles (fig. 7.1A, B and C). Because these needles are very hard to pick, only the ones shown in fig. 7.1B were shot at the synchotron. No diffraction was obtained, which confirms that at least these crystals are from protein. Interestingly, in conditions where needles were obtained, they showed up only in one of the drops. In two cases needles appeared in drop 2 (P2) and in one case in drop 1 (P1). In each case the second drop corresponding to the same well either remained clear or some minor precipitation was seen.

A fourth condition, that might be of interest is represented in fig. 7.1D. The heavy precipitation, which leads to very dense protein aggregation in some spots, could serve as a starting point for an optimisation trial.

7.3 Crystallisation trials in DMNG

For membrane protein crystallisation, DDM is not the most optimal detergent, partly because of its relatively long chain length. An alternative to DDM are the maltose neopentyl glycol based detergents, which have been shown to have favorable properties for membrane protein stability and crystallisation [191]. In the precedent thesis on MntH2 the protein has been found stable in these detergents and it was proposed that especially DMNG (fig. 7.2) would be a promising candidate for crystallisation because of its short chain length [108, 218].

Purification of MntH2 in DMNG was performed analogously to purification

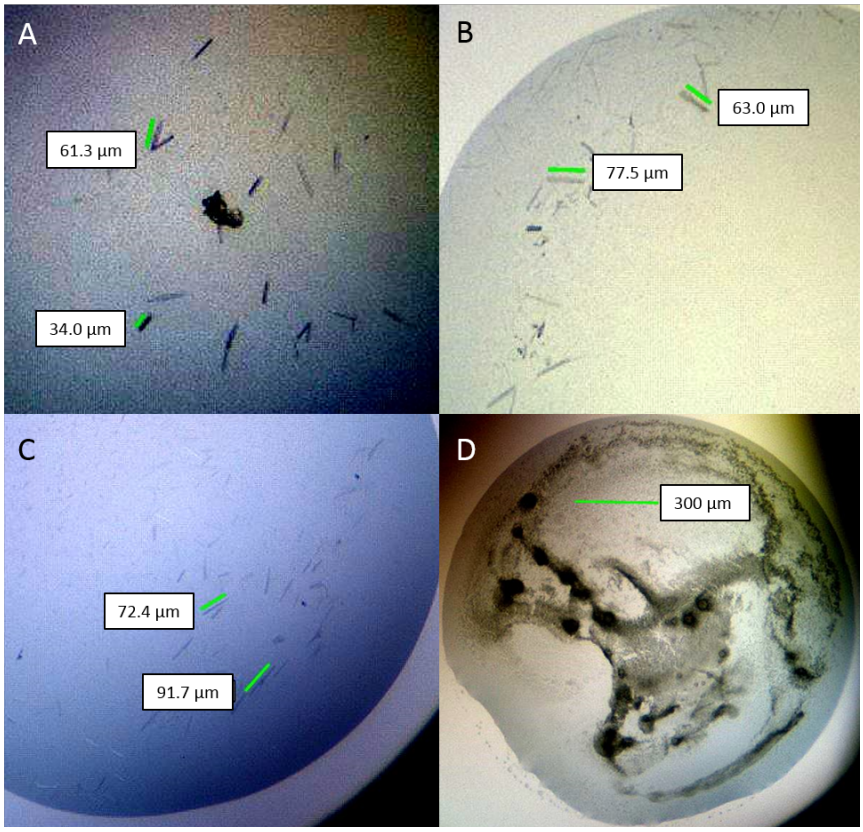

Figure 7.1: *Crystallisation trials on MntH2 in DDM buffer. Trials were set up in 96-well plates at 4 °C using the commercial screens MemGold, MemGold2 and MemSys/MemStart. Crystals in the shape of thin needles were obtained in three different drops, from P1 (3.8 mg/mL; A) and P2 (8.4 mg/mL; B and C). Well solutions were A: 0.2 M $(NH_4)_2SO_4$; 0.02 M NaCl; 0.02 M Na Acet, pH 4.0; 33 % v/v PEG 200, B: 0.2 M $CaCl_2$; 0.1 M MES, pH 5.0; 20 % v/v PEG MME 350, C: 0.2 M Ca Acet; 0.1 M HEPES, pH 7.0; 24 % v/v PEG 400. The precipitate in D is from P1 (3.8 mg/mL) and conditions were 0.01 M KCl; 0.02 M Tris, pH 7.0; 0.1 M K Acet; 44 % PEG 3K.*

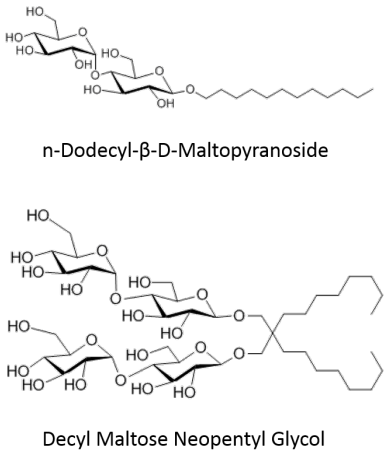

Figure 7.2: *Structure of detergents used for crystallisation trials.*

in DDM and is described in section 5.6. The following steps were performed immediately after purified protein was obtained. The protein was concentrated (spin-concentrator; 30 kDa) to concentrations of 6.5 mg/mL (P2) and 3.2 mg/mL (P1) as determined by nanodrop measurements. The first three plates were set up using the same three screens as before: MemGold, MemGold2 and MemSys/MemStart. These plates had the following load: Drops one and three were from P1, mixed in a ratio of 1:1 and 1.75:1 respectively and the final drop volume was 0.2 and 0.275 μL. Drop two was P2 mixed in a ratio of 1.75:1 to a drop volume of 0.275 μL. After these plates were left for storage at 4 °C, the remaining protein was concentrated further before setting up the next trials: P2 was concentrated up to 5.4 mg/mL protein concentration and P1 to 6.7 mg/mL as confirmed again on a nanodrop. Using this higher concentrated protein sample, two more crystallisation plates were set up, using the MemGold and MemGold2 screen. In these screens

drop one and three were loaded as before with P1, but in drop two, P2 was now mixed in a 1:1 ratio with well solution. Both plates were stored at 20 °C.

Of all five screens in total, there was one interesting result in particular. In one of the conditions at 4 °C, crystals appeared only 45 min after the plate was put into storage (fig. 7.3). This happened in drop 1 and drop 2, but not in drop 3. The appearance of these crystals suggested, that they might well be from membrane protein. However, the crystals remained stable for only eight more hours and were gone after one day. An issue with this condition was that when setting up the plate, the solution from this well has been mixed accidentally with a neighbouring well solution in a ratio of 1:1. This combination led to formation of salt crystals in the well solution, which appeared as well in the drops. These crystals were eventually shot at the synchotron where it was confirmed that they were salt crystals, but this does not change the fact that some of the crystals seen initially, looked promising.

7.4 Discussion

Two series of trials have been set up for MntH2 and the results appear quite promising. In a first series MntH2 it was attempted to reproduce crystallisation trials that have been performed in previous work, where some (non-diffracting) crystals were obtained [108]. In contrast to the preceding trials, MntH2 was separated into samples P1 and P2, a distinction that was

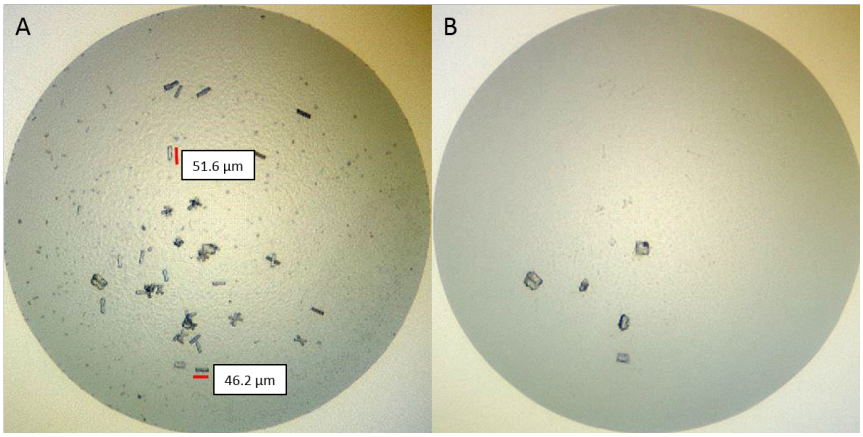

Figure 7.3: *Crystallisation trials on MntH2 in DMNG buffer (25 mM MES, pH 6.0; 150 mM NaCl; 0.05 % DMNG). Trials were set up in 96-well plates at both at 4 and at 20 °C using the commercial screens MemGold, MemGold2 and MemSys/MemStart as indicated in text. In the condition shown, already 45 min after starting the trial crystals appeared, that had the look to be from membrane protein. After only one day the crystals had redissolved and the remaining crystals were confirmed to be salt. Crystals appeared in drop one (1:1 P1 (3.2 mg/mL):buffer) and drop 2 (1.75:1 P2 (6.5 mg/mL):buffer). Well solution was a 1:1 mixture of 11 % PEG 600; 0.35 M $LiSO_4$; 0.1 M Na Acet, pH 4.5 and 38 % PEG 400; 0.2 M Ca Acet; 0.1 M Na Acet.*

found only, because MntH2 was eluted in a linear gradient in IMAC purification. In addition, MntH2 was screened with MemGold2, a complement to the MemGold screen incorporating more recent advances in membrane protein crystallography [217].

The result of this screen was that needle shaped crystals were obtained in three different conditions, albeit these were not identical to the conditions identified previously. Crystals from one condition (fig. 7.1) were shot at the synchotron, but no diffraction pattern was obtained.

Trials in DMNG led to one potentially interesting hit, where crystals were obtained that had the shape of small rods, which is an indication that they are membrane protein crystals. Unfortunately these crystals redissolved and

could not be investigated at the synchotron. If these crystals could be reproduced, they could be harvested in time and stored in liquid N_2.

In general terms MntH2 appears to have some properties that are quite favourable for crystallisation. It does have a high thermal stability, it does not have a strong tendency to aggregate and importantly, the yields are comparably very high for a membrane protein.

Chapter 8

Conclusions

In this thesis the SURFE^{2}R technique has been applied for two very different proteins: The human TRPM2 non-selective Ca^{2+} channel and the bacterial transition metal transporter *Enterococcus faecalis* MntH2. What these systems have in common is that they are both very challenging to characterise, for different reasons that have been explained in the text. As a result, not everything that has been tried to achieve has worked out in the end. Despite considerable effort it was not possible to monitor the activity of the TRPM2 channel in SURFE^{2}R experiments. The reasons for this remain unknown, but there is always a risk when taking a protein out of its native environment, that it will not behave well and may loose its functionality. It may also have to be conceded, that the SURFE^{2}R has not been designed primarily to investigate ion channels and therefore TRPM2 was not a straightforward target.

In contrast to experiments with TRPM2, characterisation with the SURFE^{2}R worked well for the transition metal transporter MntH2. Metal substrates and inhibitors of the protein were identified and a pH profile for activity was established. For these types of experiments the SURFE^{2}R has shown to be invaluable because it would have been much harder to get the same data with other techniques. The fluorescence based assay with calcein, also applied in this thesis, is much more time consuming and requires more protein. Also, the assay cannot be performed at arbitrary pH because calcein has a low sensitivity at pH $\geqslant$ 8.0. The most unexpected result from SURFE^{2}R experiments on MntH2 was that currents were unaffected by the protonophore CCCP, suggesting that MntH2 transport is not proton coupled. It has been proposed here that MntH2 may be a uniporter and arguments supporting this hypothesis were presented in chapter 6.

8.1 Future research

Future research on MntH2 would include experiments on the stopped flow. These would allow to obtain kinetic data of MntH2 transport under conditions with and without membrane potential. In the most ideal case these experiments would be conducted with his-tag cleaved protein, where protein from the two peaks in the IMAC step is treated separately. It might be worth to repeat some experiments on the SURFE^{2}R with protein from both peaks to see if there is any difference in functional behaviour. It would be interesting to compare the data obtained in this thesis with data from

a different SLC11 homologues, e.g. EcoDMT. In particular the experiment with CCCP should be repeated to confirm the finding made with MntH2 that metal transport in SLC11 can work without co-transport of protons. Crystallisation trials for MntH2 should be continued because there is still a demand for more structural information on SLC11 homologues. Optimisation trials could be set up around the crystallisation conditions that have been found in this project or in previous work. Another path that may be pursued is to try and obtain a structure with the LCP crystallisation technique.

Bibliography

[1] Voet D., Voet J. G., and Pratt C. W. *Principle of Biochemistry (Fourth Edition)*, book section Chapter 9 - Lipids, Bilayer and Membranes, pages 241–287. John Wiley & Sons, Inc., 2013.

[2] Drew D. and Boudker O. Shared Molecular Mechanisms of Membrane Transporters. *Annual Review of Biochemistry*, 85(1):543–572, 2016.

[3] Voet D., Voet J. G., and Pratt C. W. *Principle of Biochemistry (Fourth Edition)*, book section Chapter 10 - Passive and Active Transport, pages 288–314. John Wiley & Sons, Inc., 2013.

[4] Alberts B. and Bray D. *Essential Cell Biology (Third Edition)*, book section Chapter 12 - Membrane Transport, pages 387–425. Garland Science, Taylor & Francis Group, 2010.

[5] Doyle D. A., Cabral J. M., Pfuetzner R. A., Kuo A., Gulbis J. M., Cohen S. L., Chait B. T., and MacKinnon R. The Structure of the

Potassium Channel: Molecular Basis of K^+ Conduction and Selectivity. *Science*, 280(5360):69–77, 1998.

[6] Schrödinger, LLC. The PyMOL molecular graphics system, version 1.8. November 2015.

[7] Cuello L. G., Romero J. G., Cortes D. M., and Perozo E. pH-dependent gating in the *Streptomyces lividans* k^+ channel. *Biochemistry*, 37(10):3229–3236, 1998.

[8] Cuello L. G., Jogini V., Cortes D. M., and Perozo E. Structural mechanism of C-type inactivation in K^+ channels. *Nature*, 466(7303):203–U73, 2010.

[9] Tóth B. and Csanády L. Pore collapse underlies irreversible inactivation of TRPM2 cation channel currents. *Proceedings of the National Academy of Sciences of the United States of America*, 109(33):13440–13445, 2012.

[10] Jiang Y. X., Lee A., Chen J. Y., Ruta V., M Cadene, Chait B. T., and MacKinnon R. X-ray structure of a voltage-dependent K^+ channel. *Nature*, 423(6935):33–41, 2003.

[11] Long S. B., Campbell E. B., and MacKinnon R. Crystal structure of a mammalian voltage-dependent Shaker family K^+ channel. *Science*, 309(5736):897–903, 2005. Long, SB Campbell, EB MacKinnon, R.

[12] Kuo A. L., Gulbis J. M., Antcliff J. F., Rahman T., Lowe E. D., Zimmer J., Cuthbertson J., Ashcroft F. M., Ezaki T., and Doyle D. A. Crystal structure of the potassium channel KirBac1.1 in the closed state. *Science*, 300(5627):1922–1926, 2003.

[13] Jiang Y., Lee A., Chen J., Cadene M., Chait B. T., and MacKinnon R. Crystal structure and mechanism of a calcium-gated potassium channel. *Nature*, 417(6888):515–522, 2002.

[14] Payandeh J., Scheuer T., Zheng N., and Catterall W. A. The crystal structure of a voltage-gated sodium channel. *Nature*, 475(7356):353–358, 2011.

[15] Tang L., Gamal El-Din T. M., Payandeh J., Martinez G. Q., Heard T. M., Scheuer T., and Zheng N.and Catterall W. A. Structural basis for Ca^{2+} selectivity of a voltage-gated calcium channel. *Nature*, 505(7481):56–61, 2014.

[16] Yue L. X., Navarro B., Ren D. J., Ramos A., and Clapham D. E. The cation selectivity filter of the bacterial sodium channel, NaChBac. *Journal of General Physiology*, 120(6):845–853, 2002.

[17] Catterall W. A., Cestele S., Yarov-Yarovoy V., Yu F. H., Konoki K., and Scheuer T. Voltage-gated ion channels and gating modifier toxins. *Toxicon*, 49(2):124–41, 2007.

[18] Alper S. L. and Sharma A. K. The SLC26 gene family of anion transporters and channels. *Molecular Aspects of Medicine*, 34(2):494–515, 2013.

[19] Dutzler R., Campbell E. B., Cadene M., Chait B. T., and R. MacKinnon. X-ray structure of a ClC chloride channel at 3.0 Åreveals the molecular basis of anion selectivity. *Nature*, 415(6869):287–294, 2002.

[20] Accardi A. and Miller C. Secondary active transport mediated by a prokaryotic homologue of ClC Cl^- channels. *Nature*, 427(6977):803–807, 2004.

[21] Venkatachalam K.and Montell C. TRP Channels. *Annual Review of Biochemistry*, 76(1):387–417, 2007.

[22] Nilius B.and Owsianik G., Voets T., and Peters J. A. Transient Receptor Potential Cation Channels in Disease. *Physiological Reviews*, 87(1):165–217, 2007.

[23] Damann N., Voets T., and Nilius B. TRPs in our senses. *Current Biology*, 18(18):R880–R889, 2008.

[24] Nilius B. and Owsianik G. The transient receptor potential family of ion channels. *Genome Biology*, 12(3):218, 2011.

[25] Cosens D. J. and Manning Aubrey. Abnormal Electroretinogram from a Drosophila Mutant. *Nature*, 224(5216):285–287, 1969.

[26] Wes P. D., Chevesich J., Jeromin A., Rosenberg C., Stetten G., and Montell C. TRPC1, a human homolog of a *Drosophila* store-operated channel. *Proceedings of the National Academy of Sciences of the United States of America*, 92(21):9652–9656, 1995.

[27] Zhu X., Chu P. B., Peyton M., and Birnbaumer L. Molecular Cloning of a widely expressed human homolog for the *Drosophila trp* gene. *Febs Letters*, 373(3):193–198, 1995.

[28] Colbert H. A., Smith T. L., and Bargmann C. I. OSM-9, a novel protein with structural similarity to channels, is required for olfaction, mechanosensation, and olfactory adaptation in Caenorhabditis elegans. *Journal of Neuroscience*, 17(21):8259–8269, 1997.

[29] Jaquemar D., Schenker T., and Trueb B. An ankyrin-like protein with transmembrane domains is specifically lost after oncogenic transformation of human fibroblasts. *Journal of Biological Chemistry*, 274(11):7325–7333, 1999.

[30] Mochizuki T., Wu G. Q., Hayashi T., Xenophontos S. L., Veldhuisen B., Saris J. J., Reynolds D. M., Cai Y. Q., Gabow P. A., Pierides A., Kimberling W. J., Breuning M. H., Deltas C. C., Peters D. J. M., and Somlo S. PKD2, a gene for polycystic kidney disease that encodes an integral membrane protein. *Science*, 272(5266):1339–1342, 1996.

[31] Sun M., Goldin E., Stahl S., Falardeau J. L., Kennedy J. C., Acierno J.

S., Bove C., Kaneski C. R., Nagle J., Bromley M. C., Colman M., Schiffmann R., and Slaugenhaupt S. A. Mucolipidosis type IV is caused by mutations in a gene encoding a novel transient receptor potential channel. *Human Molecular Genetics*, 9(17):2471–2478, 2000.

[32] Bassi M. T., Manzoni M., Monti E., Pizzo M. T., Ballabio A., and Borsani G. Cloning of the gene encoding a novel integral membrane protein, mucolipidin - and identification of the two major founder mutations causing mucolipidosis type IV. *American Journal of Human Genetics*, 67(5):1110–1120, 2000.

[33] Bargal R., Avidan N., Ben-Asher E., Olender Z., Zeigler M., Frumkin A., Raas-Rothschild A., Glusman G., Lancet D., and Bach G. Identification of the gene causing mucolipidosis type IV. *Nature Genetics*, 26(1):118–121, 2000.

[34] Duncan L. M., Deeds J., Hunter J., Shao J., Holmgren L. M., Woolf E. A., Tepper R. I., and Shyjan A. W. Down-regulation of the novel gene melastatin correlates with potential for melanoma metastasis. *Cancer Research*, 58(7):1515–1520, 1998.

[35] Caterina M. J., Schumacher M. A., Tominaga M., Rosen T. A., Levine J. D., and Julius D. The capsaicin receptor: a heat-activated ion channel in the pain pathway. *Nature*, 389(6653):816–824, 1997.

[36] Tominaga M., Caterina M. J., Malmberg A. B., Rosen T. A., Gilbert

H., Skinner K., Raumann B. E., Basbaum A. I., and Julius D. The cloned capsaicin receptor integrates multiple pain-producing stimuli. *Neuron*, 21(3):531–543, 1998.

[37] Siemens J., Zhou S., Piskorowski R., Nikai T., Lumpkin E. A., Basbaum A. I., King D., and Julius D. Spider toxins activate the capsaicin receptor to produce inflammatory pain. *Nature*, 444(7116):208–212, 2006.

[38] Watanabe H., Vriens J., Suh S. H., Benham C. D., Droogmans G., and Nilius B. Heat-evoked activation of TRPV4 channels in a HEK293 cell expression system and in native mouse aorta endothelial cells. *Journal of Biological Chemistry*, 277(49):47044–47051, 2002.

[39] Guler A. D., Lee H., Iida T., Shimizu I., Tominaga M., and Caterina M. Heat-evoked activation of the ion channel, TRPV4. *J Neurosci*, 22(15):6408–14, 2002.

[40] Xu H., Ramsey I. S., Kotecha S. A., Moran M. M., Chong J. A., Lawson D., Ge P., Lilly J., Silos-Santiago I., Xie Y., DiStefano P. S., Curtis R., and Clapham D. E. TRPV3 is a calcium-permeable temperature-sensitive cation channel. *Nature*, 418(6894):181–6, 2002.

[41] Peier A. M., Reeve A. J., Andersson D. A., Moqrich A., Earley T. J., Hergarden A. C., Story G. M., Colley S., Hogenesch J. B., McIntyre P.,

Bevan S., and Patapoutian A. A heat-sensitive trp channel expressed in keratinocytes. *Science*, 296(5575):2046–9, 2002.

[42] Caterina M. J., Rosen T. A., Tominaga M., Brake A. J., and Julius D. A capsaicin-receptor homologue with a high threshold for noxious heat. *Nature*, 398(6726):436–41, 1999.

[43] McKemy D. D., Neuhausser W. M., and Julius D. Identification of a cold receptor reveals a general role for TRP channels in thermosensation. *Nature*, 416(6876):52–8, 2002.

[44] Peier A. M., Moqrich A., Hergarden A. C., Reeve A. J., Andersson D. A., Story G. M., Earley T. J., Dragoni I., McIntyre P., Bevan S., and Patapoutian A. A TRP channel that senses cold stimuli and menthol. *Cell*, 108(5):705–15, 2002.

[45] Nilius B., Prenen J., Droogmans G., Voets T., Vennekens R., Freichel M., Wissenbach U., and Flockerzi V. Voltage dependence of the Ca^{2+}-activated cation channel TRPM4. *Journal of Biological Chemistry*, 278(33):30813–30820, 2003.

[46] Nilius B., Talavera K., Owsianik G., Prenen J., Droogmans G., and Voets T. Gating of TRP channels: a voltage connection? *Journal of Physiology-London*, 567(1):35–44, 2005.

[47] Voets T., Droogmans G., Wissenbach U., Janssens A., Flockerzi V.,

and Nilius B. The principle of temperature-dependent gating in cold- and heat-sensitive TRP channels. *Nature*, 430(7001):748–754, 2004.

[48] Voets T., Talavera K., Owsianik G., and Nilius B. Sensing with TRP channels. *Nature Chemical Biology*, 1(2):85–92, 2005.

[49] Premkumar L. S., Raisinghani M., Pingle S. C., Long C., and Pimentel F. Downregulation of transient receptor potential melastatin 8 by protein kinase C-mediated dephosphorylation. *Journal of Neuroscience*, 25(49):11322–11329, 2005.

[50] Stokes A., Wakano C., Koblan-Huberson M., Adra C. N., Fleig A., and Turner H. TRPA1 is a substrate for de-ubiquitination by the tumor suppressor CYLD. *Cellular Signalling*, 18(10):1584–1594, 2006.

[51] Nilius B., Owsianik G., and Voets T. Transient receptor potential channels meet phosphoinositides. *Embo Journal*, 27(21):2809–2816, 2008.

[52] Rohacs T. and Nilius B. Regulation of transient receptor potential (TRP) channels by phosphoinositides. *Pflugers Archiv-European Journal of Physiology*, 455(1):157–168, 2007. Rohacs, Tibor Nilius, Bernd.

[53] Voets T. and Nilius B. Modulation of TRPs by PIPs. *Journal of Physiology-London*, 582(3):939–944, 2007.

[54] Liao M. F., Cao E. H., Julius D., and Cheng Y. F. Structure of the

TRPV1 ion channel determined by electron cryo-microscopy. *Nature*, 504(7478):107–+, 2013.

[55] Paulsen C. E., Armache J. P., Gao Y., Cheng Y. F., and Julius D. Structure of the TRPA1 ion channel suggests regulatory mechanisms. *Nature*, 520(7548):511–+, 2015.

[56] Zubcevic L., Herzik M. A., Chung B. C., Liu Z. R., Lander G. C., and Lee S. Y. Cryo-electron microscopy structure of the TRPV2 ion channel. *Nature Structural & Molecular Biology*, 23(2):180–+, 2016.

[57] Huynh K. W., Cohen M. R., Jiang J. S., Samanta A., Lodowski D. T., Zhou Z. H., and Moiseenkova-Bell V. Y. Structure of the full-length TRPV2 channel by cryo-EM. *Nature Communications*, 7, 2016.

[58] Saotome K., Singh A. K., Yelshanskaya M. V., and Sobolevsky A. I. Crystal structure of the epithelial calcium channel TRPV6. *Nature*, 534(7608):506–+, 2016.

[59] Cao E. H., Liao M. F., Cheng Y. F., and Julius D. TRPV1 structures in distinct conformations reveal activation mechanisms. *Nature*, 504(7478):113–+, 2013.

[60] Hunter J. J., Shao J., Smutko J. S., Dussault B. J., Nagle D. L., Woolf E. A., Holmgren L. M., Moore K. J., and Shyjan A. W. Chromo-

somal localization and genomic characterization of the mouse melastatin gene (Mlsn1). *Genomics*, 54(1):116–123, 1998.

[61] Behrendt H. J., Germann T., Gillen C., Hatt H., and Jostock R. Characterization of the mouse cold-menthol receptor TRPM8 and vanilloid receptor type-1 VR1 using a fluorometric imaging plate reader (FLIPR) assay. *British Journal of Pharmacology*, 141(4):737–745, 2004.

[62] Talavera K., Yasumatsu K., Voets T., Droogmans G., Shigemura N.and Ninomiya Y., Margolskee R. F., and Nilius B. Heat activation of TRPM5 underlies thermal sensitivity of sweet taste. *Nature*, 438(7070):1022–1025, 2005.

[63] Oancea E., Wolfe J. T., and Clapham D. E. Functional TRPM7 channels accumulate at the plasma membrane in response to fluid flow. *Circulation Research*, 98(2):245–253, 2006.

[64] Yin J. and Kuebler W. M. Mechanotransduction by TRP Channels: General Concepts and Specific Role in the Vasculature. *Cell Biochemistry and Biophysics*, 56(1):1–18, 2010. Yin, Jun Kuebler, Wolfgang M.

[65] Shen Y., Heimel J. A., Kamermans M., Peachey N. S., Gregg R. G., and Nawy S. A Transient Receptor Potential-Like Channel Mediates

Synaptic Transmission in Rod Bipolar Cells. *Journal of Neuroscience*, 29(19):6088–6093, 2009.

[66] Simon F., Varela D., and Cabello-Verrugio C. Oxidative stress-modulated TRPM ion channels in cell dysfunction and pathological conditions in humans. *Cellular Signalling*, 25(7):1614–1624, 2013.

[67] Herson P. S. and Ashford M. L. J. Activation of a novel non-selective cation channel by alloxan and H_2O_2 in the rat insulin-secreting cell line CRI-G1. *Journal of Physiology-London*, 501(1):59–66, 1997.

[68] Hara Y., Wakamori M., Ishii M., Maeno E., Nishida M., Yoshida T., Yamada H., Shimizu S., Mori E., Kudoh J., Shimizu N., Kurose H., Okada Y., Imoto K., and Mori Y. LTRPC2 Ca^{2+}-permeable channel activated by changes in redox status confers susceptibility to cell death. *Molecular Cell*, 9(1):163–173, 2002.

[69] Wehage E. and Eisfeld J. and Heiner I. and Jungling E. and Zitt C. and Lückhoff, A. Activation of the cation channel long transient receptor potential channel 2 (LTRPC2) by hydrogen peroxide - A splice variant reveals a mode of activation independent of ADP-ribose. *Journal of Biological Chemistry*, 277(26):23150–23156, 2002.

[70] Kuhn F. J. P. and Heiner I. and Lückhoff, A. TRPM2: a calcium influx pathway regulated by oxidative stress and the novel second mes-

senger ADP-ribose. *Pflugers Archiv-European Journal of Physiology*, 451(1):212–219, 2005.

[71] Miller B. A. The role of TRP channels in oxidative stress-induced cell death. *Journal of Membrane Biology*, 209(1):31–41, 2006.

[72] Simon F., Leiva-Salcedo E., Armisen R., Riveros A., Cerda O., Varela D., Eguiguren A. L., Olivero P., and Stutzin A. Hydrogen peroxide removes TRPM4 current desensitization conferring increased vulnerability to necrotic cell death. *Journal of Biological Chemistry*, 285(48):37150–37158, 2010.

[73] Becerra A., Echeverria C., Varela D., Sarmiento D., Armisen R., Nunez-Villena F., Montecinos M., and Simon F. Transient receptor potential melastatin 4 inhibition prevents lipopolysaccharide-induced endothelial cell death. *Cardiovascular Research*, 91(4):677–684, 2011.

[74] Gerzanich V., Woo S. K., Vennekens R., Tsymbalyuk O., Ivanova S., Ivanov A., Geng Z. H., Chen Z., Nilius B., Flockerzi V., Freichel M., and Simard J. M. De novo expression of Trpm4 initiates secondary hemorrhage in spinal cord injury. *Nature Medicine*, 15(2):185–191, 2009.

[75] Nunez-Villena F., Becerra A., Echeverria C., Briceno N., Porras O., Armisen R., Varela D., Montorfano I., Sarmiento D., and Simon F. Increased expression of the Transient Receptor Potential Melastatin

7 channel is critically involved in lipopolysaccharide-induced reactive oxygen species-mediated neuronal death. *Antioxidants & Redox Signaling*, 15(9):2425–2438, 2011.

[76] Nadler M. J. S., Hermosura M. C., Inabe K., Perraud A. L., Zhu Q. Q., Stokes A. J., Kurosaki T., Kinet J. P., Penner R., Scharenberg A. M., and Fleig A. LTRPC7 is a Mg center dot ATP-regulated divalent cation channel required for cell viability. *Nature*, 411(6837):590–595, 2001.

[77] Aarts M., Iihara K., Wei W. L., Xiong Z. G., Arundine M., Cerwinski W., MacDonald J. F., and Tymianski M. A key role for TRPM7 channels in anoxic neuronal death. *Cell*, 115(7):863–877, 2003.

[78] Wuensch T., Thilo F., Krueger K., Scholze A., Ristow M., and Tepel M. High glucose-induced oxidative stress increases transient receptor potential channel expression in human monocytes. *Diabetes*, 59(4):844–849, 2010.

[79] Chen H. C., Su L. T., Gonzalez-Pagan O., Overton J. D., and Runnels L. W. A key role for Mg^{2+} in TRPM7's control of ROS levels during cell stress. *Biochemical Journal*, 445:441–448, 2012.

[80] Launay P., Fleig A., Perraud A. L., Scharenberg A. M., Penner R., and Kinet J. P. TRPM4 is a Ca^{2+}-activated nonselective cation channel mediating cell membrane depolarization. *Cell*, 109(3):397–407, 2002.

[81] Bodding M. TRPM6: A Janus-like protein. *Handb Exp Pharmacol*, (179):299–311, 2007.

[82] Penner R. and Fleig A. The Mg^{2+} and Mg(2+)-nucleotide-regulated channel-kinase TRPM7. *Handb Exp Pharmacol*, (179):313–28, 2007.

[83] Perraud A. L., Fleig A., Dunn C. A., Bagley L. A., Launay P., Schmitz C., Stokes A. J., Zhu Q. Q., Bessman M. J., Penner R., Kinet J. P., and Scharenberg A. M. ADP-ribose gating of the calcium-permeable LTRPC2 channel revealed by Nudix motif homology. *Nature*, 411(6837):595–599, 2001.

[84] Sano Y., Inamura K., Miyake A., Mochizuki S., Yokoi H., Matsushime H., and Furuichi K. Immunocyte Ca^{2+} influx system mediated by LTRPC2. *Science*, 293(5533):1327–1330, 2001.

[85] Nagamine K., Kudoh J., Minoshima S., Kawasaki K., Asakawa S., Ito F., and Shimizu N. Molecular cloning of a novel putative Ca^{2+}channel protein (TRPC7) highly expressed in brain. *Genomics*, 54(1):124–131, 1998.

[86] Zhang W., Chu X., Tong Q., Cheung J. Y., Conrad K., Masker K., and Miller B. A. A novel TRPM2 isoform inhibits calcium influx and susceptibility to cell death. *Journal of Biological Chemistry*, 278(18):16222–16229, 2003.

[87] Heiner I. and Eisfeld J. and Lückhoff A. Role and regulation of TRP channels in neutrophil granulocytes. *Cell Calcium*, 33(5-6):533–540, 2003.

[88] Lange I., Yamamoto S., Partida-Sanchez S., Mori Y., Fleig A., and Penner R. TRPM2 Functions as a Lysosomal Ca^{2+}-Release Channel in beta Cells. *Science Signaling*, 2(71), 2009.

[89] Nada Abuarab. *TRPM2 ion channel trafficking and its role in mitochondrial fragmentation and cell death.* Phd, University of leeds, 2016.

[90] Sumoza-Toledo A. and Penner R. TRPM2: a multifunctional ion channel for calcium signalling. *J Physiol*, 589(7):1515–1525, 2011.

[91] Takahashi N., Kozai D., Kobayashi R., Ebert M., and Mori Y. Roles of TRPM2 in oxidative stress. *Cell Calcium*, 50:279–287, 2011.

[92] Maruyama Y., Ogura T., Mio K., Kiyonaka S., Kato K., Mori Y., and Sato C. Three-dimensional reconstruction using transmission electron microscopy reveals a swollen, bell-shaped structure of transient receptor potential melastatin type 2 cation channel. *Journal of Biological Chemistry*, 282(51):36961–36970, 2007.

[93] Togashi K., Hara Y., Tominaga T., Hihashi T., Konishi Y., Mori Y., and Tominaga M. TRPM2 activation by cyclic ADP-ribose at body

temperature is involved in insulin secretion. *EMBO J*, 25:1804–1815, 2006.

[94] Carter R. N., Tolhurst G., Walmsley G., Vizuete-Forster M., Miller N., and Mahaut-Smith M. P. Molecular and electrophysiological characterization of transient receptor potential ion channels in the primary murine megakaryocyte. *J Physiol*, 576:151–162, 2006.

[95] Hecquet C. M., Ahmmed G. U., Vogel S. M., and Malik A. B. Role of TRPM2 channel in mediating H_2O_2-induced Ca^{2+} entry and endothelial hyperpermeability. *Circ Res*, 102:347–355, 2008.

[96] Kraft R., Grimm C., Grosse K., Hoffmann A., Sauerbruch S., Kettenmann H., Schulz G., and Harteneck C. Hydrogen peroxide and ADP-ribose induce TRPM2 mediated calcium influx and cation currents in microglia. *Am J Physiol Cell Physiol*, 286:C129–C137, 2004.

[97] Olah M. E., Jackson M. F., Li H., Perez Y., Sun H. S., Kiyonaka S., Mori Y., Tymianski M., and MacDonald J. F. Ca^{2+}-dependent induction of TRPM2 currents in hippocampal neurons. *J Physiol*, 5:965–979, 2009.

[98] Yang W., Manna P. T., Zou J., Luo J., Beech D. J., Sivaprasadarao A., and Jiang L. H. Zinc inactivates Melastatin Transient Receptor Potential 2 channels via the outer pore. *J Biol Chem*, 286:23789–23798, 2011.

[99] Tong Q., Zhang W., Conrad C., Mostoller K., Cheung J. Y., Peterson B. Z., and Miller B. A. Regulation of the Transient Receptor Potential Channel TRPM2 by the Ca^{2+} Sensor Calmodulin . *jbc*, 281(14):9076–9085, 2006.

[100] Csanády L. and Törőcsik B. Four Ca^{2+} ions activate TRPM2 channels by binding in deep crevices near the pore but Intracellularly of the gate. *J Gen Physiol*, 133(2):189–203, 2009.

[101] Kolisek M., Beck A., Fleig A., and Penner R. Cyclic ADP-ribose and hydrogen peroxide synergize with ADP-ribose in the activation of TRPM2 channels. *Molecular Cell*, 18(1):61–69, 2005.

[102] Lange I., Penner R., Fleig A., and Beck A. Synergistic regulation of endogenous TRPM2 channels by adenine dinucleotides in primary human neutrophils. *Cell Calcium*, 44(6):604–615, 2008.

[103] Beck A., Kolisek M., Bagley L. A., Fleig A., and Penner R. Nicotinic acid adenine dinucleotide phosphate and cyclic ADP-ribose regulate TRPM2 channels in T lymphocytes. *Faseb Journal*, 20(7):962–+, 2006.

[104] Tóth B. and Csanády L. Identification of direct and indirect effectors of the Transient Receptor Potential Melastatin 2 (TRPM2) cation channel. *J Biol Chem*, 285:30091–30102, 2010.

[105] Starkus J. G., Fleig A., and Penner R. The calcium-permeable non-selective cation channel TRPM2 is modulated by cellular acidification. *J Physiol*, 588:1227–1240, 2010.

[106] Manna T., Munsey T., Abuarab N., Li F., Asipu A., Howell G., Sedo A., Yang W., Naylor J., Beech D. J., Jiang L. H., and Sivaprasadarao A. TRPM2-mediated intracellular Zn^{2+} release triggers pancreatic β-cell death. *Biochemical Journal*, 466:537–546, 2015.

[107] Zhang Z., Zhang W., Young Jung D., Jin Ko H., Lee Y., Friedline R. H., Lee E., Jun J., Ma Z., Kim F., Tsitsilianos N., Chapman K., Morrison A., Cooper M. P., Miller B. A., and Kim J. K. TRPM2 Ca^{2+} channel regulates energy balance and glucose metabolism. *Am J Physiol Endocrinol Metab*, 302:E807–E816, 2012.

[108] C. Ma. *Prokaryote proteins as experimentally amenable models for eukaryote transporters*. Phd, University of Leeds, 2013.

[109] Abramson J. and Wright E. M. Structure and function of Na^{+}-symporters with inverted repeats. *Current Opinion in Structural Biology*, 19(4):425–432, 2009.

[110] Hediger M. A., Clmenon B., Burrier R. E., and Bruford E. A. The ABCs of membrane transporters in health and disease (SLC series): Introduction. *Molecular Aspects of Medicine*, 34(2):95–107, 2013.

[111] Gruswitz F., Chaudhary S., Ho J. D., Schlessinger A., Pezeshki B., Ho C. M., Sali A., Westhoff C. M., and Stroud R. M. Function of human Rh based on structure of RhCG at 2.1 Å. *Proc Natl Acad Sci U S A*, 107(21):9638–43, 2010.

[112] Deng D., Xu C., Sun P., Wu J., Yan C., Hu M., and Yan N. Crystal structure of the human glucose transporter GLUT1. *Nature*, 510:121, 2014.

[113] Deng D., Sun P., Yan C., Ke M., Jiang X., Xiong L., Ren W., Hirata K., Yamamoto M., Fan S., and Yan N. Molecular basis of ligand recognition and transport by glucose transporters. *Nature*, 526:391, 2015.

[114] Yamashita A., Singh S. K., Kawate T., Jin Y., and Gouaux E. Crystal structure of a bacterial homologue of Na^+/Cl^--dependent neurotransmitter transporters. *Nature*, 437(7056):215–223, 2005.

[115] Huang Y. F., Lemieux M. J., Song J. M., Auer M., and Wang D. N. Structure and mechanism of the glycerol-3-phosphate transporter from *Escherichia coli*. *Science*, 301(5633):616–620, 2003.

[116] Abramson J., Smirnova I., Kasho V., Verner G., Kaback H. R., and Iwata S. Structure and mechanism of the lactose permease of *Escherichia coli*. *Science*, 301(5633):610–615, 2003.

[117] Yernool D., Boudker O., Jin Y., and Gouaux E. Structure of a glutamate transporter homologue from *Pyrococcus horikoshii*. *Nature*, 431(7010):811–818, 2004.

[118] Hunte C., Screpanti E., Venturi M., Rimon A., Padan E., and Michel H. Structure of a Na^+/H^+ antiporter and insights into mechanism of action and regulation by pH. *Nature*, 435(7046):1197–1202, 2005.

[119] Johnson Z. L., Cheong C. G., and Lee S. Y. Crystal structure of a concentrative nucleoside transporter from vibrio cholerae at 2.4 angstrom. *Nature*, 483(7390):489–U150, 2012.

[120] Reyes N., Ginter C., and Boudker O. Transport mechanism of a bacterial homologue of glutamate transporters. *Nature*, 462(7275):880–885, 2009.

[121] Lee C., Kang H. J., von Ballmoos C., Newstead S., Uzdavinys P., Dotson D. L., Iwata S., Beckstein O., Cameron A. D., and Drew D. A two-domain elevator mechanism for sodium/proton antiport. *Nature*, 501(7468):573–+, 2013.

[122] Ehrnstorfer I. A., Geertsma E. R., Pardon E., Steyaert J., and Dutzler R. Crystal structure of a SLC11 (NRAMP) transporter reveals the basis for transition-metal ion transport. *Nature Structural & Molecular Biology*, 21(11):990–996, 2014.

[123] Ehrnstorfer I. A., Manatschal C., Arnold F. M., Laederach J., and Dutzler R. Structural and mechanistic basis of proton-coupled metal ion transport in the SLC11/NRAMP family. *Nature Communications*, 8, 2017.

[124] Krishnamurthy H., Piscitelli C. L., and Gouaux E. Unlocking the molecular secrets of sodium-coupled transporters. *Nature*, 459(7245):347–355, 2009.

[125] Weyand S., Shimamura T., Yajima S., Suzuki S., Mirza O., K. Krusong, Carpenter E. P., Rutherford N. G., Hadden J. M., O'Reilly J., Ma P., Saidijam M., Patching S. G., Hope R. J., Norbertczak H. T., Roach P. C. J., Iwata S., Henderson P. J. F., and Cameron A. D. Structure and Molecular Mechanism of a Nucleobase-Cation-Symport-1 Family Transporter. *Science*, 322(5902):709–713, 2008.

[126] Gao X., Lu F. R., Zhou L. J., Dang S. Y., Sun L. F., Li X. C., Wang J. W., and Shi Y. G. Structure and Mechanism of an Amino Acid Antiporter. *Science*, 324(5934):1565–1568, 2009.

[127] Ressl S., van Scheltinga A. C. T., Vonrhein C., Ott V., and Ziegler C. Molecular basis of transport and regulation in the Na^+/betaine symporter BetP. *Nature*, 458(7234):47–U1, 2009.

[128] Shaffer P. L., Goehring A., Shankaranarayanan A., and Gouaux E.

Structure and Mechanism of a Na^+-Independent Amino Acid Transporter. *Science*, 325(5943):1010–1014, 2009.

[129] Faham S., Watanabe A., Besserer G. M., Cascio D., Specht A., Hirayama B. A., Wright E. M., and Abramson J. The crystal structure of a sodium galactose transporter reveals mechanistic insights into na(+)/sugar symport. *Science*, 321(5890):810–814, 2008.

[130] Shimamura T., Weyand S., Beckstein O., Rutherford N. G., Hadden J. M., Sharples D., Sansom M. S. P., Iwata S., Henderson P. J. F., and Cameron A. D. Molecular Basis of Alternating Access Membrane Transport by the Sodium-Hydantoin Transporter Mhp1. *Science*, 328(5977):470–473, 2010.

[131] Tang L., Bai L., Wang W. H., and Jiang T. Crystal structure of the carnitine transporter and insights into the antiport mechanism. *Nature Structural & Molecular Biology*, 17(4):492–U137, 2010.

[132] Krishnamurthy H. and Gouaux E. X-ray structures of LeuT in substrate-free outward-open and apo inward-open states. *Nature*, 481(7382):469–U80, 2012.

[133] Penmatsa A. and Gouaux E. How LeuT shapes our understanding of the mechanisms of sodium-coupled neurotransmitter transporters. *The Journal of Physiology*, 592(5):863–869, 2014.

[134] Wessling-Resnick M. Nramp1 and other transporters involved in metal withholding during infection. *Journal of Biological Chemistry*, 290(31):18984–18990, 2015.

[135] Nevo Y. and Nelson N. The NRAMP family of metal-ion transporters. *Biochimica Et Biophysica Acta-Molecular Cell Research*, 1763(7):609–620, 2006.

[136] Jabado N., Jankowski A., Dougaparsad S., Picard V., Grinstein S., and Gros P. Natural resistance to intracellular infections: Natural resistance-associated macrophage protein 1 (NRAMP1) functions as a pH-dependent manganese transporter at the phagosomal membrane. *Journal of Experimental Medicine*, 192(9):1237–1247, 2000.

[137] Picard V., Govoni G., Jabado N., and Gros P. Nramp 2 (DCT1/DMT1) expressed at the plasma membrane transports iron and other divalent cations into a calcein-accessible cytoplasmic pool. *Journal of Biological Chemistry*, 275(46):35738–35745, 2000.

[138] Forbes J. R. and Gros P. Iron, manganese, and cobalt transport by Nramp1 (Slc11a1) and Nramp2 (Slc11a2) expressed at the plasma membrane. *Blood*, 102(5):1884–1892, 2003.

[139] Goswami T., Bhattacharjee A., Babal P., Searle S., Moore E., Li M., and Blackwell J. M. Natural-resistance-associated macrophage protein

1 is an H^+/bivalent cation antiporter. *Biochemical Journal*, 354:511–519, 2001.

[140] Techau M. E., Valdez-Taubas J., Popoff J. F., Francis R., Seaman M., and Blackwell J. M. Evolution of differences in transport function in slc11a family members. *Journal of Biological Chemistry*, 282(49):35646–35656, 2007.

[141] A. C. Illing, A. Shawki, C. L. Cunningham, and B. Mackenzie. Substrate profile and metal-ion selectivity of human divalent metal-ion transporter-1. *Journal of Biological Chemistry*, 287(36):30485–30496, 2012.

[142] Gunshin H., Mackenzie B., Berger U. V., Gunshin Y., Romero M. F., Boron W. F., Nussberger S., Gollan J. L., and Hediger M. A. Cloning and characterization of a mammalian proton-coupled metal-ion transporter. *Nature*, 388(6641):482–488, 1997.

[143] Mackenzie B., Ujwal M. L., Chang M. H., Romero M. F., and Hediger M. A. Divalent metal-ion transporter DMT1 mediates both H+-coupled Fe^{2+} transport and uncoupled fluxes. *Pflugers Archiv-European Journal of Physiology*, 451(4):544–558, 2006.

[144] Bozzi A. T., Bane L. B., Weihofen W. A., McCabe A. L., Singharoy A., Chipot C. J., Schulten K., and Gaudet R. Conserved methionine dictates substrate preference in Nramp-family divalent

metal transporters. *Proceedings of the National Academy of Sciences*, 113(37):10310–10315, 2016.

[145] Lam-Yuk-Tseung S., Govoni G., Forbes J., and Gros P. Iron transport by Nramp2/DMT1: pH regulation of transport by 2 histidines in transmembrane domain 6. *Blood*, 101(9):3699–3707, 2003.

[146] Kehres D. G. and Maguire M. E. Emerging themes in manganese transport, biochemistry and pathogenesis in bacteria. *FEMS Microbiology Reviews*, 27(2-3):263–290, 2003.

[147] Kehres D. G., Janakiraman A., Slauch J. M., and Maguire M. E. SitABCD is the alkaline Mn^{2+} transporter of *Salmonella enterica* Serovar Typhimurium. *Journal of Bacteriology*, 184(12):3159–3166, 2002.

[148] Zaharik M. L., Cullen V. L., Fung A. M., Libby S. J., Choy S. L. K., Coburn B., Kehres D. G., Maguire M. E., Fang F. C., and Finlay B. B. The *Salmonella enterica* Serovar Typhimurium divalent cation transport systems MntH and SitABCD are essential for virulence in an Nramp1(G169) murine typhoid model. *Infection and Immunity*, 72(9):5522–5525, 2004.

[149] Jensen A. N. and Jensen L. T. *Manganese Transport, Trafficking and Function in Invertebrates*, volume 22 of *Manganese in Health and Disease*. 2015. Jensen, Amornrat Naranuntarat Jensen, Laran T.

[150] Corbin B. D., Seeley E. H., Raab A., Feldmann J., Miller M. R., Torres V. J., Anderson K. L., Dattilo B. M., Dunman P. M., Gerads R., Caprioli R. M., Nacken W., Chazin W. J., and Skaar E. P. Metal chelation and inhibition of bacterial growth in tissue abscesses. *Science*, 319(5865):962–965, 2008.

[151] Richer E., Courville P., Bergevin I., and Cellier M. F. M. Horizontal gene transfer of "prototype" Nramp in bacteria. *Journal of Molecular Evolution*, 57(4):363–376, 2003.

[152] Abrantes M. C., Kok J., and Lopes M. D. EfaR Is a Major Regulator of *Enterococcus faecalis* Manganese Transporters and Influences Processes Involved in Host Colonization and Infection. *Infection and Immunity*, 81(3):935–944, 2013.

[153] Lopez G., Latorre M., Reyes-Jara A., Cambiazo V., and Gonzalez M. Transcriptomic response of *Enterococcus faecalis* to iron excess. *Biometals*, 25(4):737–747, 2012.

[154] Ma C., Hao Z. Y., Huysmans G., Lesiuk A., Bullough P., Wang Y. Y., Bartlam M., Phillips S. E., Young J. D., Goldman A., Baldwin S. A., and Postis V. L. G. A Versatile Strategy for Production of Membrane Proteins with Diverse Topologies: Application to Investigation of Bacterial Homologues of Human Divalent Metal Ion and Nucleoside Transporters. *Plos One*, 10(11), 2015.

[155] Clayton Paul R. *Fundamentals of Electric Circuit Analysis*. John Wiley & Sons, Inc., 2001.

[156] Piccolino M. Animal electricity and the birth of electrophysiology: the legacy of Luigi Galvani. *Brain Research Bulletin*, 46(5):381–407, 1998.

[157] Cole K. S. and Curtis H. J. Electric impedance of the squid giant axon during activity. *The Journal of General Physiology*, 22(5):649–670, 1939.

[158] Neher E., Sakmann B., and Steinbach J. H. Estracellular patch clamp - method for resolving currents through individual open channels in biological-membranes. *Pflugers Archiv-European Journal of Physiology*, 375(2):219–228, 1978.

[159] Rubaiy H. N. A short guide to electrophysiology and ion channels. *Journal of Pharmacy and Pharmaceutical Sciences*, 20:48–67, 2017.

[160] Hamill O. P., Marty A., Neher E., Sakmann B., and Sigworth F. J. Improved patch-clamp techniques for high-resolution current recording from cells and cell-free membrane patches. *Pflugers Archiv-European Journal of Physiology*, 391(2):85–100, 1981.

[161] Yajuan X., Xin L., and Zhiyuan L. A comparison of the performance and application differences between manual and automated patch-clamp techniques. *Curr Chem Genomics*, 6:87–92, 2012.

[162] Priest B. T., Swensen A. M., and McManus O. B. Automated electrophysiology in drug discovery. *Current Pharmaceutical Design*, 13(23):2325–2337, 2007.

[163] Pintschovius J. and Fendler K. Charge translocation by the Na^+/K^+-ATPase investigated on solid supported membranes: Rapid solution exchange with a new technique. *Biophysical Journal*, 76(2):814–826, 1999.

[164] Grewer C., Gameiro A., Mager T., and Fendler K. *Electrophysiological characterization of membrane transport proteins*, volume 42 of *Annual Review of Biophysics*, pages 95–120. Annual Reviews, Palo Alto, 2013.

[165] Pintschovius J., Fendler K., and Bamberg E. Charge translocation by the Na^+/K^+-ATPase investigated on solid supported membranes: Cytoplasmic cation binding and release. *Biophysical Journal*, 76(2):827–836, 1999.

[166] Meyer-Lipp K., Ganea C., Pourcher T., Leblanc G., and Fendler K. Sugar binding induced charge translocation in the melibiose permease from *Escherichia coli*. *Biochemistry*, 43(39):12606–12613, 2004.

[167] Schulz P., Dueck B., Mourot A., Hatahet L., and Fendler K. Measuring ion channels on solid supported membranes. *Biophysical Journal*, 97(1):388–396, 2009.

[168] Drachev L. A., Jasaitis A. A., Kaulen A. D., Kondrashin A. A., Liberman E. A., Nemecek I. B., Ostroumov S. A., Semenov A. Y., and Skulachev V. P. Direct measurement of electric-current generation by cytochrome-oxidase, H^+-ATPase and bacteriorhodopsin. *Nature*, 249(5455):321–324, 1974.

[169] E. Neher and B. Sakmann. Single-channel currents recorded from membrane of denervated frog muscle-fibers. *Nature*, 260(5554):799–802, 1976.

[170] Bamberg E. and Apell H. J. and Dencher N. A. and Sperling W. and Stieve H. and Läuger, P. Photocurrents generated by bacteriorhodopsin on planar bilayer membranes. *Biophysics of Structure and Mechanism*, 5(4):277–292, 1979.

[171] Herrmann T. R. and Rayfield G. W. The electrical response to light of bacteriorhodopsin in planar membranes. *Biophysical Journal*, 21(2):111–125, 1978.

[172] Borlinghaus R., Apell H. J., and P. Läuger. Fast charge translocations associated with partial reactions of the Na,K-Pump: I. Current and voltage transients after photochemical release of ATP. *Journal of Membrane Biology*, 97(3):161–178, 1987.

[173] Fahr A., Läuger P., and Bamberg E. Photocurrent kinetics of purple-

membrane sheets bound to planar bilayer membranes. *The Journal of Membrane Biology*, 60(1):51–62, 1981.

[174] Fendler K., Jaruschewski S., Hobbs A., Albers W., and Froehlich J. P. Pre-steady-state charge translocation in nak-atpase from eel electric organ. *Journal of General Physiology*, 102(4):631–666, 1993.

[175] Zhou A., Wozniak A., Meyer-Lipp K., Nietschke M., Jung H., and Fendler K. Charge translocation during cosubstrate binding in the Na^+/proline transporter of *E-coli*. *Journal of Molecular Biology*, 343(4):931–942, 2004.

[176] Xu J., Wang X. B., Ensign B., Li M., Wu L., Guia A., and Xu J. Q. Ion-channel assay technologies: quo vadis? *Drug Discovery Today*, 6(24):1278–1287, 2001.

[177] Chao Y. and Fu D. Kinetic study of the antiport mechanism of an *Escherichia coli* zinc transporter, ZitB. *Journal of Biological Chemistry*, 279(13):12043–12050, 2004.

[178] Mei Z. Z., Mao H. J., and Jiang L. H. Conserved cysteine residues in the pore region are obligatory for human TRPM2 channel function. *American Journal of Physiology-Cell Physiology*, 291(5):C1022–C1028, 2006.

[179] IonGate Biosciences GmbH. *General Procedures for Assay Development*, March 2008.

[180] Zhao H., Ruberu K., Li H., and Garner B. Analysis of subcellular [^{57}Co] cobalamin distribution in SH-SY5Y neurons and brain tissue. *Journal of Neuroscience Methods*, 217:67–74, 2013.

[181] Laemmli U. K. Cleavage of Structural Proteins during the Assembly of the Head of Bacteriophage t4. *Nature*, 227:680–685, 1970.

[182] Meyer T. S. and Lamberts B. L. Use of coomassie brilliant blue R250 for the electrophoresis of microgram quantities of parotid saliva proteins on acrylamide-gel strips. *Biochim Biophys Acta*, 107(1):144–145, 1965.

[183] Kaback H. R. Bacterial membranes. *Methods Enzymol*, 22:99–120, 1971.

[184] Geertsma E. R., Mahmood N. A. B. N., Schurman-Wolters G. K., and Poolman B. Membrane reconstitution of ABC transporters and assays of translocator function. *Nat protoc*, 3:256–266, 2008.

[185] R Core Team. *R: A Language and Environment for Statistical Computing*. R Foundation for Statistical Computing, Vienna, Austria, 2013.

[186] Sumoza-Toledo A. and Penner R. TRPM2: a multifunctional ion chan-

nel for calcium signalling. *Journal of Physiology-London*, 589(7):1515–1525, 2011.

[187] Du J., Xie J., and Yue L. Intracellular calcium activates TRPM2 and its alternative spliced isoforms. *Proc Natl Acad Sci*, 106(17):7239–7244, 2008.

[188] Rath A. and Deber C. M. Correction factors for membrane protein molecular weight readouts on sodium dodecyle sulfate-polyacrylamide gel electrophoresis. *Analytical Biochemistry*, 434:67–72, 2013.

[189] Wei Y. N., Li H. L., and Fu D. Oligomeric state of the *Escherichia coli* metal transporter YiiP. *Journal of Biological Chemistry*, 279(38):39251–39259, 2004.

[190] Slotboom D. J., Duurkens R. H., Olieman K., and Erkens G. B. Static light scattering to characterize membrane proteins in detergent solution. *Methods*, 46(2):73–82, 2008.

[191] Chae P. S., Rasmussen S. G. F., Rana R. R., Gotfryd K., Chandra R., Goren M. A., Kruse A. C., Nurva S., Loland C. J., Pierre Y., Drew D., Popot J. L., Picot D., Fox B. G., Guan L., Gether U., Byrne B., Kobilka B., and Gellman S. H. Maltose-neopentyl glycol (MNG) amphiphiles for solubilization, stabilization and crystallization of membrane proteins. *Nature Methods*, 7(12):1003–U90, 2010.

[192] Alexandrov A. I., Mileni M., Chien E. Y. T., Hanson M. A., and Stevens R. C. Microscale fluorescent thermal stability assay for membrane proteins. *Structure*, 16(3):351–359, 2008.

[193] Postis V. L. G., Deacon S. E., Roach P. C. J., Wright G. S. A., Xia X., Ingram J. C., Hadden J. M., Henderson P. J. F., Phillips S. E. V., McPherson M. J., and Baldwin S. A. A high-throughput assay of membrane protein stability. *Molecular Membrane Biology*, 25(8):617–624, 2008.

[194] Kolaj-Robin O., Russell D., Hayes K. A., Pembroke J. T., and Soulimane T. Cation Diffusion Facilitator family: Structure and function. *Febs Letters*, 589(12):1283–1295, 2015.

[195] Lin W., Chai J., Love J., and Fu D. Selective electrodiffusion of zinc ions in a Zrt-, Irt-like Protein, ZIPB. *Journal of Biological Chemistry*, 285(50):39013–39020, 2010.

[196] Zhang T., Liu J., Fellner M., Zhang C., Sui D. X., and Hu J. Crystal structures of a ZIP zinc transporter reveal a binuclear metal center in the transport pathway. *Science Advances*, 3(8), 2017.

[197] M. Rahman. *Structural and functional studies on membrane transport proteins*. Phd, University of Leeds, 2007.

[198] V. Vasilca. *Nanoscale Spherical-Supported Membranes as Novel Plat-*

forms for Improving the Phage Display Screening of Antibody Mimetics against Membrane Protein Targets. Phd, University of Leeds, 2016.

[199] Kehres D. G., Zaharik M. L., Finlay B. B., and Maguire M. E. The NRAMP proteins of *Salmonella typhimurium* and *Escherichia coli* are selective manganese transporters involved in the response to reactive oxygen. *Molecular Microbiology*, 36(5):1085–1100, 2000.

[200] Garcia-Celma J. J., Smirnova I. N., Kaback H. R., and Fendler K. Electrophysiological characterization of LacY. *Proceedings of the National Academy of Sciences of the United States of America*, 106(18):7373–7378, 2009.

[201] Haemig H. A. H. and Brooker R. J. Importance of conserved acidic residues in MntH, the Nramp homolog of *Escherichia coli*. *Journal of Membrane Biology*, 201(2):97–107, 2004.

[202] Chaloupka R., Courville P., Veyrier F., Knudsen B., Tompkins T. A., and Cellier M. F. M. Identification of functional amino acids in the Nramp family by a combination of evolutionary analysis and biophysical studies of metal and proton cotransport in vivo. *Biochemistry*, 44(2):726–733, 2005.

[203] Courville P., Urbankova E., Rensing C., Chaloupka R., Quick M., and Cellier M. F. M. Solute carrier 11 cation symport requires dis-

tinct residues in transmembrane helices 1 and 6. *Journal of Biological Chemistry*, 283(15):9651–9658, 2008.

[204] Lan W. J., Ren H. L., Pang Y., Huang C. S., Xu Y. F., Brooker R. J., and Zhang J. Y. A facile transport assay for h^+ coupled membrane transport using fluorescence probes. *Analytical Methods*, 4(1):44–46, 2012.

[205] Nelson N. Metal ion transporters and homeostasis. *Embo Journal*, 18(16):4361–4371, 1999.

[206] Schulz P., Celma-Garcia J. J., and Fendler K. SSM-based electrophysiology. *Methods*, 46:97–103, 2008.

[207] Tsai M. F., McCarthy P., and Miller C. Substrate selectivity in glutamate-dependent acid resistance in enteric bacteria. *Proceedings of the National Academy of Sciences of the United States of America*, 110(15):5898–5902, 2013.

[208] Nachin L., Nannmark U., and Nystrom T. Differential roles of the universal stress proteins of *Escherichia coli* in oxidative stress resistance, adhesion, and motility. *Journal of Bacteriology*, 187(18):6265–6272, 2005.

[209] Waldron K. J. and Robinson N. J. How do bacterial cells ensure that

metalloproteins get the correct metal? (vol 7, pg 25, 2009). *Nature Reviews Microbiology*, 7(2):1, 2009.

[210] Robertson D. E., Kaczorowski G. J., Garcia M. L., and Kaback H. R. Active-transport in membrane-vesicles from *Escherichia-coli* - the electrochemical proton gradient alters the distribution of the lac carrier between 2 different kinetic states. *Biochemistry*, 19(25):5692–5702, 1980.

[211] Viitanen P., Garcia M. L., and Kaback H. R. Purified reconstituted lac carrier protein from *Escherichia-Coli* is fully functional. *Proceedings of the National Academy of Sciences of the United States of America-Biological Sciences*, 81(6):1629–1633, 1984.

[212] Chen X. Z., Peng J. B., Cohen A., Nelson H., Nelson N., and Hediger M. A. Yeast SMF1 mediates H^+-coupled iron uptake with concomitant uncoupled cation currents. *Journal of Biological Chemistry*, 274(49):35089–35094, 1999.

[213] Nelson N., Sacher A., and Nelson H. The significance of molecular slips in transport systems. *Nature Reviews Molecular Cell Biology*, 3(11):876–881, 2002.

[214] Iwata S. *Methods and results in crystallization of membrane proteins*, volume 4. Internat'l University Line, 2003.

[215] Parker J. L. and Newstead S. *Membrane Protein Crystallisation: Current Trends and Future Perspectives*, pages 61–72. Springer International Publishing, Cham, 2016.

[216] Newstead S. and Ferrandon S. and Iwata S. Rationalizing α-helical membrane protein crystallization. *Protein Science*, 17(3):466–472, 2008.

[217] Parker J. L. and Newstead S. Current trends in α-helical membrane protein crystallization: An update. *Protein Science*, 21(9):1358–1365, 2012.

[218] Sonoda Y., Cameron A., Newstead S., Omote H., Moriyama Y., Kasahara M., Iwata S., and Drew D. Tricks of the trade used to accelerate high-resolution structure determination of membrane proteins. *FEBS Letters*, 584(12):2539–2547, 2010.

Appendix

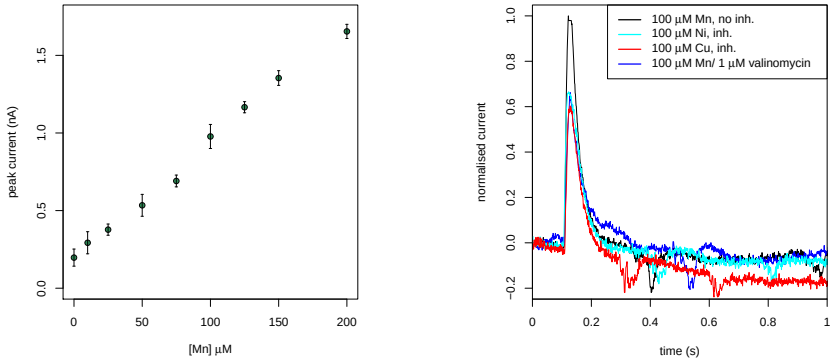

(a) *Concentration dependence of Mn^{2+}-induced currents for his-tag cleaved MntH2.*

(b) *Inhibition of Mn^{2+}-induced currents by Ni^{2+} and Cu^{2+} for his-tag cleaved MntH2. Because of the high background of the sensor, a control experiment was performed with valinomycin.*

Figure A1: *Control experiments on SURFE^{2}R with his-tag cleaved MntH2. Qualitatively the data is not different from data recorded with uncleaved protein.*

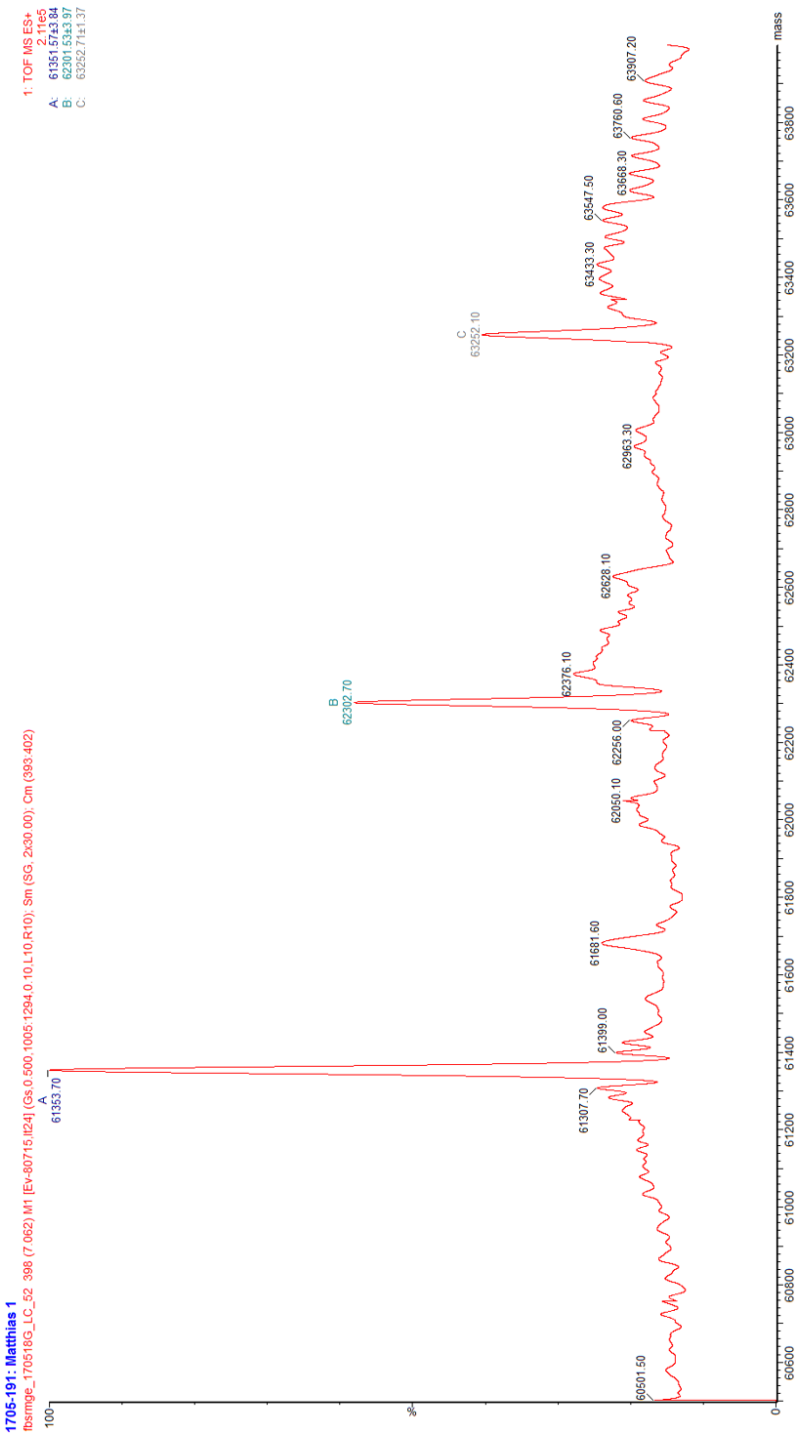

Figure A2: *Complete mass spectrum of P1.*

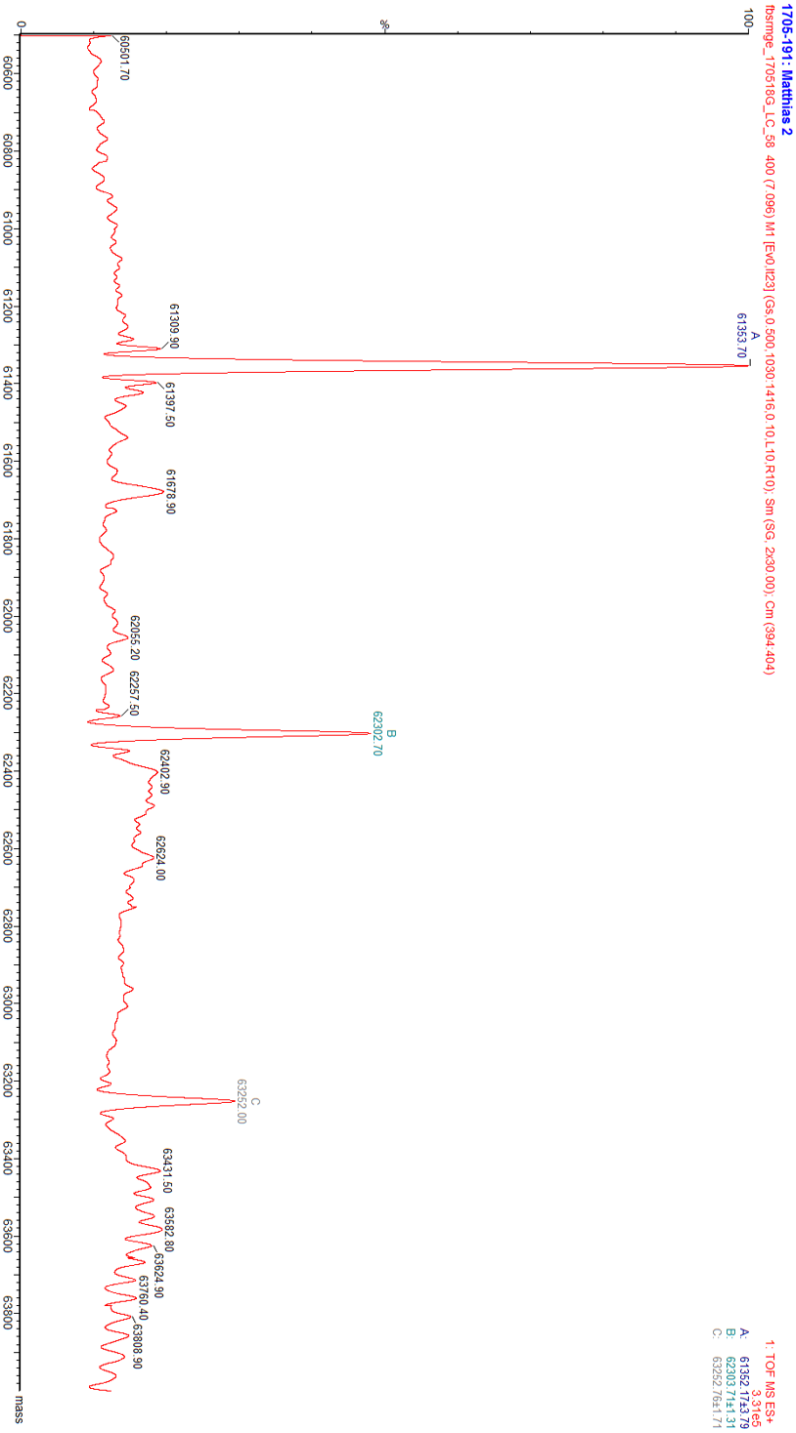

Figure A3: *Complete mass spectrum of P2.*